Chemical
Science

ROYAL SOCIETY
OF CHEMISTRY

REVIEW

View Article Online
View Journal | View Issue

Cite this: *Chem. Sci.*, 2025, **16**, 21705

High-performance organic semiconductor near-infrared and shortwave-infrared photodetectors: a materials and device roadmap

Hongyu Tan,†[a] Xianshuo Wu,†[a] Suhao Hu,[a] Yiwen Ren,[a] Yuhan Du,[a] Qiang Zhao,[b] Lingjie Sun,*[a] Fangxu Yang*[a] and Wenping Hu[a]

Organic semiconductors have emerged as versatile platforms for near-infrared (NIR, 650–900 nm) and short-wave infrared (SWIR, 900–1700 nm) photodetection, offering tunable absorption, mechanical flexibility, and low-temperature, solution-based processing. However, realizing truly high-performance organic NIR–SWIR photodetectors (OPDs) requires simultaneous optimization of multiple interdependent metrics, including narrow optical bandgaps for extended spectral coverage, low trap-state densities to suppress dark current, efficient exciton dissociation for high responsivity, and ultralow noise for exceptional detectivity, along with fast, stable responses under real-world operating conditions. In this performance-focused review, we consolidate recent advances in narrow-bandgap donor polymers and non-fullerene acceptors that enable absorption onsets beyond 900 nm and into the SWIR region, while highlighting morphological strategies optimizing exciton diffusion against charge percolation. We then dissect device-level innovations including graded energy alignments, self-assembled interfacial dipoles, plasmonic enhancements, and hybrid integrations with quantum dots and 2D materials, which elevate responsivity above 0.4 A W^{-1} and detectivity toward 10^{13} Jones. Furthermore, we highlight emerging applications in wearable health monitoring, autonomous vision systems, and secure optical communications that exploit the unique conformability and tunability of organic semiconductors. Finally, we outline persistent challenges in stability, scalability, and dark-current suppression, proposing a roadmap for performance-driven material and architectural optimization, demonstrating how performance-driven optimization can unlock the full potential of large-area, conformal infrared sensing technologies.

Received 14th August 2025
Accepted 22nd October 2025

DOI: 10.1039/d5sc06197k

rsc.li/chemical-science

---

[a] *State Key Laboratory of Advanced Materials for Intelligent Sensing, Key Laboratory of Organic Integrated Circuit, Ministry of Education & Tianjin Key Laboratory of Molecular Optoelectronic Sciences, Department of Chemistry, School of Science & Institute of Molecular Aggregation Science, Tianjin University, Tianjin 300072, China. E-mail: sunlingjie@tju.edu.cn; yangfangxu@tju.edu.cn*

[b] *College of Science, Civil Aviation University of China (CAUC), Tianjin, 300300, China*

† Hongyu Tan and Xianshuo Wu have contributed equally to this work.

Hongyu Tan

Hongyu Tan was born in Guangxi Zhuang Autonomous Region, China. She received her bachelor's degree in 2024 from the Wuhan University of Technology. She is currently pursuing a Master's degree at the Department of Chemistry, School of Science, Tianjin University, focusing on molecular electronics, organic semiconductor ma-terial growth, and device fabrication.

Xianshuo Wu

Xianshuo Wu was born in Jiangsu province, China. She received her bachelor's degree in 2021 from Jiangnan University. Since 2021, she has been pursuing a PhD at the Department of Chemistry, School of Science, Tianjin University. Her research work focuses on molecular electronics, including crystalline organic semiconductor growth and device engineering.

1 Introduction

Organic semiconductors are opening exciting new horizons in near-infrared (NIR, 650–900 nm) and short-wave infrared (SWIR, 900–1700 nm) photodetection by combining precisely tunable absorption, mechanical flexibility, and low-temperature, solution-based processing.[1–4] These materials can be molecularly engineered to harvest NIR–SWIR photons at room temperature, enabling truly conformable, large-area sensors that bend around curved surfaces, integrate into fabrics, and roll-to-roll print at low cost.[5,6] Such flexible detectors are already being used in cutting-edge applications[7] such as wearable health monitors that noninvasively track blood oxygen levels and tissue perfusion beneath the skin,[8,9] intelligent vision systems for drones and autonomous vehicles that can operate in fog or darkness,[10,11] and secure, high-speed optical communication links that remain hidden in plain sight.[12,13] In each of these cases, the performance of an organic photodetector hinges on achieving a careful balance: high responsivity to detect even weak signals clearly, low dark current and noise to preserve accuracy in low light, and a fast, stable response to reliably capture rapid changes without drift. However, optimizing all these performance metrics at the same time is challenging. It requires carefully designed molecules to reduce trap states,[14] precisely controlled film morphologies to facilitate efficient exciton dissociation,[15,16] and device architectures that effectively manage interface engineering and enhance photoelectric conversion efficiency.[17] Only by meeting these demanding requirements can organic NIR–SWIR detectors fully realize their potential in next-generation biomedical diagnostics, environmental sensing under harsh conditions, and secure infrared data communication, applications where high sensitivity, fast response, and flexible form factors are indispensable.

Over the past decade, the field of organic NIR–SWIR photodetectors has witnessed remarkable advances in both materials science and device architecture, marking a dynamic frontier in optoelectronics research (Fig. 1).[15,16,18–30] Chemists have crafted a diverse portfolio of narrow-bandgap polymers featuring extended π-conjugation and finely tuned electron-withdrawing substituents, driving optical onsets below 1.55 eV to harvest photons beyond 800 nm.[19,31] Concurrently, non-fullerene acceptors with planar fused cores and tailored end groups have demonstrated absorption tails extending into the SWIR.[20,24,27,28,30,32] On the device side, simple bulk heterojunctions evolved into multilayer stacks with graded energy alignments, self-assembled interfacial dipoles, and ultrathin charge-blocking layers that suppress leakage currents.[22,25,29,33] Innovations such as organic single crystals[15,24] and cocrystals,[34] dielectric microcavities,[35] solid additives,[16] and vertical current pathways[36] have pushed responsivities above 0.4 A W^{-1} and detectivities toward 10^{13} Jones in the NIR. Hybrid approaches, which marry organic films with colloidal quantum dots[18,37,38] or two-dimensional materials,[21,39,40] have further broadened spectral coverage and enhanced exciton dissociation. Looking ahead, trends point toward integration of light-trapping metasurfaces, dynamic tuning of energy levels *via* electric or thermal stimuli, and fully printed modules that seamlessly integrate with flexible electronics.[25,26,41,42] Simultaneously, machine-learning-guided molecular design is accelerating the discovery of new polymer and small-molecule candidates with optimized energy landscapes and minimal trap densities. Taken together, these advances sketch a trajectory in which OPDs not only achieve parity with inorganic detectors in key metrics but also offer unparalleled adaptability for large-area, conformal, and low-cost infrared imaging and sensing platforms.

Despite these strides, the realization of truly high-performance organic NIR–SWIR detectors remains hampered by a constellation of interrelated challenges that underscore the necessity for a performance-focused insight. First, lowering the optical bandgap to access longer wavelengths typically exacerbates trap state density and thermal generation currents, which elevate dark current and degrade detectivity.[43,44] Second, the intrinsically low dielectric constant of organic materials leads to strongly bound Frenkel excitons, whose inefficient dissociation limits charge-carrier generation under low-intensity illumination.[45] Third, exciton diffusion lengths on the order of tens of nanometers mandate precise control of phase separation and domain purity to balance efficient dissociation against charge percolation.[46–48] Fourth, parasitic absorption by electrodes or transport layers, energy-level mismatches at each interface, and

---

Lingjie Sun

Lingjie Sun has been an associate professor at Tianjin University since 2024. Before that, she had postdoctoral experience at the Joint School of National University of Singapore and Tianjin University. She received her PhD degree from the Department of Chemistry, School of Science, Tianjin University in 2020. Her research interests mainly focus on organic optoelectronic materials and devices.

Fangxu Yang

Fangxu Yang is a Professor at Tianjin University. He obtained his master's degree from Harbin Institute of Technology in 2009 and his PhD from the Institute of Chemistry, Chinese Academy of Sciences in 2016. Afterward, he engaged in postdoctoral research at Tianjin University and joined the faculty in 2019. His research interests focus on photoelectric detection and imaging using organic semiconductor crystals.

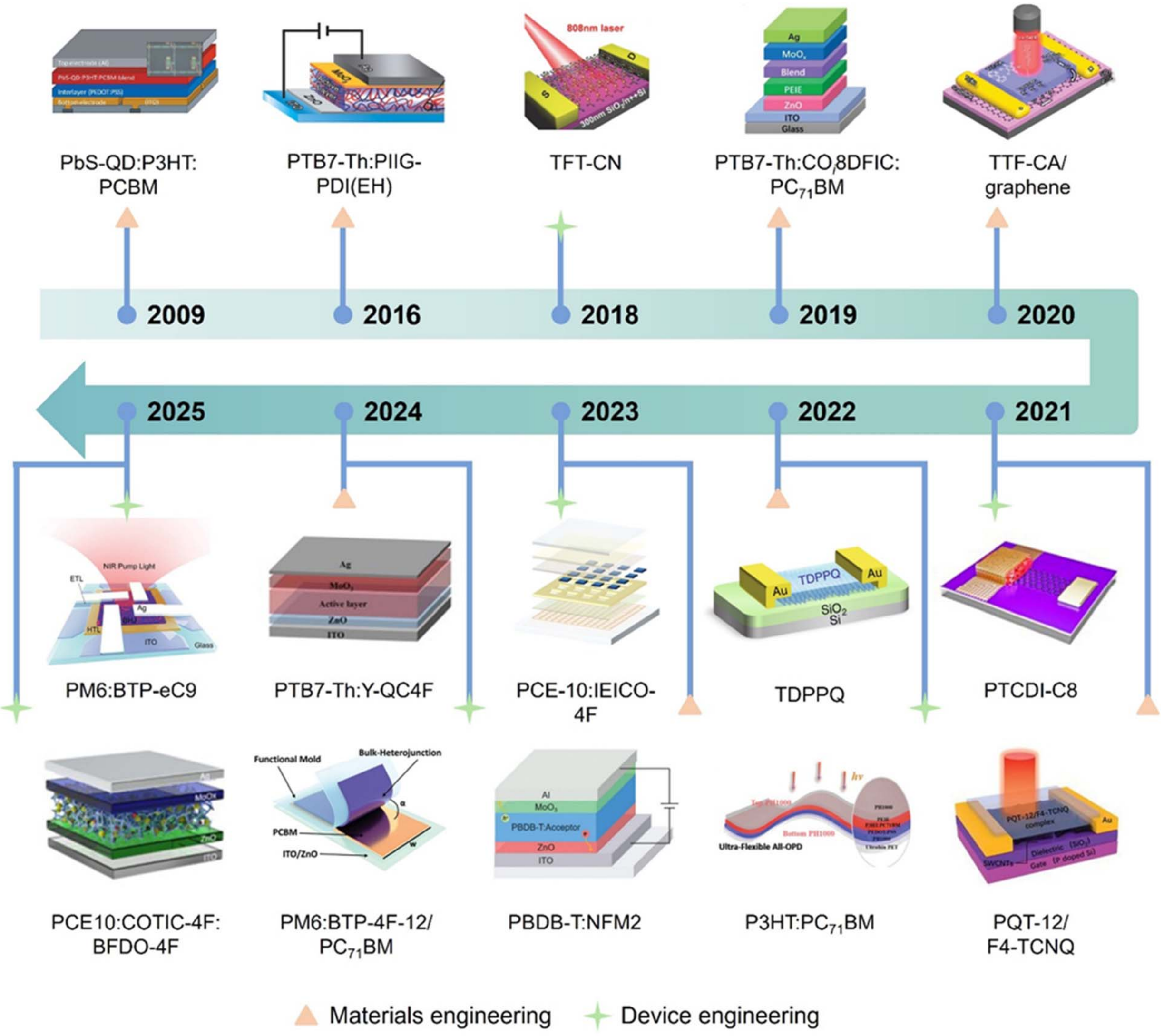

Fig. 1 The development roadmap of near-infrared and short-wavelength infrared detectors based on organic semiconductors. Reproduced from ref. 18 with permission from Springer, copyright 2009. Reproduced from ref. 19 with permission from Wiley-VCH, copyright 2016. Reproduced from ref. 15 with permission from Wiley-VCH, copyright 2018. Reproduced from ref. 20 with permission from Wiley-VCH, copyright 2019. Reproduced from ref. 21 with permission from Wiley-VCH, Copyright 2020. Reproduced from ref. 22 with permission from Springer, copyright 2021. Reproduced from ref. 23 with permission from Wiley-VCH, copyright 2021. Reproduced from ref. 24 with permission from Springer, copyright 2022. Reproduced from ref. 25 with permission from Wiley-VCH, copyright 2022. Reproduced from ref. 26 with permission from Springer, copyright 2023. Reproduced from ref. 27 with permission from Wiley-VCH, copyright 2023. Reproduced from ref. 28 with permission from Wiley-VCH, copyright 2024. Reproduced from ref. 29 with permission from Wiley-VCH, copyright 2024. Reproduced from ref. 16 with permission from Wiley-VCH, copyright 2025. Reproduced from ref. 30 Wiley-VCH, Copyright 2025.

morphological drift under bias and environmental stress all conspire to erode stability and reproducibility.[49,50] These obstacles are not isolated; they interact in complex ways, meaning that a solution that suppresses dark current may inadvertently slow response time or reduce spectral bandwidth. Despite the growing number of reports on individual materials and device configurations, a unified framework that links molecular design rules, morphological parameters, and architectural strategies to holistic device performance across the full NIR–SWIR spectrum is still lacking. Bridging this gap requires a systematic, performance-oriented review that identifies successful paradigms, clarifies key trade-offs, and outlines a coherent roadmap for the advancement of next-generation infrared OPDs.

Herein, we present a systematic and focused review on the optimization of high-performance NIR–SWIR OPDs, aiming to bridge fragmented advancements and establish a clear roadmap for future research (Fig. 2). We begin by consolidating molecular design principles for achieving narrow optical bandgaps while minimizing trap densities, highlighting recent breakthroughs in donor polymer development, small-molecule acceptor synthesis, morphological control, and energy-level alignment. Building upon this foundation, we analyze device engineering strategies aimed at suppressing dark current and

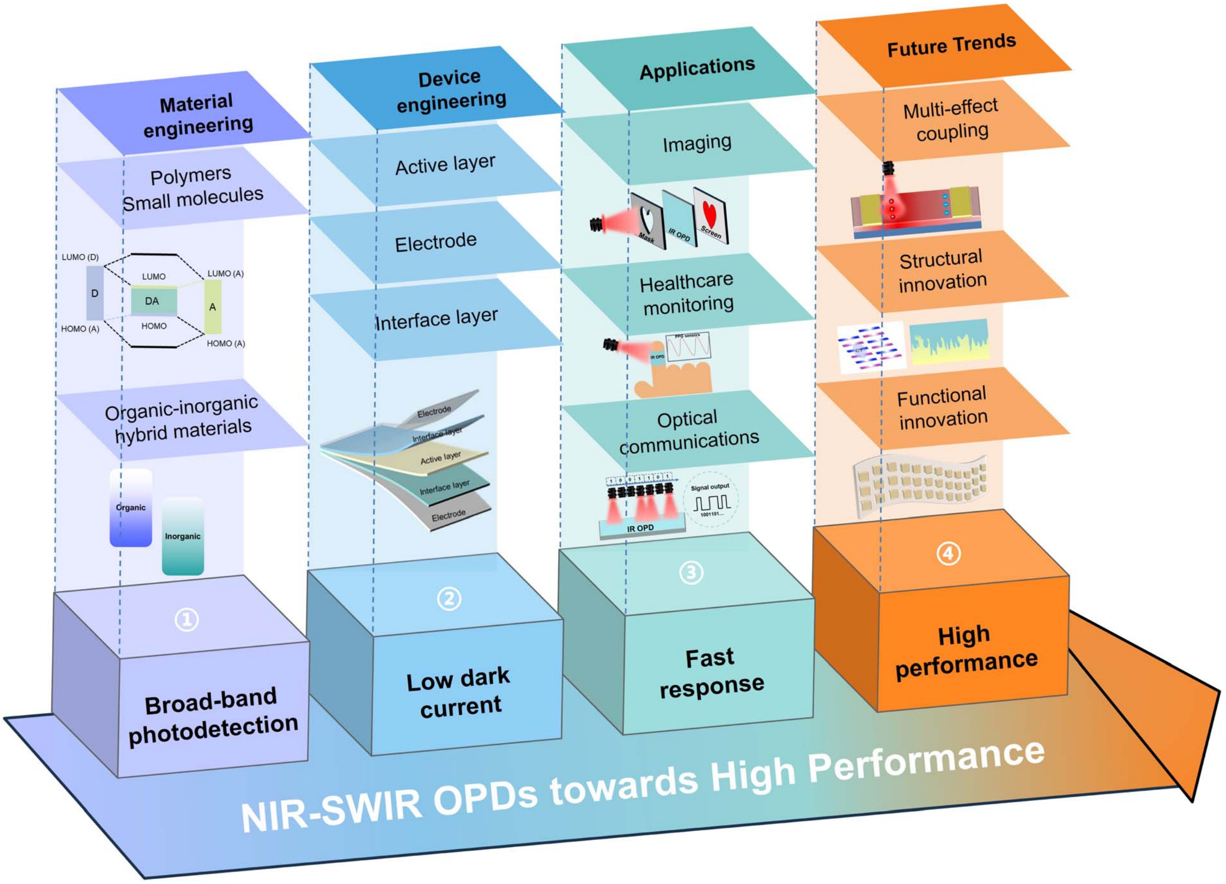

Fig. 2 An overview of NIR–SWIR OPDs advancement towards high performance, from the development of organic semiconductor materials, innovative design of device structures to advanced optoelectronic applications, and further to future prospects.

enhancing responsivity, encompassing interfacial layer selection, electrode modification, field-management architectures, and hybrid integration approaches. We further highlight emerging applications such as artificial vision systems, infrared imaging arrays, wearable health monitoring devices, and secure optical communication, which leverage the unique advantages of high-performance OPDs and underscore the practical significance of each design paradigm. Finally, we critically examine persistent challenges such as operational stability, scalable fabrication, and integration with complementary technologies, and propose targeted directions for future investigation. By emphasizing performance-driven optimization and offering a cohesive synthesis of material and device innovations, this review delivers timely and actionable insights for the development of next-generation OPDs for broadband infrared sensing.

2 Classification and performance parameters of photodetectors

2.1 Classification and working mechanisms of photodetectors

Photodetectors are devices that convert optical signals into electrical signals and can be categorized into two main types: photoelectric detectors and photothermal detectors.[51] Based on device architectures, photoelectric detectors are classified into three primary categories: photo-transistor organic photodetectors (PT-OPDs), photodiode organic photodetectors (PD-OPDs), and photoconductive organic photodetectors (PC-OPDs). According to the properties of the materials, organic photothermal detectors can be divided into two categories, photothermoelectric organic photodetectors (PTE-OPDs) and pyroelectric organic photodetectors (PE-OPDs).

2.1.1 Photoelectric detectors. The fundamental principle of photoelectric detectors based on the photoelectric effect[45,52,53] involves the following sequence: when illuminated, organic semiconductor materials (active layers) absorb photons with energy exceeding the semiconductor bandgap, generating Frenkel excitons (tightly bound electron–hole pairs). These Frenkel excitons subsequently diffuse to the heterojunction interface where they dissociate into charge-transfer (CT) excitons (weakly bound electron–hole pairs). Under applied bias voltage, CT excitons further separate into free electrons and holes, which then transport to respective electrodes and are collected, ultimately generating photocurrent.

To promote efficient dissociation of Frenkel excitons into free carriers, active layer architectures are commonly classified into two categories: single-component layers containing ambipolar molecular structures with integrated donor–acceptor units, and heterojunctions composed of discrete donor (D) and acceptor (A) materials. Effective exciton separation requires a minimum energy difference (>0.3 eV) between the highest occupied molecular orbital (HOMO) of the donor and the lowest unoccupied molecular orbital (LUMO) of the acceptor. Single-component layers exhibit limited performance as exciton dissociation predominantly occurs at material–electrode interfaces. Heterojunction configurations can adopt either planar heterojunction (PHJ) through vertically stacked donor–acceptor layers[55] or bulk heterojunction (BHJ) with interpenetrating donor–acceptor networks *via* blending.[56] Given that Frenkel excitons in organic semiconductors typically demonstrate sub-20 nm diffusion lengths and organic materials possess maximum absorption coefficients around 10^5 cm^{-1}, PHJ devices (bilayer structures) require optimized donor and acceptor layer thicknesses below 40 nm to achieve incident light absorption efficiencies up to 55%.[53] Compared to PHJ architectures, BHJ configurations facilitate increased Frenkel exciton diffusion to D–A interfaces for improved dissociation efficiency, thereby significantly enhancing device performance.

As illustrated in Fig. 3(a), PT-OPDs exhibit structural similarities to organic field-effect transistors (OFETs), comprising three electrodes (source, drain, and gate), an active layer, and a dielectric layer. Their operational principle is rooted in the photoelectric effect: exposure to incident light with energy exceeding the semiconductor bandgap induces exciton generation within the active layer. A portion of these excitons undergo accelerated dissociation into dual carriers (electrons and holes) under gate voltage modulation, thereby amplifying photocurrent generation. Notably, PT-OPDs enable additional photoconductive gain through applied electric bias. The high gain originates from the trapping and prolonged retention of one type of photogenerated carrier at defects or trap states within the OPD channel, which allows the other type of carrier to circulate and contribute repeatedly to conduction, thereby amplifying the photocurrent. The photoconductive gain is given by $G = \tau/t_L$, where τ denotes the carrier lifetime and t_L represents the transit time between electrodes. Although high responsivity requires large gain, a long carrier lifetime implies slow recombination, leading to extended response time.[57,58] To balance the trade-off between high gain and fast response in PT-OPDs, it is essential to select materials with high crystallinity and high carrier mobility to reduce t_L and minimize reliance on trap-assisted gain mechanisms.[59,60] Furthermore, innovative device strategies, such as the use of high-capacitance oxide dielectrics,[61] multi-gate structures,[62] and photo-gating assisted tunneling,[57] can accelerate carrier transport, thereby shortening t_L and enabling simultaneously high responsivity and fast response. For instance, Yang *et al.*[63] incorporated a hexagonal boron nitride (h-BN) dielectric layer into an organic/graphene phototransistor, which effectively passivated trap states and

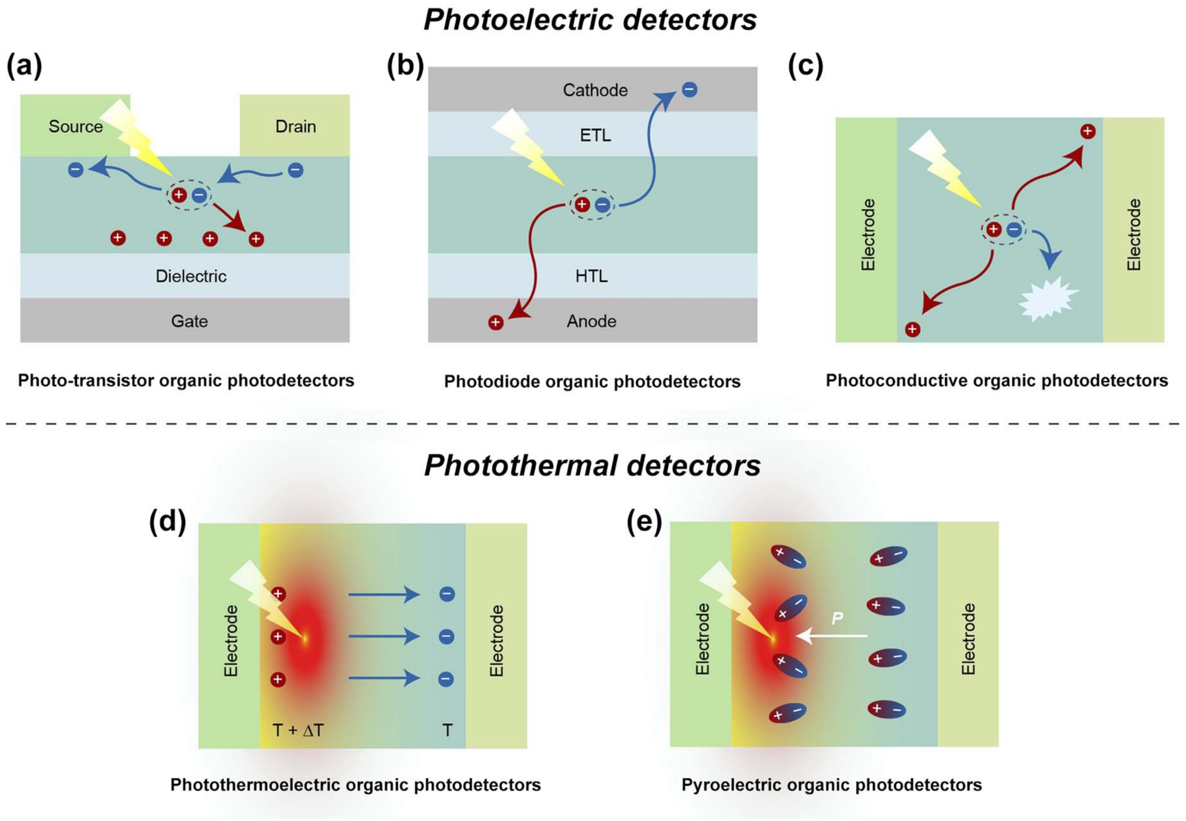

Fig. 3 The configuration and working mechanism of OPDs: (a) photo-transistor organic photodetectors (PT-OPDs), (b) photodiode organic photodetectors (PD-OPDs), (c) photoconductive organic photodetectors (PC-OPDs), (d) photothermoelectric organic photodetectors (PTE-OPDs), (e) pyroelectric organic photodetectors (PE-OPDs). Adapted from ref. 54 with permission from Wiley-VCH, copyright 2021.

suppressed interfacial carrier recombination, thereby reducing the response time from 39.4 ms to 7.15 ms.

As depicted in Fig. 3(b), PD-OPDs feature multilayer architectures comprising electrodes, electron transport layers (ETLs), active layers, and hole transport layers (HTLs). Based on layer stacking sequences, PD-OPDs are categorized into conventional and inverted configurations. Conventional PD-OPDs adopt cathode-up device structures (Fig. 3(b)), whereas inverted PD-OPDs employ anode-up architectures. The inverted configuration generally exhibits enhanced stability due to reduced oxidation susceptibility at the top anode interface. Both configurations require one transparent electrode to ensure effective light absorption by the active layer. The operational principle of PD-OPDs is also fundamentally rooted in the photoelectric effect. The working process can be systematically described as follows: the active layer material initially absorbs photon energy to generate photoinduced excitons. These excitons subsequently diffuse to donor–acceptor (D–A) interfaces where they typically dissociate into free electrons and holes under reverse bias voltage. The liberated electrons then transport along the acceptor's LUMO towards the cathode. Upon reaching the ETL, they undergo efficient collection and rapid transfer to the electrode. Simultaneously, the free holes migrate *via* the donor's HOMO pathways toward the anode, where they are effectively captured by the HTL and promptly delivered to the electrode. This coordinated charge transport mechanism ultimately produces measurable photocurrent. Similar to PT-OPDs, PD-OPDs achieve photoconductive gain by extending the carrier lifetime and accelerating charge transport. To obtain high photoconductive gain, PD-OPDs typically require the application of a high bias voltage to facilitate charge carrier tunneling and injection. However, high bias may lead to a significant increase in dark current.[64,65] Developing materials with high crystallinity and few defects can help shorten the carrier transit time t_L while reducing dark current under high bias. Meanwhile, innovative device strategies,[66,67] such as incorporating emission layers, lateral architectures, and insulating interfacial layers, can further suppress dark-state carrier recombination and leakage current, thereby maximizing photogain.

Photoconductive organic photodetectors (PC-OPDs) consist of an active layer sandwiched between ohmic-contact electrodes, typically fabricated from organic small-molecule or polymer semiconductor materials. As illustrated in Fig. 3(c), under applied bias, photogenerated carriers experience multiple collection cycles through a photomultiplication (PM) mechanism, achieving remarkable photoconductive gains exceeding 100% and external quantum efficiency (EQE) values surpassing unity (>100%). However, the inherent lateral charge transport configuration significantly extends carrier transit distances. This geometric constraint necessitates high reverse bias voltages, triggering undesirable carrier injection phenomena that elevate dark current densities while concomitantly prolonging response times to millisecond-scale levels.

2.1.2 Photothermal detectors. Recent advances in photothermal detectors driven by photothermoelectric or pyroelectric effects demonstrate significant potential for energy-efficient photodetection. Unlike conventional organic photodetectors restricted by intrinsic material bandgaps, these devices enable broad-spectrum detection and self-powered operation through thermoelectric conversion.[68,69] The photothermoelectric effect involves two sequential processes: photothermal conversion where photon absorption generates thermal gradients (ΔT); thermoelectric (seebeck) effect where carrier diffusion along the temperature gradient produces electrical potentials (Fig. 3(d)).[70] Guo *et al.*[71] developed a flexible 4 × 4 infrared thermopile array by integrating tellurium/copper telluride (Te/CuTe) multilayered films (optimized for optical reflection suppression) with polyimide substrates (exhibiting strong infrared absorption). This configuration achieved remarkable thermal sensitivity (3.2 μV per 0.05 °C temperature variation) and successfully implemented temperature warning systems in soft robotic claws. As illustrated in Fig. 3(e), the pyroelectric effect in polarized polymers generates spontaneous electric dipoles with compensating surface charges. Incident radiation alters crystal symmetry through thermal expansion, reducing polarization intensity and producing measurable pyroelectric currents. Common pyroelectric polymers include polyvinylidene fluoride (PVDF)[72] and poly(vinylidene fluoride-*co*-trifluoroethylene) (PVDF-TrFE) copolymers.[73,74] Nevertheless, photothermal detectors face fundamental limitations from slow thermal dynamics and low responsivity, necessitating further research. This study primarily focuses on photoelectric-effect-based organic photodetectors.

2.2 Photodetector performance parameters

The critical parameters for evaluating photodetector performance encompass spectral response range, external quantum efficiency (EQE), responsivity (R), sensitivity (P), noise equivalent power (NEP), specific detectivity (D^*), linear dynamic range (LDR), and response speed.

2.2.1 Spectral response range. The spectral responsivity of organic photodetectors (OPDs) is fundamentally determined by the absorption characteristics of their active layers. Organic semiconductors exhibit tunable optoelectronic properties through molecular engineering, allowing tailored responsivity from ultraviolet (UV) to near-infrared (NIR) spectral regions. Broadband OPD configurations typically employ active materials with extended π-conjugation systems and complementary absorption profiles to achieve wide spectral coverage. Conversely, achieving high-sensitivity photodetection within narrow spectral ranges (full width at half maximum < 50 nm) poses greater technical challenges.

2.2.2 Responsivity and external quantum efficiency. Responsiveness (R) refers to the ratio of the photocurrent generated by a detector under illumination of a certain wavelength of light to the incident light power, that is, the photocurrent generated under illumination of a unit power.

$$R = I_{\mathrm{ph}}/P_{\mathrm{in}} \tag{2.1}$$

In eqn (2.1), I_{ph} represents the photocurrent (A), and P_{in} represents the incident light power (W cm^{-2}).

EQE refers to the ratio of the number of collected charge carriers to the number of incident photons, and it is an important indicator for testing the performance of photodetectors.

$$\mathrm{EQE} = I_{\mathrm{ph}}hc/(P_{\mathrm{in}}\lambda e) \tag{2.2}$$

In eqn (2.2), h represents Planck's constant, c represents the speed of light, λ represents the incident wavelength,e represents the elementary charge. For photodiode detectors, EQE typically remains below 100%. In contrast, photoconductive detectors frequently exhibit EQE values exceeding 100% through photoconductive gain phenomena, where the EQE is redefined as the ratio between the trapped charge carrier lifetime and the free carrier transit time.

2.2.3 Noise. Noise can be divided into shot noise, thermal noise (Johnson–Nyquist noise), and flicker noise (1/f noise). Shot noise describes the interference with the optical radiation signal induced by the random fluctuations of electrons inside the device as a result of bias voltage and thermal excitation during operation. Thermal noise originates from the irregular motion of electrons in resistive components, which affects the accuracy of the device output. Both shot and thermal noise demonstrate frequency-independent white noise characteristics. Low-frequency noise is inversely related to frequency and is nearly always present in different photodetectors. Flashing noise often occurs in the frequency band below 1 kHz of the signal frequency and rapidly diminishes as the signal frequency increases. The source of noise for infrared photodetectors is primarily determined by the device's working conditions; shot noise predominates at high bias voltages, whereas thermal noise is the primary source at low bias voltages.

2.2.4 Sensitivity. Sensitivity (P) refers to the ratio of photocurrent to dark current, commonly referred to as the switching ratio. A higher sensitivity indicates improved response performance of the device.

$$P = I_{\mathrm{ph}}/I_{\mathrm{d}} \tag{2.3}$$

In eqn (2.3), I_{d} represents the dark current value of the device in the absence of light. J_{d} (dark current density, mA cm^{-2}) is commonly used in literature to represent it, and I_{d} or J_{d} indirectly reflects the noise level of the device.

2.2.5 Noise equivalent power and specific detectivity. Noise equivalent power (NEP) and specific detectivity (D^*) are key parameters that quantify the impact of noise on device performance. NEP signifies the minimum optical power required for a photodetector to differentiate between signal and noise. A lower NEP indicates a higher sensitivity of the photodetector.

$$\mathrm{NEP} = (I_{\mathrm{n}}/\Delta f^{1/2})/R \tag{2.4}$$

In eqn (2.4), I_{n} represents the noise current, and Δf denotes the bandwidth of the noise measurement.

D^* is a metric utilized to quantify the detector's capability to identify the weakest optical signals, allowing for direct comparison of sensitivity among different device structures. A higher D^* value indicates superior sensitivity of the device. When the noise source is exclusively dark current, D^* can be calculated as shown in eqn (2.5).

$$D^* = (S^{1/2}R)/(2eI_{\mathrm{d}}) = R(Sf)^{1/2}/I_{\mathrm{n}} = S^{1/2}/\mathrm{NEP} \tag{2.5}$$

In eqn (2.5), S is the effective area of the device, and D^* is measured in Jones (1 Jones = 1 cm Hz$^{1/2}$ W^{-1}).

2.2.6 Linear dynamic range. Under reverse bias conditions, the photocurrent generated by the device exhibits a linear increase in response to an increase in incident light power. The linear dynamic range (LDR) is defined as the interval between the maximum and minimum light intensities that a photodetector is capable of detecting.

$$\mathrm{LDR} = 20\log(I_{\mathrm{ph,max}}/I_{\mathrm{ph,min}}) \tag{2.6}$$

In eqn (2.6), $I_{\mathrm{ph,max}}$ and $I_{\mathrm{ph,min}}$ denote the maximum and minimum photocurrent, respectively, within the linear correlation between photocurrent and light intensity. The unit of measurement for LDR is decibels (dB).

2.2.7 Response speed. The response speed is determined by the rise time of photocurrent generated by photodetector under light radiation irradiation and the fall time of current when the light radiation stops. The rise time (t_{r}) is the time required for the photocurrent to rise from 10% to 90%, and the fall time (t_{d}) is the time required for the photocurrent to fall from 90% to 10%. The shorter the response time, the faster the device responds to the light radiation signal.

The cut-off frequency is defined as the frequency at which the optical response value decreases to $1/\sqrt{2}$ ($\sim$0.707 times) of the peak value, and is typically expressed as a -3 dB bandwidth. A higher cutoff frequency indicates that the device can respond more rapidly to signals with higher modulation frequencies.

3 Organic material choices and design principles for high performance IR detection

Generally, the materials for IR detection can be categorized into two distinct groups: conjugated polymers and conjugated small molecules. OPDs work on a similar principle as organic solar cells, and therefore advances in OPDs are closely related to the improvement of organic solar cells, especially the use of new materials with narrower optical gaps.[75] In recent years, more and more materials with narrow bandgaps have been developed and have demonstrated remarkable performance in photodetectors, in order to expand the spectral response range of organic materials.

3.1 Polymers

In 1977, Heeger *et al.*[76] reported the pioneering work of significant increase in electrical conductivity after halogenation of polyacetylene, which revealed for the first time the fact that polymers conduct electricity, thus unveiling conductive polymers in the history of semiconductors. Semiconducting polymers have a large bandwidth, similar to that of inorganic semiconductors, due to the π-electron overlap of the conjugated system in the repeating unit. However, interchain interactions are weak, comparable to van der Waals interactions in molecular crystals. This anisotropy between intra-chain and extra-chain makes the exciton binding energy of semiconducting polymers intermediate between that of Wannier and Frenkel excitons.[77] The advantages of structural tunability, flexibility, and solution-processability have led to the wide application of semiconducting polymers in the field of organic photovoltaic devices. Research on polymer photodetectors has also made significant progress over the past few decades.

In 1992, Sariciftci *et al.*[55] discovered that a conjugated polymer can rapidly transfer electrons to a fullerene under light-induced conditions. This finding led to the rapid development of photoactive layers composed of polymers and fullerene derivatives in the field of organic photovoltaic devices. Currently, the most widely used polymer photodetectors are BHJ active layers co-blended with polymer donors and fullerene derivatives or small molecule acceptors. While the BHJ active layer reduces the distance of exciton diffusion, it concomitantly increases the probability of carrier complexation. It is therefore vital to use high carrier mobility (μ) of π-conjugated polymers to facilitate transport of separated charges across the active layer, which in turn reduces charge complexation. Increasing the stiffness of the backbone and extending the conjugate planarity are commonly used methods to improve the carrier mobility of conjugated polymers. Representative polymer donor molecules include the poly(3-hexylthiophene-2,5-diyl) (P3HT) series, the poly[[4,8-bis[(2-ethylhexyl)oxy]benzo[1,2-*b*:4,5-*b*′]dithiophene −2,6-diyl][3-fluoro-2-[(2-ethylhexyl)carbonyl] thieno[3,4-*b*]thiophenediyl]] (PTB7) series, and the diketopyrrolopyrrole (DPP) series *etc.* Fig. 4 shows some commonly used design principles for narrow-bandgap polymer donors.[92] Fig. 5 illustrates the polymer donor molecules employed in the literature in recent years. Table 1 summarizes the research progress of NIR-SWIR OPDs with polymers as donors in recent years. To achieve infrared light detection, the HOMO and LUMO energy levels of the polymer donor must be higher than the two energy levels of the acceptor, and the energy difference between the HOMO energy level of the donor and the LUMO energy level of the acceptor must be between 0.3 eV and 1.55 eV to achieve efficient exciton separation and IR light absorption, thus requiring effective strategies to modulate the energy poles of both. The backbones of new conjugated polymer donors usually adopt alternating donor–acceptor (D–A) conjugated structures. Fig. 4(b) shows some of the commonly used building blocks for D and A units.[92] The D–A structure can effectively increase the HOMO energy level of the polymer, stabilize the electron-rich donor polymer chains and reduce the band gap of the material by exploiting the intramolecular charge transfer effect between the donor/puller electron units.[93] Heeger *et al.*[94] reported a polymer photodetector using a narrow bandgap polymer, poly(5,7-bis(4-decanyl-2-thienyl)-thieno(3,4-*b*)diathiazole-thio-phene-2,5) (PDDTT), as the donor and (6,6)-phenyl-C61-butyric acid methyl ester ($PC_{60}BM$) as the acceptor, with a spectral response in the range of 300–1450 nm. The device detectivity is greater than 10^{12} cm $Hz^{1/2}$ W^{-1} at room temperature, and the LDR is more than 100 dB, which extends the spectral response range to the SWIR region for the first time. The electron withdrawing unit thienopyrazine in the PDDTT not only stabilises the electron-rich thiophene chain but also accelerates the charge transfer to the conjugated backbone. Wang *et al.*[95] synthesized polythiophene derivatives containing two electron-deficient units, diketo-pyrrolopyrrole and thiophene isoindigo, and used [6,6]-phenyl-C71-butyric acid methyl ester ($PC_{71}BM$) as an acceptor for 300–1200 nm light detection. The device has a higher detection rate than 10^{11} Jones, probably because the electron-deficient unit enhances the HOMO energy level of the polythiophene derivatives from −5.41 eV to −4.76 eV, while the LUMO energy level remains almost unchanged, which reduces the optical bandgap of the polymer. Zheng *et al.*[96] reported the detection rate higher than that of 10^{11} Jones for a poly[(4,7-bis(3-hexylthien-2-yl)-$2\lambda^4\delta^2$-benzo[1,2-*c*;4,5*c*′]bis[1,2,5]thiadia-zole)-*alt*-(*N*-(3,4,5-tris(dodecyloxy) phenyl)-dithieno[3,2-*b*:2′,3′-*d*]pyrrole)] (PBBTPD):Tri-$PC_{61}BM$ photodetector with a spectral response up to 2500 nm, which is attributed to the fact that the PBBTPD carries a strong electron acceptor portion (benzobisthiadiazole) and a strong electron donor portion (dithienopyrrole), which exhibits a very low optical bandgap (0.5 eV). Nguyen's group[35] used a resonant optical microcavity to extend the wavelength detection range of PD-OPD based on poly[(2,6′-4,8-di(5-ethylhexylthienyl)benzo [1,2-*b*:3,4-*b*′]dithio-phene)-*alt*-(3-fluoro-2-((2-ethylhexyl) carbonyl)thieno [3,4-*b*] thiophenediyl)] (PTB7-Th also called PCE10): 2,2′-((2*Z*,2′*Z*)-(((4,4-bis(2-ethylhexyl)-4*H*-cyclopenta[2,1-*b*:3,4-*b*′]dithioph-ene-2,6-diyl)bis(4-(2-ethylhexyloxy)thiophene-5,2-diyl))bis (methanylylidene))bis(5,6-difluoro-3-oxo-2,3-dihydro-1*H*-in-den-2,1-diylidene))dimalononitrile (COTIC-4F) (655 nm thickness) to 1200 nm. The detector has a high D^* of 2.61×10^{13} Jones at 1150 nm and a lower J_d of 3.82×10^{-8} A cm^{-2} at −5 V.

The introduction of quinonal structures into the conjugated backbone of polymers is another effective way to reduce the band gap of π-conjugated polymers. This may be due to the fact that the transformation of the aromatic structure into a quinone-like structure results in a stronger delo-calisation of π-electrons along the conjugated backbone, leading to minimization of bond length alternation (BLA), which in turn effectively reduces the band gap of the polymer.[97] Fig. 4(c) shows some typical ground-state quinoid units. Liu's group accordingly designed *p*-azaquinodi-methane (*p*-AQM) motifs and found that the band gap of P2 polymer containing *p*-AQM was 1.49 eV.[98] Later, Liu's group[99] reported a new quinoid–donor–acceptor (Q–D–A) design strategy to synthesize a Q–D–A type polymer with a low bandgap of 1.30 eV, using *p*-AQM as the Q moiety. The resonance between the quinone units and the electroactive aromatics facilitates the lowering of the HOMO and LUMO energy levels of the polymer, while increasing the double bonding properties between cyclic π-units and enhancing the coplanarity and rigidity of the polymer backbone, which results in the polymer exhibiting a high hole 5.10 $cm^2\ V^{-1}\ s^{-1}$.

Appropriate increase in side chain length or introduction of branched side chains may improve the solubility and

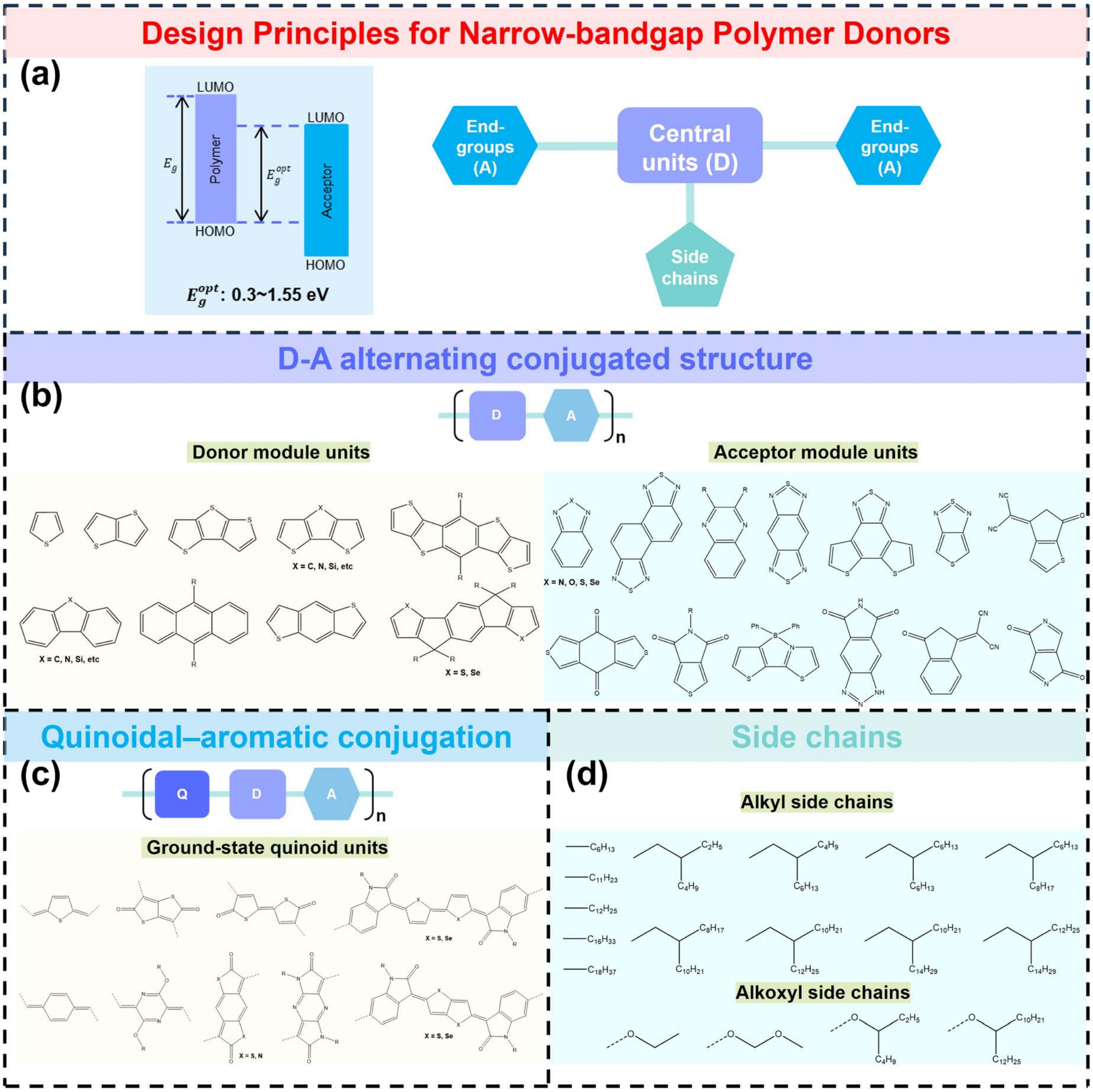

Fig. 4 Design principles for narrow-bandgap polymer donors. (a) Energy level diagrams of heterojunctions formed from polymer donors and acceptors and the compositional structure of the polymers. (b) Typical donor and acceptor modular units in D–A alternating conjugate structures. (c) Typical ground-state quinoid units in quinoidal–aromatic conjugate structures. (d) Several typical alkyl side chains and alkoxy side chains in the polymer composition.

processability of polymers in organic solvents. Moreover, it enhances intermolecular π–π interactions, which may promote the ordered arrangement of polymer chains and increase their long-range ordering (crystallinity).[77] Fig. 4(d) illustrates some typical side chains in polymer design, including alkyl and alkoxy side chains. Zhang *et al.*[100] modified the conjugated side chain of PBT with 3,4-ethylenedioxythiophene (EDOT) and found that the EDOT side chain significantly suppressed the dark current of the device. The photodetector exhibits a dark current at ± 2.0 V high rectification ratio (10^6–10^7) at ± 2.0 V, and has a good photodetectivity of 10^{13} Jones in the spectral range of 300–900 nm.

All-polymer detectors have great potential for application in the field of flexible electronics. The introduction of cyano(CN) groups, fluorine atoms, or strong electron-absorbing units into the polymer acceptor backbone to enhance the intramolecular charge transfer ability of the acceptor can significantly reduce the LUMO level and slightly decrease the HOMO level, resulting in a red-shift of the polymeracceptor absorption band. Chen *et al.*[101] used dicyanomethyl-substituted benzothiadiazole (DCBT) as the acceptor unit, and alkyl-substituted 1,1′-[2,5-dithiophen-2-ylfuran-3,4-diyl]bis[heptadecane] (4TOC) as the donor unit, and constructed the P4TOC-DCBT polymer acceptor with an optical band gap of 1.13 eV. The flexible OPD based on PDPPTDTPT:P4TOC-DCBT exhibits a high detection performance with D^* surpassing 10^{12} Jones from 650 to 1070 nm and a low J_d of 1.7×10^{-11} A cm^{-2} at zero bias, which is attributed to the fact that the CN stabilises the conformation of the polymer

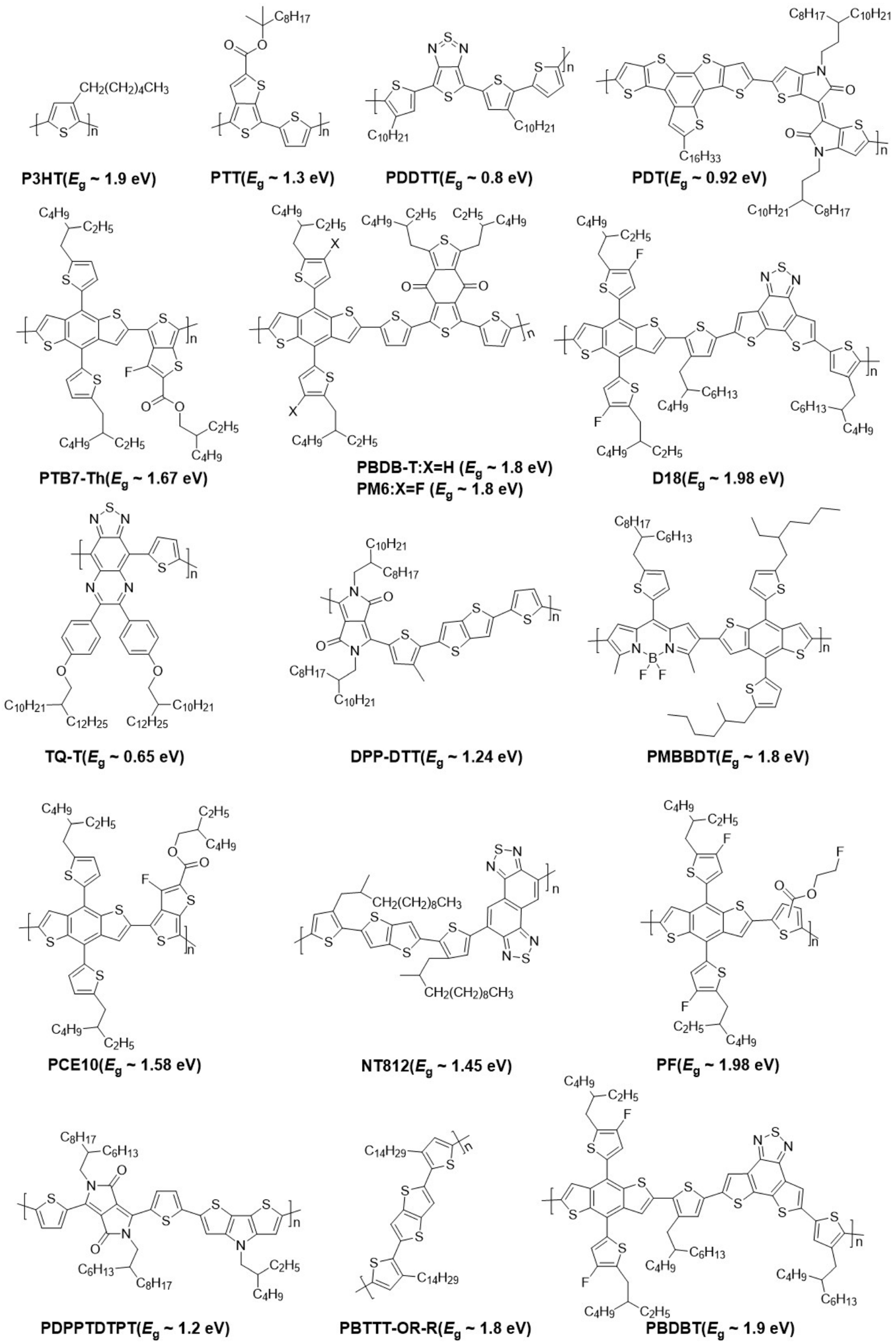

Fig. 5 Polymer donors used in NIR–SWIR OPDs in recent years.

backbone, and the fused ring 4TOC provides a rigid and planar molecular structure. Wang *et al.*[91] synthesized three novel polymeric receptors, namely PY-DTT, PY-DTP-C and PY-DTP-Ph, based on the electron-deficient units of dithiophene thiophene (DTT) and dithienopyrrole (DTP) using alkyl and aryl side chains as linking units. Poly [(2,6-(4,8-bis(5-(2-ethylhexyl-3-

Table 1 Progress of NIR–SWIR OPDs with polymers as donors in recent years

Device type	Hetero-junction type	Active layer	Spectral response /Target (nm)	EQE (%)	D^* (Jones)	R (A W^{-1})	J_d (A cm^{-2})	LDR (dB)	Response speed	Year	Ref.
PD	BHJ	PTB7-Th:CO1-4Cl	750–1000/940	876	3.31×10^{13}@−2 V	0.5	2×10^{-7}	148	−3 dB 240Hz	2019	78
PD	BHJ	P3HT:PC$_{61}$BM	300–800/600	—	1.48×10^{14}@−20 V	45	2.53×10^{-7}	60	t_r 0.3 s t_d 0.42 s	2019	79
PD	BHJ	DPP-DTT:IR dye	600–1600/1050	—	10^9@0 V	0.012	6.67×10^{-9}	—	—	2020	80
PT	BHJ	PTB7-Th:IEICO-4F:PC$_{71}$BM	488–1064/850	8.3×10^8	2.4×10^{13}@0 V	6×10^6	—	—	−3 dB 400Hz	2021	81
PT	PHJ	D18:Y6	300–1000/805	80	1.97×10^{14}@−2 V	0.508	2.1×10^{-11}	83	t_r 15 µs t_d 14 µs	2021	36
PT	BHJ	PQT-12:F4-TCNQ	400–2600/2000	10^8	3.12×10^{14}@0 V	2.75×10^6	—	—	t_r 9.7 ms t_d 10 ms	2021	23
PT	BHJ	PMBBDT:Y6	300–900/810	16 400	9.6×10^{10}@5 V	—	10^{-8}	124	t_r 79 µs	2021	82
PD	BHJ	PF:IT-4F	300–800/750	70	3.39×10^{13}@−2 V	0.37	3.7×10^{-10}	120	−3 dB 56.3 kHz	2021	83
PD	BHJ	TQ-T:IEICO-4F	400–1800/1200	—	2×10^1@−2 V	0.03	8.4×10^{-6}	43.9	t_r 6.6 µs t_d 7.3 µs	2022	84
PD	BHJ	PM7-D5:Y12	300–1000/720	72	3.3×10^{13}@−2 V	0.42	3.6×10^{-9}	150	−3 dB 82.9 kHz	2023	85
PD	BHJ	PTzBI-EHp-BTBHT0.1:N2200	350–750	—	2.94×10^{13}@−0.1 V	—	10^{-11}	—	—	2023	86
PD	BHJ	P3HT:F4TCNQ	500–1800/1800	77 100	1.11×10^{11}@−10 V	1120	6×10^{-7}	40	t_r 267 ms t_d 365 ms	2024	87
PD	BHJ	PBDTTT-OFT:N2200	300–900/730	29	6.2×10^{11}@−2 V	0.17	2.5×10^{-9}	—	t_r 3 µs t_d 8 µs	2024	88
PD	BHJ	PTB7-Th:COTIC-4F	300–1140/1100	59	6.2×10^{12}@−0.1 V	0.52	3.0×10^{-9}	133	−3 dB 550 kHz	2024	35
PD	PHJ	PM6-Br50:Y6	400–1000/780	70	4.27×10^{13}@−0.5 V	0.486	4.0×10^{-10}	73.7	t_d 1.8 ms	2024	89
PD	BHJ	PDPPTDTPT:P4TOC-DCBT	650–1070/940	13	1.13×10^{12}@−0.1 V	0.11	1.7×10^{-11}	125	t_r 1.4 µs t_d 0.6 µs	2024	90
PT	BHJ	PM6:PY-DTP-Ph	300–900/810	57%	5.4×10^{13}@−0.1 V	0.29	9.2×10^{-11}	105	t_r 1.2 µs t_d 22 µs	2024	91

fluoro)thiophen-2-yl)-benzo[1,2-*b*:4, 5-*b*′]dithiophene))-*alt*-(5,5-(1′,3′-di-2-thienyl-5′,7′-bis(2-ethyl-hexyl)benzo[1′,2′-*c*:4′,5′-*c*′]dithiophene-4,8-dione))] (PM6):PY-DTP-Ph OPD exhibited a high responsivity of 0.3 A W^{-1} and a low J_d (−0.1 V) of 9.2 × 10^{-11} A cm^{-2}, which may be attributed to the good molecular ordering of J-aggregates and stronger intermolecular interactions of PY-DTP-Ph.

3.2 Organic small molecules

In 1992, Sariciftci *et al.*[55] discovered the rapid electron transfer between donor polymer and acceptor fullerene under light, after which the photoactive layers composed of polymer and fullerene derivatives have been rapidly developed in the field of organic photovoltaic devices and photodetectors. Representative materials of fullerene derivatives include $PC_{61}BM$, $PC_{71}BM$, and ICBA. Throughout the fullerene era, most of the work focused on developing IR-absorbing p-type polymer donor materials due to the difficulty in modifying the globular structure of fullerenes and the weak light absorption in the near-infrared region of the fullerene acceptors. In 2012, non-fullerene small molecule acceptors (SMAs) appeared and rapidly became a new trend due to their broad absorption spectra, easily modifiable molecular energy levels and chemical structures.[31,102] Fig. 6 illustrates the receptor small molecules involved in literature reports in recent years. Table 2 summarizes the research progress of NIR-SWIR OPDs with small molecules as receptors in recent years. Many excellent reviews[103,104] summarize the design strategies of small molecules. Generally, SMAs mainly consist of an electron-donating unit D, an electron-donating π-bridge unit, and an electron-absorbing unit A. Strategies to further redshift the absorption spectra of small-molecule acceptors to the IR region usually include enhancing the electron-donating ability of the D unit or the electron-absorbing ability of the A unit, introducing quinone-type units, enhancing the planarity of the molecule, and optimizing molecular stacking.[105]

The molecular central units of SMAs are designed as D–A or quinone-conjugated structures that give alternating conjugation to the acceptor unit, which has been shown to be effective in achieving SWIR absorption.[106] Cong *et al.*[32] developed an A–D–A′–D–A type ultranarrow-bandgap acceptor molecule (300–1550 nm), CS-1, using benzothiadiazole (BBT) as the electron-deficient unit A′. The strong intramolecular charge-transfer effect between the donor and acceptor units extends the spectral detection range of PTB7-Th:CS-1-based OPD to 1.4 μm. Duan's group designed and synthesized the A–D–A′–D–A type receptor DPPSe-4Cl with a film-onset absorption edge of 1120 nm using selenophene-based pyrrolidopyrrolidone (Se-DPP), which contains a quinone structure and excellent planarity, as the central A′-unit (Fig. 7(b)).[107] After that, the team employed the benzodipyrro-lidone (BDP) unit as the Q-unit and synthesised the n-type small molecule BDP4Cl with the film onset absorption edge red-shifted to 1240 nm, which corresponds to an optical band gap of only 1.00 eV[108](Fig. 7(c)). Non-covalent conformation locks inhibit conformation distortion, enhance the rigidity and coplanarity of the receptor molecular skeleton, and thus improve carrier mobility through intramolecular weak interaction forces (such as S⋯O, N⋯S, N⋯H, *etc.*).[109–111] Duan's team utilized benzotriazole and thiadiazole (TBz), which has a stronger quinone resonance effect, and synthesized the n-type small-molecule semiconductor TBzIC with an even smaller optical band gap (0.97 eV).[112] As shown in Fig. 7(d), TBz units also constructed non-covalent conformational locks of S⋯N and N⋯H, which increased the crystallinity of the molecule. The OPD with poly[4,8-bis-substituted-benzo[1,2-*b*:4,5-*b*′] dithiophene-2,6-diyl-*alt*-4-substituted-thieno[3,4-*b*]thiophene-2,6-diyl] (PBD-TTT):TBzIC as the active layer exhibited an excellent specific detectivity of more than 10^{13} Jones from 0.50 μm to 1.21 μm. The enhancement of molecular planarity and optimization of molecular stacking can effectively promote the absorption of small molecules with redshift. Huang's research group used helically conjugated core donor units (SPDT) to construct two types of A–D–A SMA, namely SPT-4F (E_g = 1.09 eV) and tSPT-4F (E_g = 1.17 eV).[113] Compared with PT-4F without helical conjugation, the orthogonal helical conjugation planes enhance the light absorption of SPT-4F and tSPT-4F above 1000 nm, and the absorption spectra are redshifted. Impressively, the PTB7-Th:tSPT-4F based device has a D^* of 1.25 × 10^{13} Jones at 1010 nm.

The incorporation of polarizing groups, such as fluorine atoms , N–B ← N unit and CN, into the end-groups of small molecules, has been demonstrated to augment the electron-withdrawing capability of the A-unit. This strategy enables the precise calibration of the energy levels within small molecules. Fig. 7(e) demonstrates that Zhang *et al.*[28] utilized a di-fluorination approach on the terminal units of Y-QC to synthesize narrow bandgap SMAs with lower LUMO energy levels, Y-QC4F. The fluorinated structural modification promotes the molecules to be orderly and compactly stacked, which red-shifts the onset of the molecule's absorption to a wavelength as low as 1.5 μm, and suppresses the Y non-radiative complexation in the QC4F films. As depicted in Fig. 7(f), Liu's team[14] obtained a TF-BODIPY tetramer with a band gap of 1.02 eV by introducing a resonant N–B ← N unit and an electron-deficient pentafluorophenyl. The prepared poly[(2,6-(4,8-bis(5-(2-ethylhexyl)thiophen-2-yl)-benzo[1,2-*b*:4,5-*b*′]di-thiophene))-*alt*-(5,5-(1′,3′-di-2-thienyl-5′,7′-bis(2-ethylhexyl)benzo[1′,2′-*c*:4′,5′-*c*′]dithiophene-4,8-dione)] (PBDB-T): NBN-2 device exhibits SWIR photoresponse in the wavelength range of 0.3–1.3 μm with D* of 1.04 × 10^{12} Jones at 1.12 μm.

Furthermore, the optimization of the π-bridges of SMAs has been shown to enhance intramolecular charge transfer (ICT) and consequently reduce the band gap. Zhang *et al.*[114] have designed A–π–D–π–A type SMAs with BFIC by using FTT, which is a weakly electron absorbing π-bridge(Fig. 7(g)). FTT not only prolongs the conjugated system and enhances intramolecular charge transfer, but also regulates the molecule *via* fluorine atom-induced non-covalent interaction stacking, starting the absorption onset edge of BFIC to 1050 nm (E_g = 1.18 eV). Shao *et al.*[115] synthesized TPIC-4F by optimizing the π-bridge of TSIC-4F with TPy. The presence of S⋯N interactions in the TPy unit contributes to the enhancement of intramolecular charge transfer and quinone-type structural resonances, resulting in

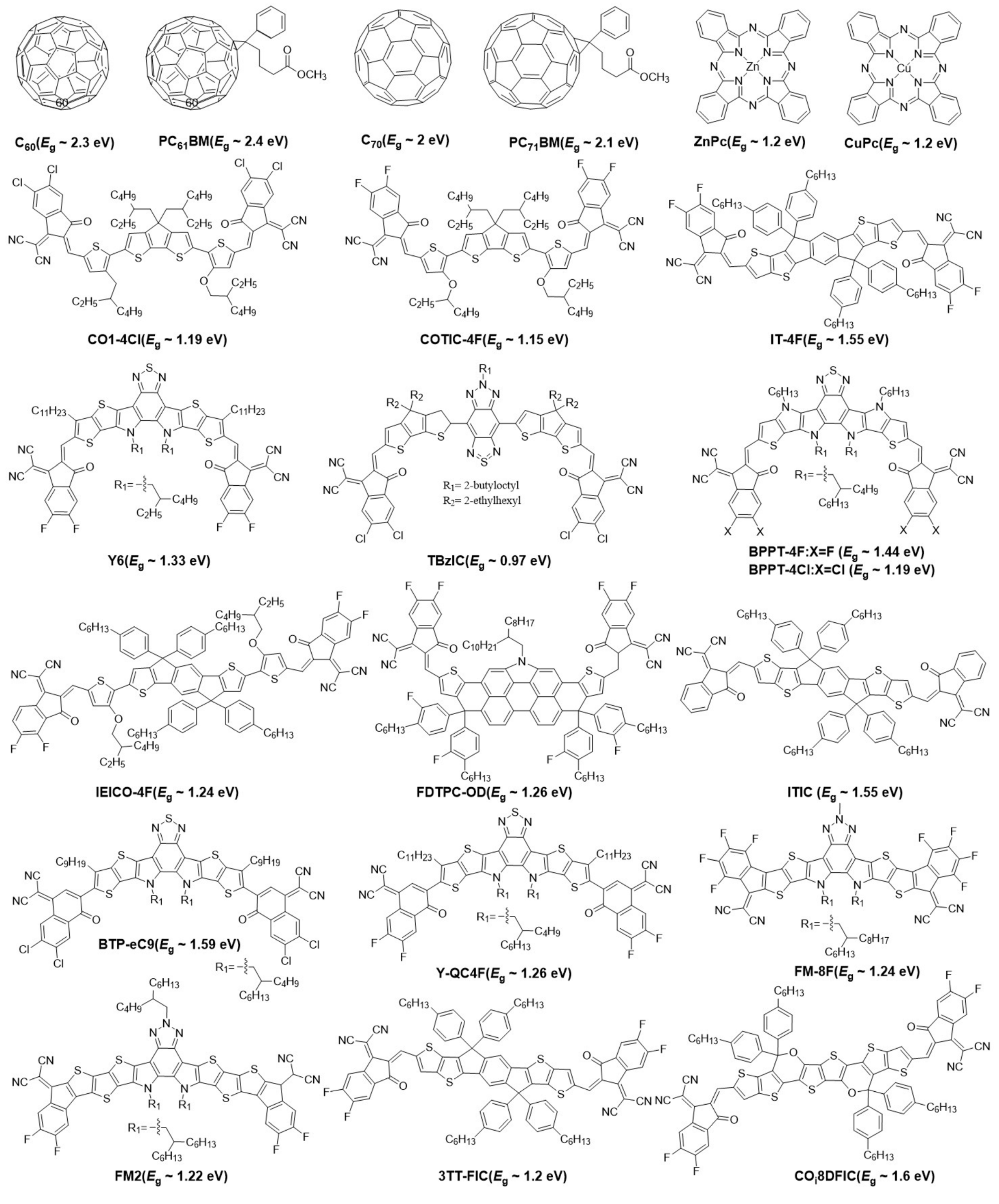

Fig. 6 Small molecule receptors used in NIR-SWIR OPDs in the last five years.

the significant red-shift (1015 nm) in the absorption of the TPIC4F film.

In addition, the alkyl side chain groups attached to the molecular skeleton can also improve the solubility and crystallinity of the molecules, and limit the molecular aggrega-tion. Peng *et al.*[116] synthesized two SMAs, TTz3 and TTz4, by introducing alkoxy/alkylthio side chains onto thiazole–thiazole (TTZ). As demonstrated in the Fig. 7(h), TTz3 and TTz4 have optical bandgaps of 1.42 eV and 1.50 eV respectively, which are smaller than the 1.65 eV of TTz. This phenomenon is attributed to the formation of multiple non-covalent conformational locks of N⋯S, S⋯O, and S⋯S between the alkoxyl/alkanethio side chains and the TTz. These locks effectively enhanced the intramolecular charge transfer and planarity. Huang's group[117]

Table 2 Progresses of NIR-SWIR OPDs with small molecules as receptors in recent years

Device type	Hetero junction type	Active layer	Spectral response/ Target(nm)	EQE (%)	D^* (Jones)	R (A W^{-1})	J_d (A cm^{-2})	LDR (dB)	Response speed	Year	Ref.
PD	BHJ	PTB7-Th:ITIC	300–1000/840	—	9.73×10^{11}@0 V	—	1.94×10^{-9}	197	t_r 149 ns	2021	118
PD	PHJ	D18/Y6	300–1000/805	80	1.97×10^{14}@0 V	0.499	2.1×10^{-11}	83	t_r 15 μs t_d 14 μs	2021	36
PD	BHJ	PTB7-Th:FDTPC-OD	300–1000/880	60	2.5×10^{11}@0 V	0.4	—	78.1	−3 dB 11.78 kHz	2022	119
PD	BHJ	PBDB-T:BPPT-4F	300–1000/870	50	1.3×10^{13}@−1 V	0.35	—	200	—	2022	120
PD	BHJ	PTB7-Th:COTIC-4F:Y6	780–1070/1050	53	1.29×10^{13}@−0.1 V	0.45	5.6×10^{-10}	150	t_r 8 μs t_d 8 μs	2022	121
PT	Single	TDPPQ	365–940/760	—	5.26×10^{13}@0V	9.2×10^{5}	—	—	—	2022	24
PD	Single	Y6	400–1000/855	22.1	2.74×10^{12}@−3 V	0.151	9.5×10^{-9}	87	t_r 7.9 μs t_d 14 μs	2023	122
PD	Single	IT-4F	400–1000/745	28.1	3.11×10^{12}@−3 V	0.169	9.2×10^{-9}	—	t_r 7.3 μs t_d 16 μs	2023	122
PD	BHJ	PBDB-T:FM2	300–1040/880	5	4.65×10^{13}@0 V	0.372	2.0×10^{-10}	—	t_r 49 μs t_d 14 μs	2023	27
PD	BHJ	PolyTPD:2TT-oC6B:PC$_{61}$BM	400–900/830	—	3×10^{11}@0 V	0.027	—	111	t_r 83 μs t_d 95 μs	2023	123
PD	BHJ	TPD-3:Y6-Se-HD	320–1090/860	6475	6.48×10^{12}@0 V	44.9	2.7×10^{-11}	55	−3 dB 45.38 kHz	2023	124
PD	BHJ	PM6:3TT-FIC	450–1000/850	54	1.45×10^{13}@0 V	0.36	7.0×10^{-10}	103	t_r 1.6 μs t_d 1.2 μs	2023	125
PD	BHJ	PBDT-TT:TBzIC	300–1400/1050	25.5	1×10^{13}@0 V	0.37	2.4×10^{-10}	106	t_r 8.3 μs t_d 6.9 μs	2024	112
PD	BHJ	PTB7-Th:Y-QC4F	400–1500/1160	13.39	1.68×10^{12}@0 V	0.12	2.4×10^{-8}	77	t_r 36 μs t_d 36 μs	2024	28
PD	BHJ	PBDB-T:PZF-V:PY-IT	300–1000/830	65	8×10^{12}@0 V	0.44	7×10^{-9}	145	−3 dB 220 kHz	2024	126
PD	BHJ	D18:FM-8F	300–1100/970	—	1.44×10^{12}@0 V	0.46	1.0×10^{-9}	—	t_r 0.46 ps t_d 3.7 ps	2024	127
PD	BHJ	PM6:CH17	400–900/880	85	$>10^{12}$@0 V	—	4.1×10^{-11}	130	t_r 91 ns t_d 102 ns	2024	128
PD	BHJ	PTB7-Th:CS-1	300–1400/1300	1.47	2.96×10^{10}@0 V	0.015	4.32×10^{-9}	91.9	t_r 5.8 μs t_d 7.4 μs	2025	32
PD	BHJ	PCE-10:COTIC-4F:BFDO-4F	300–1200/820	3484	1.13×10^{12}@1 V	23.4	—	83	t_r 2.37 ms t_d 0.58 ms	2025	30
PD	BHJ	PM6:CT-Cl	620–1000/950	—	5.8×10^{11}@0 V	0.33	2.1×10^{-11}	—	—	2025	129
PT	BHJ	PDVT-10:TMBP-F4TCNQ	1000–1700/ 1060	—	1.6×10^{13}@0 V	801@−50 V	—	—	t_r 0.68 s t_d 0.97 s	2025	34

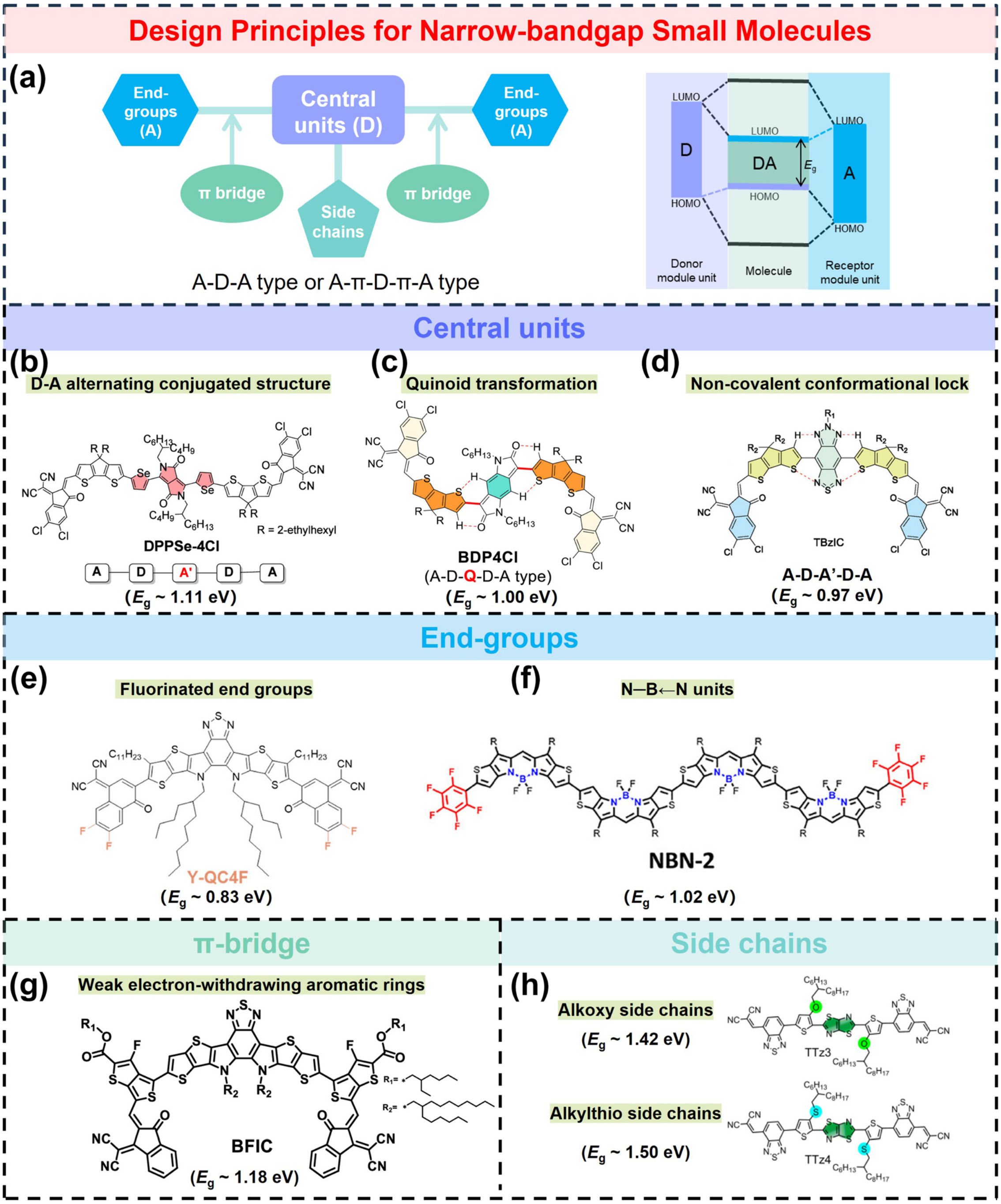

Fig. 7 Design principles for narrow-bandgap small molecules. (a) Designed structures of small molecules and bandgap tuning by tuning energy levels. Central unit modification for bandgap reduction: (b) Design D–A alternating conjugated structures, *e.g.* the DPPSe-4Cl molecule. Reproduced from ref. 107 with permission from American Chemical Society, copyright 2024. (c) Introduce quinone structures, *e.g.* the BDP4Cl molecule. Reproduced from ref. 108 with permission from Wiley-VCH, copyright 2024. (d) Introduce non-covalent conformational locks, *e.g.* the TBzIC molecule. Reproduced from ref. 112 with permission from Cell Press, copyright 2024. End-group modification: (e) Fluorinate end-groups, *e.g.* the Y-QC4F molecule. Reproduced from ref. 28 with permission from Wiley-VCH, copyright 2024. (f) Introduce N—B ← N units, *e.g.* the NBN-2 molecule. Reproduced from ref. 14 with permission from Wiley-VCH, copyright 2025. π-bridge optimization: (g) introduce weakly absorbing aromatic rings, *e.g.* the BFIC molecule. Reproduced from ref. 114 with permission from American Chemical Society, copyright 2022. Side chain engineering: (h) introducing long side chains, *e.g.* the TTz3 and TTz4 molecules. Reproduced from ref. 116 with permission from American Chemical Society, copyright 2019.

changed the solubility of the receptor DPA by adjusting the length of the alkyl side chain, and also accurately controlled the molecular filling mode of the solid state by combining the intermolecular interactions of C═O⋯H and S⋯F. Zhu's research group[140] designed and synthesized an asymmetric receptor molecule with a phenylalkyl side chain, namely Z8. Phenyl side chains can participate in intramolecular and intermolecular interactions, contributing to the π–π packing and exciton delocalization of molecules.

In recent years, squaraine (SQ) dyes, characterized by a unique D–A–D zwitterionic resonance structure, have shown considerable promise for broadband infrared detection.[141] This capability stems from their ability to exhibit red-shifted absorption spectra *via* modulation of the intramolecular push–pull electron effects between donor and acceptor units. Csucker *et al.*[142] synthesized a D–A–D structured SQ dye, RSQ2, by incorporating rhodamine, a strong electron-withdrawing group, with a diphenylamine-substituted benzothiophene donor. This molecular design resulted in a solution-phase absorption peak red-shifted to 1165 nm. Similarly, He *et al.*[143] reported two novel ladder-type polycrystalline materials, PSQ-IDT and PSQ-IDTT, prepared by linking pyrrolic squaraine (PSQ) units *via* ladder-type conjugated π-bridges based on indacenodithiophene (IDT) and indacenodithieno[3,2-*b*]thiophene (IDTT). Organic photodetectors (OPDs) based on both polycrystalline films demonstrated a broad detection range from 400 to 1000 nm and achieved high specific detectivity (D^*) exceeding 10^{11} Jones in self-powered mode. In another study, He *et al.*[144] developed a carbazole-bridged polysquaraine, PSQ-2,7-Cz. The enhanced molecular planarity and extended conjugation length significantly suppressed the dark current density to 2.07×10^{-11} A cm^{-2}, while yielding a detectivity greater than 10^{13} Jones within the 650–950 nm wavelength range under self-powered operation. On the other hand, controlling the molecular aggregation behavior of SQ derivatives can mitigate localized clustering and improve charge carrier transport. For instance, Kim *et al.*[145] described a SQ-based donor material that self-assembles into J-aggregates through intermolecular charge-transfer interactions, yielding a narrow absorption peak at 1040 nm (FWHM = 85 nm) and an external quantum efficiency (EQE) of 12.3% at 1050 nm.

The structural characteristics of organic molecules, including donor–acceptor (D–A) units, conjugation length, and side-chain structure, directly influence their energy level arrangement and crystallisation behaviour, thereby regulating dark current generation. Dark current primarily originates from thermally excited carriers injected from electrodes and recombination processes facilitated by internal defect states (trap states) within the material. The molecule's HOMO and LUMO energy levels determine the barrier height for charge injection from electrodes into the active layer. Strong electron-withdrawing groups, such as fluorine substituents[146] and cyano groups,[147] lower the molecular HOMO energy level, thereby increasing the charge injection barrier and suppressing dark-state current. The planarity and conjugation length of the molecular backbone determine the degree of order in intermolecular stacking. A highly planar conjugated skeleton helps reduce grain boundary defects and trap states, thereby suppressing trap-assisted dark current. Zhang *et al.*[27] designed an n-type fully fused molecular ring FM2, whose structure comprises 14 π-conjugated rings with D–A characteristics. Owing to its extensive π-conjugated system and rigid molecular backbone, FM2 exhibits robust near-infrared absorption exceeding 1000 nm and a dark current density as low as 2.01×10^{-10} A cm^{-2}. Furthermore, the length and branching degree of molecular side chains significantly influence the phase-separated morphology of donor–acceptor blend films.[83,148] Excessively long side chains may induce severe phase separation, while overly short chains reduce molecular solubility; high branching may cause aggregation disorder. Rational design of side chain length and volume facilitates the formation of nanoscale phase separation, minimising trap states and thereby reducing dark current. Cho *et al.*[149] discovered that by controlling the length and linearity of the acceptor molecule's side chain, COT-Oct with linear short chains and PTB7-Th could form uniform phase-separated morphologies. Their dark current was as low as 8.18×10^{-9} A cm^{-2}, representing a tenfold reduction compared to branched-chain and long-chain acceptor materials.

The above studies demonstrate the rapid development of broad-spectrum infrared photodetectors. In recent years, the demand for narrowband IR detectors has increased in wavelength-selective sensing, chemical analysis, and emerging artificial intelligence networks.[150,151] Due to the wide spectral response range of inorganic semiconductors, conventional inorganic narrowband detectors need to be combined with external colour prisms or filters to obtain detection results. However, this inevitably increases the fabrication complexity, production cost and size of the device, and also limits the response speed and LDR of the detector. Organic semiconductors can be designed to selectively absorb optical radiation by designing the molecular and device structure, and thus there is an increasing amount of research in developing narrowband high-performance OPDs. Four main design strategies are (1) using narrow-band light-absorbing materials, such as J-type aggregated squarate dyes,[145,152] (2) achieving self-filtering by employing a layered structure with a thick layer of a large bandgap donor and a thin layer of a small bandgap acceptor,[130] (3) using an optical microcavity to increase charge-transfer (CT) absorption at specific wavelengths,[132,134,153] and (4) using a thick active layer to achieve a charge collection narrowing (CCN).[135] Table 3 clearly shows the research progress of materials used in narrow-spectrum IR photodetectors in recent years, where FWHM (full width at half peak) denotes the sensitive detection performance of narrow-spectrum photodetectors for light of a certain wavelength.

3.3 Organic–inorganic hybrid materials

In recent years, numerous research teams have conducted in-depth studies to address the challenges of low D^*, low EQE and high dark current in organic infrared detection. A number of innovative active layer design strategies have been proposed, including the compounding of inorganic materials such as

Table 3 Research progress of narrow-spectrum IR OPDs in recent years

Device type	Hetero junction type	Active layer	Spectral response/ FWHM (nm)	EQE (%)	D^* (Jones)	R ($A\ W^{-1}$)	J_d ($A\ cm^{-2}$)	LDR (dB)	Response speed	Year	Ref.
PD	PHJ	NT812/Y6	860/72	89	1.2×10^{13}@−0.1 V	0.43	2×10^{-10}	—	—	2020	130
PD	PHJ	DT-PDPP$_2$T-TT/Y6	910/43	89	7.5×10^{12}@−0.1 V	0.22	5×10^{-10}	—	—	2020	130
PD	PHJ	DT-PDPP2TTT/IEICO-4F	940/66	89	1.6×10^{13}@−0.1 V	0.24	1×10^{-10}	—	—	2020	130
PD	BHJ	SQ-H:PC$_{61}$BM	1040/59	12.30	4×10^{10}@0 V	0.1	—	100	−3 dB 300 kHz	2021	131
PT	BHJ	ZnPc :C60	843/33	450	10^{11}@−5 V	—	—	—	t_r 941 μs t_d 613 μs	2021	132
PT	BHJ	P3HT:PC$_{71}$BM	660/34	1120	6.4×10^{11}@−10 V	6	—	150	t_r 0.2 s t_d 0.6 s	2021	133
PD	BHJ	PBTTT-OR-R:PC$_{61}$BM	842/30	18	3.2×10^{11}@0 V	—	2.3×10^{-6}	—	—	2021	134
PD	BHJ	PCE10:COTIC-4F	1096/50	18	6.59×10^{12}@0 V	—	—	100	−3 dB 24.4 kHz	2022	135
PD	BHJ	PM6:Y6-FAMAPbI$_3$	850/100	200	3×10^{13}@0 V	1.5	2.0×10^{-10}	150	t_r 5.6 μs t_d 6.1 μs	2023	136
PT	BHJ	P3HT:PC$_{61}$BM	650/25	4.82×10^4	6.92×10^{14}@−60 V	—	4.16×10^{-7}	120	t_r 70 ms t_d 106 ms	2024	137
PD	BHJ	PBDBT:Y6	830/30	—	1.4×10^{10}@0 V	0.12	2.73×10^{-7}	55	t_r 28 μs t_d 24 μs	2024	138
PD	BHJ	ranDPP-2TBT:IEICO-4F	916/68	—	10^{11}@−2 V	0.13	6.88×10^{-9}	107	t_r 9.5 μs t_d 11.1 μs	2025	139

chalcogenides and colloidal quantum dots with organic materials exhibiting high carrier mobility.[154] The halogenated metal chalcogenide combines organic and inorganic components and has the advantages of high light absorption coefficient, low exciton binding energy and high carrier mobility. Li *et al.* reported a high-performance photodetector with an active layer of P3HT/PDPP3T/CsPbBr$_3$, which has a broad response spectrum of 300–950 nm, a high sensitivity of 0.25 A W^{-1} and a fast response speed of 111 μs.[155] This is attributed to the integration of P3HT and PDPP3T on the chalcogenide nanowire arrays, which increases the light-harvesting efficiency, and the appropriate energy bands also facilitate the separation and transport of photogenerated carriers at the device interfaces. Shen and Hu's team[156] fabricated a photodetector based on CH$_3$NH$_3$PbI$_3$/PTB7-Th:F8IC. As illustrated in Fig. 8(a–c), it achieves broadband response spectra up to 1 μm, with an ultrafast response speed of 5.6 ns, and a wide linear dynamic range of 191 dB. Ding *et al.*[157] constructed broadband heterojunction PDs using ultraviolet (UV) luminescent concentrators (LC), chalcogenide (CsPbI$_3$:Er^{3+}) quantum dots, and BHJ (BTP-4Cl:PBDB-TF) layers as the UV, visible, and NIR photosensitive layers, respectively. The PD exhibited superior detection rates and stability in comparison to both commercial Si PD and other chalcogenide PDs over a broad spectrum ranging from 200 to 1000 nm.

Ternary hybrids formed by colloidal quantum dots (CQDs) and two organic materials are now widely used as the active layer in organic/inorganic hybrid photodiodes, as they combine the advantages of the broad spectral response of CQDs with the flexibility of organics to be processed over large areas. Based on the quantum size effect of nanocrystals, the size of the nanocrystals of colloidal quantum dots can be adjusted during the synthesis process to tune their spectral response to the infrared region.[158] PbS nanocrystalline quantum dots as sensitizers are capable of absorbing light up to about 1.8 μm, have high quantum efficiency in the near and shortwave infrared region, and are advantageous for large-area processing when composited with organic materials. As demonstrated in Fig. 8(d), Qiao *et al.*[159] leveraged the complementary absorption of CQD/organic hybrid structure (340–810 nm) and the unique absorption of CQDs in the NIR region, enabling commendable detectivity surpassing 10^{13} Jones across 400–1000 nm. The high performance, attributed to enhanced exciton dissociation efficiency, stemmed from efficient carrier transport in the CQD layer and effective charge transfer in the organic heterojunction (Fig. 8(e)). Rauch *et al.*[18] fabricated PbS:P3HT:PCBM active layer photodiodes with a high sensitivity of 0.16 A W^{-1} at 1220 nm and an EQE of up to 51%. P3HT and PCBM can promote the efficient dissociation of PbS quantum dot excitons and electron/hole transport, which makes the detector have a higher EQE value than the pure quantum dot device. Pejović *et al.*[37] reported a dual-band photodiode based on PbS CQDs and PTB7-Th:2,2′-((2*Z*,2′*Z*)-((5,5′-(4,4,9,9-tetrahexyl-4,9-dihydro-*s*-indaceno[1,2-b:5,6-*b*′]dithiophene-2,7-diyl)bis(4-(2-ethylhexyl)thiophene-5,2-diyl))bis(methanylylidene))bis(5,6-difluoro-3-oxo-2,3-dihydro-1*H*-indene-2,1-diylidene))dimalononitrile (IEICO-4F) organic absorber. The detector has a broad spectral response from 400 to 1600 nm and an EQE of up to 70 per cent in the NIR region with a fast response time of 10 μs.

Another prevalent combination of organic and inorganic materials is that of metal oxides (*e.g.* zinc oxide (ZnO),[160] titanium dioxide (TiO$_2$)) or sulphur metalized nanoparticles (*e.g.* cadmium selenide (CdSe)[161]) mixed with polymers in an active layer. Hou *et al.*[160] designed an inverted organic photodiode based on PTB7-Th:PC$_{61}$BM/ZnO with EQE of 72.2% and D^* of 9.11×10^{12} Jones at 730 nm. The hybrid heterojunction consisting of an inorganic semiconductor, copper thiocyanate

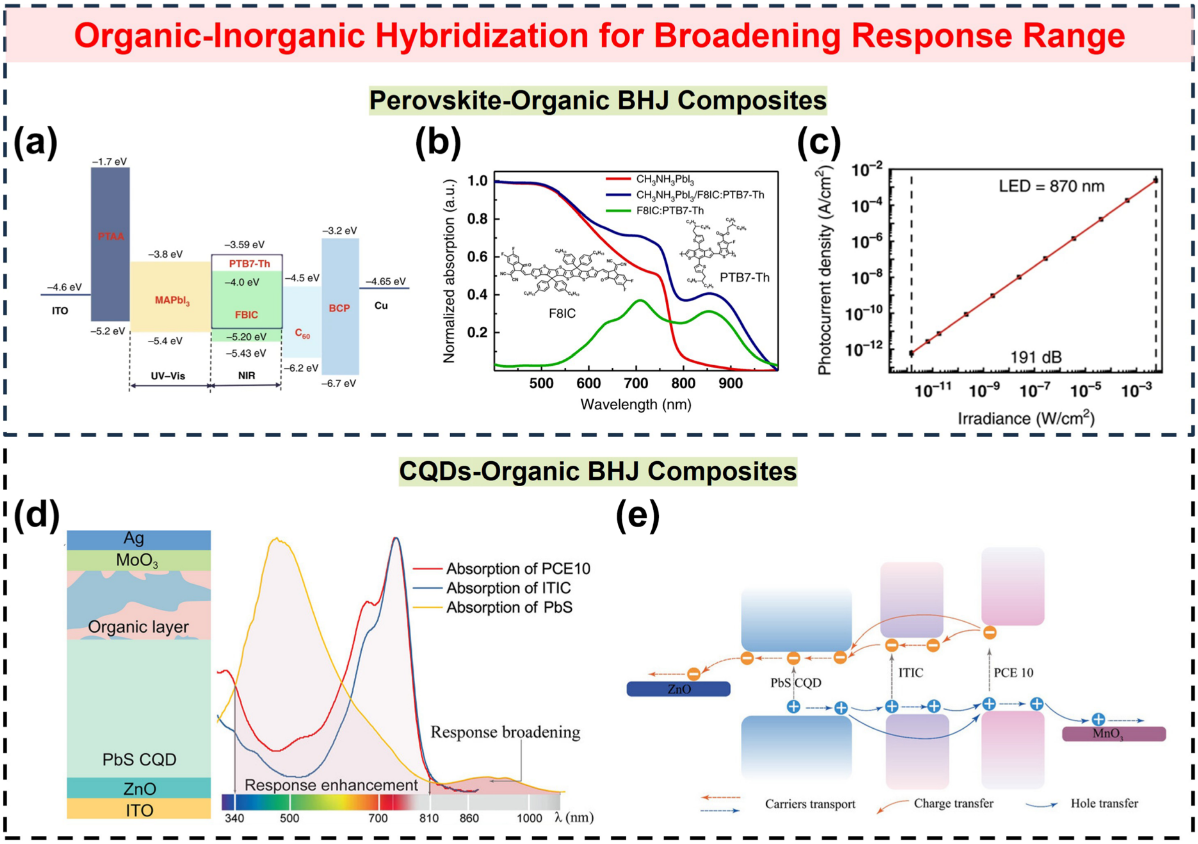

Fig. 8 Organic–inorganic hybridization strategies for expanding the spectral response range. (a) Energy level diagram, (b) absorption spectra of different active layers, and (c) LDR under 870-nm LED illumination of $CH_3NH_3PbI_3$/PTB7-Th:F8IC-based photodetector. Reproduced from ref. 156 with permission from Springer, copyright 2020. (d) Diagrammatic illustration of the device structure and absorption spectra, (e) diagrammatic illustration of the exciton/carrier dynamics of CQD/organic hybrid PDs. Reproduced from ref. 159 with permission from Wiley-VCH, copyright 2025.

(CuSCN), and an organic semiconductor also has a high light absorption coefficient in the NIR region. Flurin *et al.*[162] established that the CuSCN/2,2′-((2*Z*,2′*Z*)-((12,13-bis(2-ethylhexyl)-3,9-diundecyl-12,13-dihydro-[1,2,5]thiadiazolo[3,4-*e*]thieno[2″,3″:4′,5′]thieno[2′,3′:4,5]pyrrolo[3,2-*g*]thieno[2′,3′: 4,5]thieno[3,2-*b*]indole-2,10-diyl)bis(methanylylidene))bis(5,6-difluoro-3-oxo-2,3-dihydro-1*H*-indene-2,1-diylidene))dimalo-nonitrile (Y6) detector exhibits a wide spectral response range from 400 nm to 950 nm, with D^* of 9.97×10^{12} Jones and J_d of 5×10^{-9} A cm^{-2} at 810 nm and −0.5 V reverse bias.

4 Device optimization strategies for high-performance IR detection

A series of novel narrow bandgap organic materials have been developed in recent years, which have significantly expanded the spectral response range of infrared OPDs to 1500 nm and beyond. However, the majority of these devices demonstrate suboptimal detection performance, a phenomenon that may be attributed to an increase in dark current. The dark current is principally attributable to two origins: the leakage current at the interface between the electrode and the active layer (charge carrier injection) and the intrinsic dark current arising from the thermal diffusion of carriers within the active layer. The bandgap energy (E_g) of organic materials is typically large ($E_g > 1$ eV), leading to a negligible concentration of thermally generated carriers. Consequently, the majority of current research has concentrated on reducing the charge carrier injection rate. Inorder to reduce the dark current of the device and improve the detection performance, scientists have used many device structure optimization strategies, such as optimizing the active layer morphology, electrode materials and the interface between the electrode and the active layer.

4.1 Active layer

The active layer is the core of organic photodetectors, and a good active layer morphology can effectively improve the problems of exciton generation, transport, dissociation and charge complexation processes. Most organic infrared photodetectors use mixed donor and acceptor BHJ structures, but the presence of both donor and acceptor components near the anode and cathode interfaces in the device can cause strong reverse charge injection, which directly leads to high dark current density. To overcome this problem, scientists have proposed strategies such as crystal engineering,[163] optimizing molecular stacking using additives,[16,164] optimizing the hierarchical structure of the active layer,[165,166] thick bulk heterojunction and employing a ternary compensation strategy.[167,168]

Self-powered detectors have low dark current due to the absence of shunt leakage current and injected control limiting current.[169] By comparing the detection performance of NIR self-powered OPDs based on non-fullerene and fullerene receptors, Huang's group found that the low trap density property of the active layer plays a key role in reducing the dark current density and achieving high responsivity.[169] The active layer of PCE10:BTPV-4F-eC9 has a more densely packed π–π molecular stacking and lower crystalline disorder compared to that of PCE10:PC71BM, which reduces trap formation and carrier complexation.

Recently, crystal engineering has emerged as an effective methodology for constructing small-molecule optoelectronic functional materials.[163] Guan *et al.*[24] obtained n-type thiophene (TDPPQ) crystalline nanosheets by a solvent-phase interfacial self-assembly method. As shown in Fig. 9(a), the TDPPQ crystalline nanosheets-based organic transistor exhibits a high electron mobility of 2.1 cm^{-2} V^{-1} s^{-1} with a broad spectral response from UV (365 nm) to NIR (940 nm). Single crystals provide longer exciton diffusion lengths and low dark currents due to the intrinsic properties of no grain boundaries and defects, resulting in high responsivity and sensitivity.[170,171] Hu's group[15] prepared a two-dimensional single crystal film of a furan–thiophene quinoidal compound, TFT-CN, based on solution epitaxy. As illustrated in Fig. 9(b), the NIR phototransistor based on the TFT-CN single-crystal film exhibited a low dark current of about 0.3 pA and an ultrahigh detectivity of more than 6 × 10^{14} Jones. Cui *et al.*[172] reported a new fused diketopyrrolopyrrole (FDPP) derivative, FDPP-p-C6, and fabricated a phototransistor based on the FDPP-p-C6 single crystal (Fig. 9(c)). The transistor exhibits a high hole mobility of 0.2 cm^{-2} V^{-1} s^{-1} and a high responsivity in the 550–715 nm range, where the maximum photoresponsivity reaches 2.2 × 10^{3} A W^{-1}. Cocrystals refer to crystalline structures formed by two or more organic molecules mixed in specific ratios through non-covalent interactions. Compared with bulk heterojunction (BHJ) blends, the ordered arrangement of donors and acceptors in organic cocrystals creates a nanoscale D–A interpenetrating network, which enhances photon harvesting efficiency and improves charge carrier mobility.[173] Moreover, the grain boundary-free nature, minimal impurities, and defect-free characteristics of organic cocrystals significantly reduce the dark current density in photodetectors. Based on charge transfer (CT) interactions, orbital hybridization occurs between the HOMO of donors and the LUMO of acceptors, generating new excited states with ultranarrow optical bandgaps that extend the absorption of cocrystals into the short-wave infrared (SWIR) region.[174] Hu's research group[174] synthesized two-dimensional ZnTPP-C_{60} cocrystals using a simple and low-cost solid-phase epitaxy method, which were fabricated into planar photoconductor devices. These cocrystals demonstrated a specific detectivity of 3.77 × 10^{11} Jones and an external quantum efficiency of 376% at 800 nm. Yu *et al.*[173] reported a BFxTQ (X = 0, 1, 2, 4) co-crystal photodetector based on CT interactions. As shown in the Fig. 9(d), the LUMO energy level of the co-crystal decreases with an increase in the number of F atoms, resulting in a gradual narrowing of the energy gap from 3.26 eV to 0.98 eV. The detectivity of the BF_4TQ detector exceeds 10^{13} Jones over the wavelength range from 375 nm to 1064 nm, reaching a peak of 1.76 × 10^{14} Jones at 1064 nm.

When small molecules self-assemble from solution to the solid state, they typically form face-to-face stacked H-aggregation or head-to-tail aligned stacked J-aggregation. Más-Montoya *et al.*[175] found that the J-aggregation state decreases the energy level difference between LUMO and HOMO and broadens the absorption range of TDPPPy derivative molecules. Liu *et al.*[176] used ultrasonication to induce MTSIC (a organic molecule) to exhibit excellent J-aggregation, with the absorption band red-shifted from 624 nm to 790 nm. Qiao *et al.*[16] induced the J-aggregation of the acceptor molecules by using the electrostatic attraction between the volatile solid additive di-iodobenzene (DIB) and the acceptor molecules, 2,2′-((2*Z*,2′*Z*)-((12,13-bis(2-butyloctyl)-3,9-dinonyl-12,13-dihydro-[1,2,5]thiadiazolo[3,4-*e*] thieno[2″,3′:4′,5′]thieno[2′,3′:4,5]pyrrolo[3,2-g] thieno[2′,3′:4,5] thieno[3,2-*b*]indole-2,10-diyl)bis(methanylylidene))bis(5,6-di-chloro-3-oxo-2,3-dihydro-1*H*-indene-2,1-diylidene))dimalono-nitrile (BTP-eC9). As shown in Fig. 9(e), the J-aggregation enhanced the intermolecular π–π interactions, which is conducive to promoting molecular stacking order and charge separation, and significantly reduced the dark current density of the self-powered PM6:BTP-eC9 OPD (J_d = 63.5 pA cm^{-2}). As depicted in the Fig. 9(f), Liu *et al.*[177] utilized a terminal fluorination strategy to enhance the J-aggregate ratio and crystallinity of the acceptor TBT-V-F. The aggregation exhibited a propensity for promoted molecular π–π stacking and suppressed non-radiative energy loss, achieving a low dark current density as low as 7.30 × 10^{-12} A cm^{-2} in the TBT-V-F-based OPD. Gao *et al.*[179] introduced a small amount of ITIC units into the N2200 backbone to synthesize NTI, which reduced the excessive self-aggregation of N2200. The ordered stacking of NTI and mixing with J71 optimized the morphology of the active layer, and thus the J71:NTI-based detector had a low J_d of 1.6 × 10^{-11} A cm^{-2}.

In recent years, novel heterojunctions, including pseudo-planar heterojunction (*p*-PHJ) and ternary heterojunction, have been developed, leveraging the high detectivity of bulk heterojunction (BHJ) and the low dark current of planar heterojunction (PHJ). Active layers with low dark currents have attracted increasing attention. Jang *et al.*[29] fabricated a $PC_{71}BM$/PM6:BTP-4F-12 multiactive layer consisting of a single receptor layer and a bulk heterojunction (A/BHJ structure) by transfer printing, illustrated in the Fig. 9(g). The structure achieved low dark current (J_d = 1.68 × 10^{-9} A cm^{-2}) and fast response (t_d = 2.37 μs) by increasing the hole injection barrierand suppressing the trap sites within the interface. Yu *et al.*[180] constructed an interdigitated heterojunction (IHJ) detector based on D18-Cl/L8-BO by adding trace amounts of PY-IT acceptor into the D18-Cl donor solution to induce vertical infiltration of the top L8-BO acceptor solution into the underlying film. By increasing the PY-IT content to adjust film roughness and phase separation extent, the IHJ detector achieved reduced dark current (J_d =

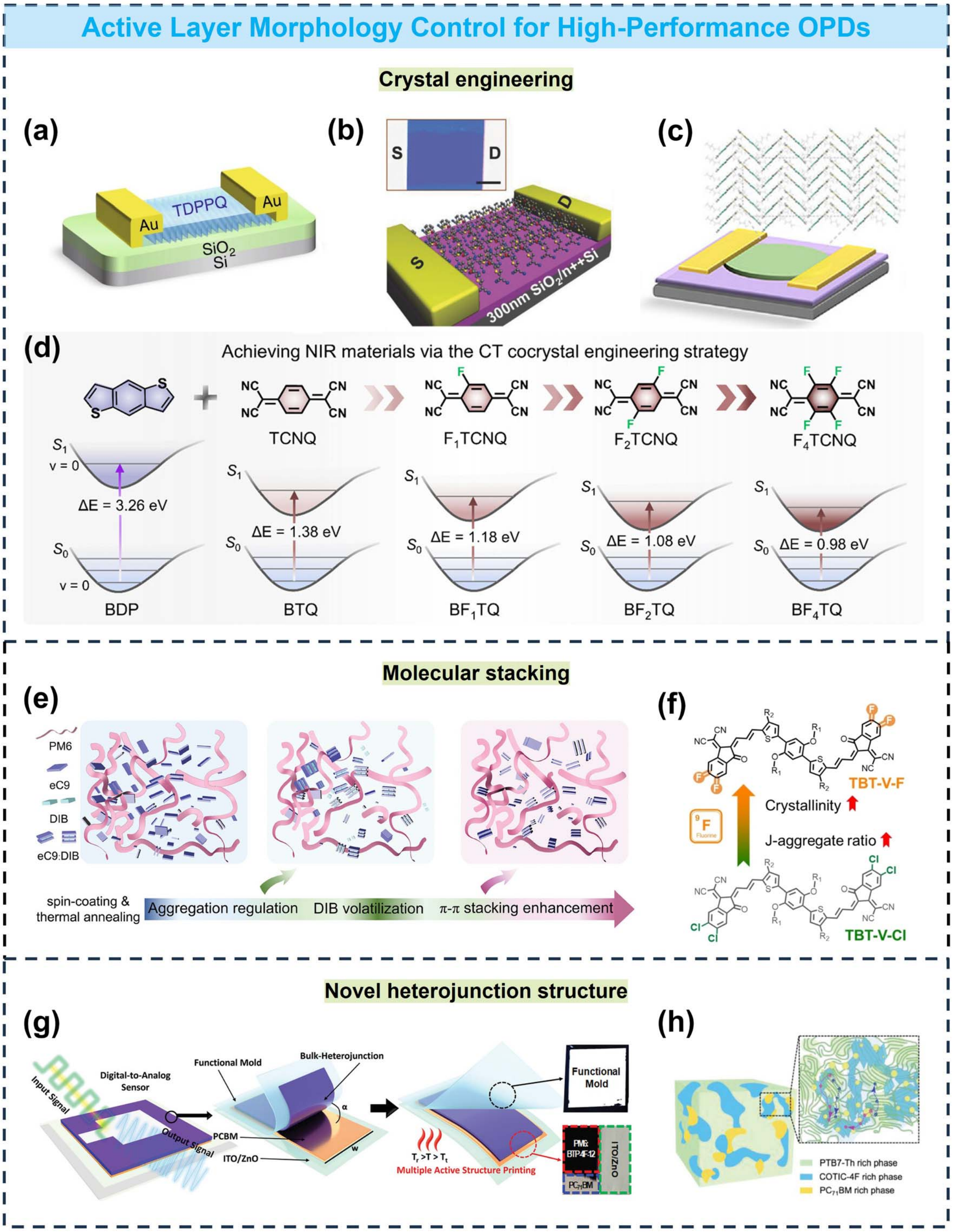

Fig. 9 (a) Schematic diagram of TDPPQ crystalline nanosheets-based organic transistor. Reproduced from ref. 24 with permission from Springer, copyright 2022. (b) Schematic illustration of the phototransistor based on TFT-CN single-crystal film. Reproduced from ref. 15 with permission from Wiley-VCH, copyright 2018. (c) Schematic diagram of single crystal phototransistor based on FDPP-p-C6. Reproduced from ref. 172 with permission from Wiley-VCH, copyright 2025. (d) Illustrations of energy level and optical bandgap values of the donor molecule of BDP and BF*x*TQ ($X = 0, 1, 2, 4$) CT cocrystals. Reproduced from ref. 173 with permission from American Chemical Society, copyright 2024. (e) Working mechanisms of DIB-induced J-aggregation of BTP-eC9. Reproduced from ref. 16 with permission from Wiley-VCH, copyright 2025. (f) Schematic of TBT-V-F to enhance the crystallinity and J-aggregation ratio by terminal fluorination. Reproduced from ref. 177 with permission from Wiley-VCH, copyright 2025. (g) Schematic diagram illustrating the transfer printing process for creating the A/BHJ structure. Reproduced from ref. 29 with permission from Wiley-VCH, copyright 2024. (h) Schematic of the microstructure and working mechanisms in the PTB7-Th:COTIC-4F:$PC_{71}BM$ ternary blend. Reproduced from ref. 178 with permission from Wiley-VCH, copyright 2023.

1.38×10^{-10} A cm^{-2}). Lim *et al.*[181] introduced a novel asymmetric acceptor, A-YBO-2Cl, as a third component into the PM6/Y6 system to construct a ternary *p*-PHJ configuration. The incorporation of the third component enhanced intermolecular packing, reduced thermally activated carriers, and the 500 nm-thick *p*-PHJ active layer suppressed charge injection under reverse bias. Consequently, the organic photodetector (OPD) based on PM6/Y6:A-YBO-2Cl achieved a dark current density as low as 1.06 pA cm^{-2}. As shown in the Fig. 9(h), Lou *et al.*[178] introduced $PC_{71}BM$ into the PTB7-Th:COTIC-4F binary system, accelerating charge transfer and exciton dissociation efficiency in the infrared range. Subsequently, PEI-Zn was employed as the ETL layer to eliminate pinholes, further reducing the dark current ($J_d = 3.82 \times 10^{-8}$ A cm^{-2}, at 0 V).

Increasing the thickness of the active layer can reduce dark current density, as studies[182] demonstrate that thicker bulk heterojunctions are less affected by defects, bubbles, and other imperfections. The EQE values of PTB7-Th:COTIC-4F active layers with varying thicknesses investigated by Nguyen's group,[35] demonstrating that thicker films enhance light absorption in photodetectors. The group also experimentally compared the detection performance of devices with active layer thicknesses of 245 nm and 655 nm. They found that the latter exhibited a lower J_d of 3.82×10^{-8} A cm^{-2} at −5 V, along with 35% EQE at 1150 nm and a high D^* of 2.61×10^{13} Jones. Ying Lei's research team[183] designed NT40 and N2200, materials with high carrier mobility, and blended them into active layers of different thicknesses. The organic photodetector (OPD) with a 350 nm-thick active layer achieved the lowest J_d.

Specific morphological strategies including solvent additive utilisation, thermal annealing, and solvent vapour annealing have been demonstrated to effectively reduce trap states and suppress dark current by precisely controlling phase separation and molecular packing, whilst maintaining a narrow bandgap. Solvent additives influence the crystallisation process of polymers and acceptor molecules by altering solvent properties and evaporation rates, thereby regulating the degree of phase separation in the active layer. This leads to a reduction in trap formation and a consequent decrease in dark current. Köntges *et al.*[184] demonstrated that in the PBDB-T:ITIC blends, solvent additives such as 1,8-diiodooctane (DIO) or 1-chloronaphthalene (CN), synergising with thermal annealing, induce the formation of a chain-like polymorph in ITIC. This facilitates direct π–π contact with the polymer donor, enhancing carrier transport efficiency and reducing trap-assisted recombination. Bao *et al.*[185] employed dithieno[3,2-*b*:2′,3′-*d*]thiophene (DTT) and CN as additives to suppress excessive self-aggregation of Y6-type acceptors. Synergistic thermal annealing yielded a finely phase-separated structure, markedly reducing dark current. During thermal annealing, molecular motion and recrystallisation at elevated temperatures improve the crystalline quality of the active layer, enhancing charge carrier mobility.[186] Concurrently, thermal annealing eliminates defects and trap states within the active layer, thereby reducing dark current. Guo *et al.*[187] discovered that optimising thermal annealing temperature and duration induces a hierarchical nanoscale phase-separated structure between the donor (SM-mB) and mixed acceptor (Y6/L8-BO), promoting exciton dissociation and charge transport while reducing non-radiative recombination and trap-assisted recombination. Solvent vapour annealing (SVA) constitutes a mild post-processing technique. By permeating organic solvent vapour into the active layer, it induces recrystallisation of organic molecules and enhances molecular packing and orientation. This process facilitates the formation of more ordered molecular structures, thereby reducing trap density. Zeng *et al.*[146] induced directional rearrangement and π–π stacking of BTT-DTPn-2F molecules within the active layer *via* a chloroform (CF) solvent atmosphere, forming an ordered layered structure parallel to the substrate. This method also reduces voids and interfacial defects within the bulk heterojunction, lowering the density of states (DOS) by an order of magnitude. Wang *et al.*[188] discovered that for the D18:Y6 and D18:IT-4F systems, CF SVA promotes D18 chain extension, significantly enhancing the coherent length of D18–acceptor π–π stacking and thereby improving molecular packing quality.

4.2 Electrode

Electrodes with deep work functions can form Schottky barriers with the photoactive layer, thereby reducing charge injection. Common anodes include indium tin oxide (ITO), fluorine-doped tin oxide (FTO), carbon nanotubes (CNTs), and poly(3,4-ethylenedioxythiophene):polystyrene sulfonate (PEDOT:PSS), while cathodes are typically high-work-function metal electrodes such as Al and Ag. In recent years, applications like wearable devices and artificial retinas have imposed higher demands for electrode flexibility, transparency, and conductivity. ITO and FTO, with high optical transparency (∼90% in the visible range) and high conductivity, remain the most widely used transparent electrodes. However, these electrodes are brittle, costly, and exhibit low transmittance in the infrared region. To address these limitations, more flexible alternatives such as CNTs, silver nanowires (AgNWs), and PEDOT:PSS have gained increasing attention from researchers.[196–198] As shown in the Fig. 10(a), Lau *et al.*[189] fabricated a PEDOT:PSS upper electrode with 92% optical transparency at 850 nm using a lamination transfer process on an organic photoactive layer. The transparent self-powered NIR OPD based on the PEDOT:PSS upper electrode has an order of magnitude lower dark current and D^* exceeding 10^{12} Jones compared to the opaque MoO_3 electrode. As depicted in Fig. 10(b), Ma *et al.*[190] optimized a PEDOT:PSS thin film by sequential solution and film methanesulfonic acid (MSA) doping to obtain the SFD-PH1000 electrode. The SFD-PH1000 electrode has a high conductivity of 4400 S cm^{-2} and a high work function of 5.07 eV. The OPD using SFD-PH1000 as the anode exhibited a J_d one order of magnitude lower than ITO-based devices under −0.1 V bias, along with a broad and strong photoresponse across 300–1100 nm. Jang *et al.*[191] demonstrated that a flexible transparent CNT electrode with a low work function formed a significant electron injection barrier (approximately 1 eV) with the PBDTTT-EFT:$PC_{71}BM$ active layer(Fig. 10(c)). In contrast, the disparity in electron injection barrier between the PEDOT:PSS and the active layer is

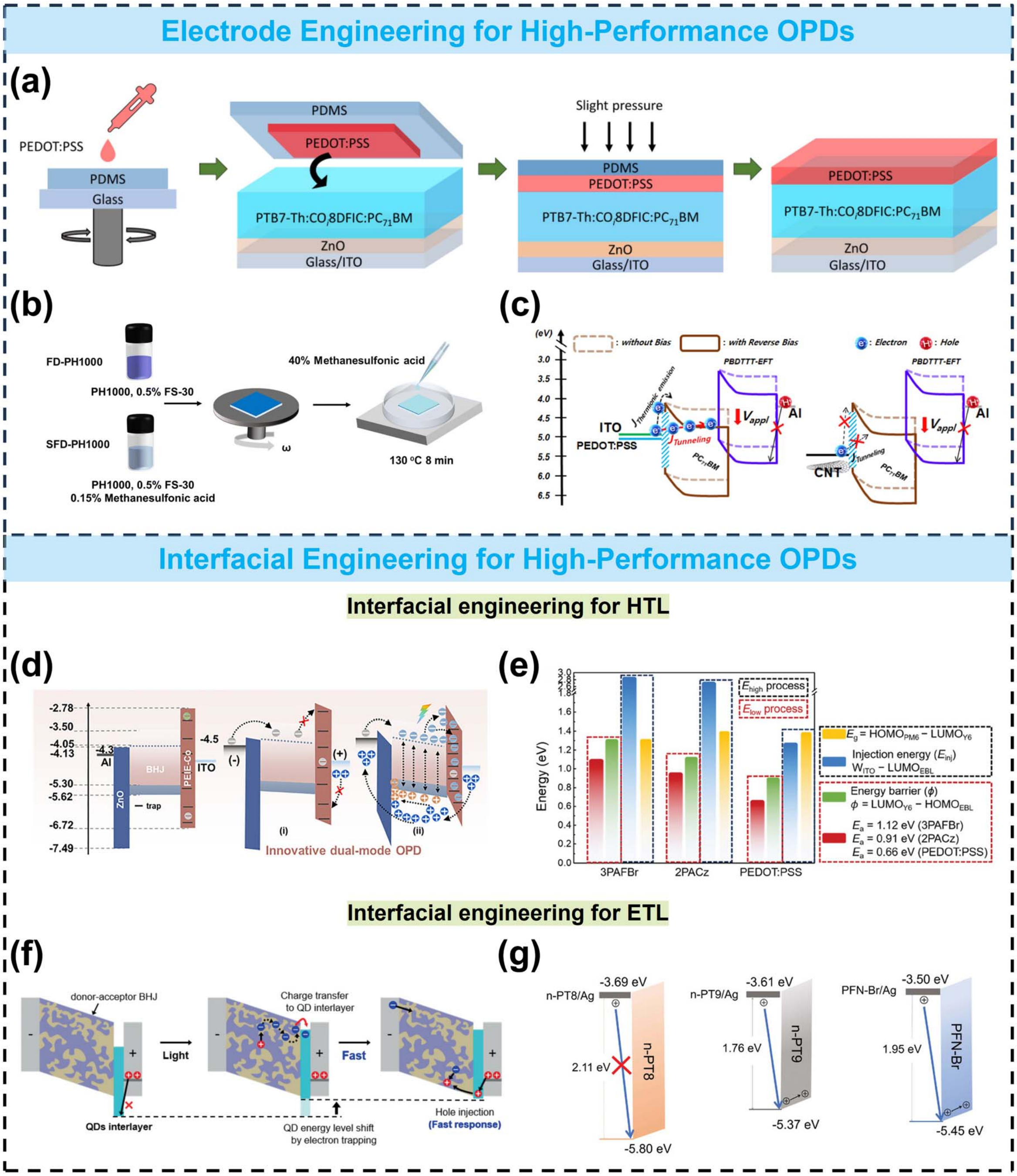

Fig. 10 Electrode and interfacial engineering to reduce dark current for high-performance OPDs. (a) A flow chart showing the deposition of a PEDOT:PSS upper transparent electrode on a photoactive layer using a lamination transfer process. Reproduced from ref. 189 with permission from Elsevier, copyright 2021. (b) Schematic preparation procedures of the FD-PH1000 and SFD-PH1000 electrode. Reproduced from ref. 190 with permission from Royal Society of Chemistry, copyright 2024. (c) Working principle of dark current generation in OPDs depending on the electrode. Reproduced from ref. 191 with permission from Elsevier, copyright 2021. (d) Diagram of the energy level arrangement, schematic diagram of working mechanism under forward bias of the dual-mode OPD. Reproduced from ref. 192 with permission from Wiley-VCH, copyright 2025. (e) Comparison of energy process variations within E_{high} (E_g and E_{inj}) and E_{low} (ϕ and E_a) for different EBL-based OPDs. Reproduced from ref. 193 with permission from Wiley-VCH, copyright 2024. (f) Schematics of working mechanisms of QD-interlayer PM-type OPD. Reproduced from ref. 194 with permission from Wiley-VCH, copyright 2021. (g) Schematic diagram of the hole injection barrier between n-PT8 and Ag electrode. Reproduced from ref. 195 with permission from Wiley-VCH, copyright 2024.

diminished due to the extent of bending of the energy levels. Consequently, the CNT-based OPD achieved an ultralow J_d of 9.62×10^{-13} A cm^{-2}, approximately 10^5 times lower than PEDOT:PSS-based OPD, and maintained a high D^* exceeding 10^{12} Jones from 300 to 900 nm. Ju *et al.*[199] reported a high-work-function transparent electrode composed of $Ti_3C_2T_x$ nanosheetconformally wrapped AgNWs. This electrode exhibited ultra-high transmittance (>94% at 400–800 nm) and low sheet resistance (<15 Ω sq^{-1}). Furthermore, introducing oxygen terminations on the $Ti_3C_2T_x$ surface generated positive dipoles, enabling tunable work functions ranging from 4.7 to 6.0 eV.

4.3 Interfacial layer

Excessive reverse bias voltage increases charge injection rates, leading to a rise in dark current density. To address this, a common approach is to enhance the charge injection barrier, such as introducing hole transport layers (HTLs) and electron transport layers (ETLs) at the interface between the active layer and electrodes, with energy levels aligned to those of the donor and acceptor materials in the active layer.[200] Furthermore, the interfacial layer has been demonstrated to enhance the photocurrent and stability by passivating the interfacial defects. Typical HTLs include PEDOT:PSS, molybdenum trioxide (MoO_3), CuSCN, and poly(*N*,*N*′-bis(4-butylphenyl)-*N*,*N*′-bis(phenyl) benzidine) (poly-TPD),[201] while ETLs include C_{60}, lithium fluoride (LiF), ZnO, and poly(9,9-bis(3′-(*N*,*N*-dimethylammonium) propyl)-2,7-fluorene)-*alt*-1,4-phenylene) bromide (PFN-Br). Xiao *et al.*[192] constructed dual-mode OPDs exhibiting photoconductive/photo-multiplication (PC/PM) effects under reverse/forward bias by modulating the energy levels and electron traps in the PEIE-Co interfacial layer. As shown in the Fig. 10(d), the deep HOMO and the shallow LUMO of PEIE-Co effectively increases the carrier injection barrier under reverse and forward bias, thereby suppressing the J_d of the device; Under illumination, the traps in PEIE-Co capture photo-generated electrons, causing the energy band to bend and lowering the injection barrier of external circuit holes, thereby achieving PM effect. Kim *et al.*[193] designed an electron-blocking layer (EBL), 3PAFBr, incorporating two phosphonic acid (PA) groups. Compared to 2PACz (which contains one PA group), the additional PA group in 3PAFBr anchors more effectively to electrode surfaces, thereby forming a uniform and defect-poor EBL layer. As shown in Fig. 10(e), the 3PAFBr-based OPD demonstrated the highest energy barrier ($\phi = \mathrm{LUMO_{Y6}}{-}\mathrm{HOMO_{EBL}}$) and electron injection barrier (E_{inj}). Moreover, the OPD incorporating 3PAFBr achieved an ultralow dark current density ($J_d = 12.3$ fA cm^{-2} at $V \rightarrow -0.1$ V). Zhou *et al.*[202] reported an all-polymer photodetector (Al/PDPP3T:$PC_{71}BM$/poly-TPD/ITO) with an ultralow J_d of 0.64 nA cm^{-2} under −0.5 V bias. This remarkably low J_d was attributed to the cross-linked poly-TPD layer, which served as a buffer to collect photogenerated holes while blocking electron injection from the ITO anode into the active layer under reverse bias. Nguyen's group[17] optimized the HTL by incorporating (3-glycidyloxypropyl)trimethoxysilane (GOPS) crosslinker into a conjugated polyelectrolyte (CPE), creating an insulating CPE-Ph interface. The shallower LUMO energy level of CPE-Ph, in conjunction with the increased GOPS content, can effectively impede electron injection. When CPE-Ph containing 0.5% GOPS (CPE-$Ph_{0.5}$) is utilized as the HTL, the J_d of the device can be as low as 1 nA cm^{-2} at −5 V bias. Han *et al.*[194] employed a monolayer of CdSe/ZnS core–shell quantum dots (QDs) as the electron transport layer (ETL) for a PM-type PBDB-T:Y6-based organic photodetector (OPD). In dark conditions, the QD layer effectively suppressed hole injection from the electrodes. Under illumination, it rapidly accumulated photogenerated electrons in the active layer, causing an upward shift of energy levels (Fig. 10(f)). This enabled a rapid response and low dark current. Liu's team[195] developed a n-type polythiophene derivative by introducing electron-withdrawing groups on polythiophene backbone, n-PT8, with E_{HOMO} as low as −5.80 eV. The n-PT8 molecule exhibited a substantial hole-injection barrier of 2.11 eV between itself and the cathode Ag, as illustrated in the Fig. 10(g). The NIR OPD based on n-PT8 demonstrated an ultra-low J_d of 1.76×10^{-9} A cm^{-2} (one order of magnitude lower than the J_d of the PFN-Br-based OPD) and a specific detectivity of 2.88×10^{12} Jones at −1 V.

5 Applications

5.1 Imaging

5.1.1 Artificial visual recognition systems. Conventional image data processing necessitates repetitive data conversion and transfer between memory and processor, resulting in high energy consumption and inefficiency when the amount of data is substantial, particularly in the domains of autonomous driving and artificial retina, which demand real-time processing of voluminous amounts of image information. Vertebrates, including humans, utilize a collaborative integration of the retina and the visual cortex of the multilayered brain to perceive their environment, while demonstrating the capacity to process substantial volumes of visual data with minimal energy expenditure and at elevated speeds. In conditions such as low lighting, precipitation, snow, and haze, infrared light detectors can provide clear images, offering critical information for path planning, speed control and obstacle avoidance of self-driving vehicles, which significantly improves driving safety.[206,207] Consequently, infrared photodetectors that emulate biological vision have emerged as a prominent research focus. Concurrent with the advancement of artificial retina or wearable vision systems, flexible OPDs have garnered significant interest from researchers worldwide due to their capacity to adapt to the nuances of human movement and the constraints of wearable environments.[208–210] Tang's research group[11] designed a flexible all-polymer OPD based on DPPT-TT:N2200. By developing a composite dielectric layer to enhance exciton dissociation efficiency, they achieved a specific detectivity of 1.13×10^{15} Jones. The OPD was integrated into a 90-pixel hemispherical biomimetic eye imaging system. Using an "H"-shaped mask under weak 808 nm near-infrared illumination to simulate 3D retinal imaging, Fig. 11(a) demonstrates the clear image captured by the biomimetic eye. Xia *et al.*[203] developed a narrow-bandgap acceptor YZ1 with a rigid electron-donating core (DTPC), constructing a PCE10:YZ1-based OPD with D^* of 9.24×10^{13} Jones at 1000 nm. To mimic biological eye imaging, they fabricated a 12 × 12-pixel flexible OPD array. As shown in Fig. 11(b), when 940 nm light passed through an "H"-shaped mask and projected onto the OPD array, the system successfully resolved the letter "H" with high clarity. Enhancing the long-term operational stability and robustness of NIR–SWIR OPDs

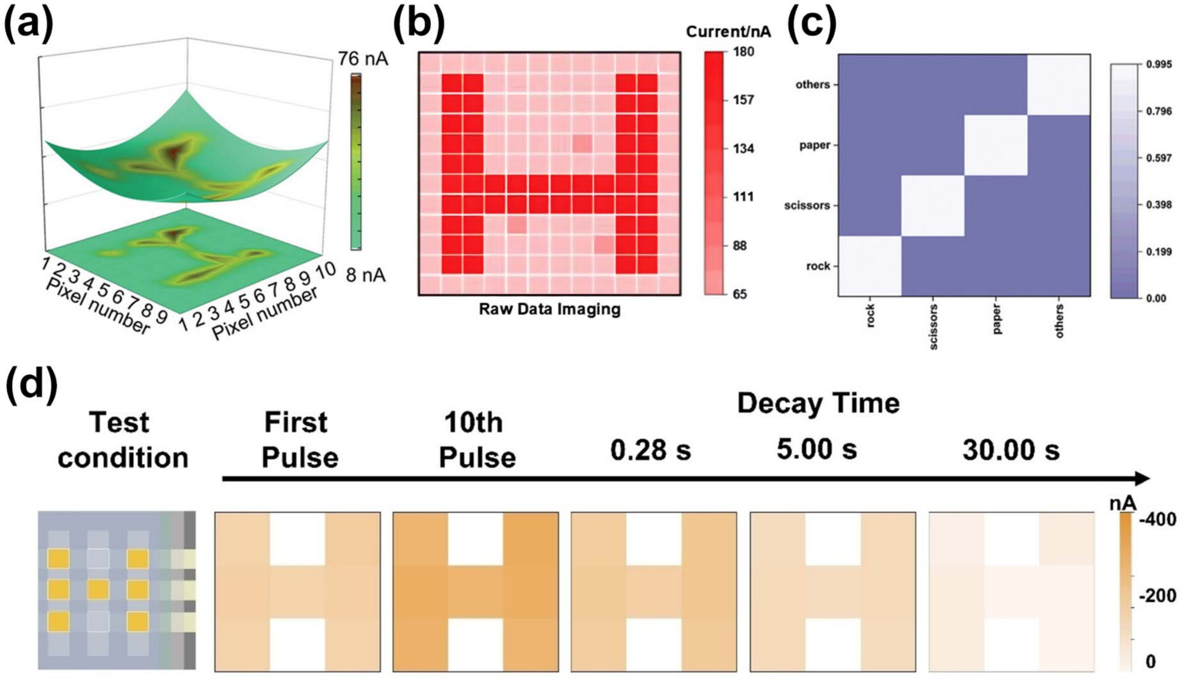

Fig. 11 (a) Imaging of an ultraflexible DPPT-TT:N2200-based OPD array under 808 nm illumination. Reproduced from ref. 11 with permission from Wiley-VCH, copyright 2022. (b) Imaging of a PCE10:YZ1-based flexible OPD array under 940 nm illumination. Reproduced from ref. 203 with permission from Wiley-VCH, copyright 2024. (c) Recognition accuracy of a PbS/C_{60}/pentacene organic ambipolar transistor array for different hand gestures. Reproduced from ref. 204 with permission from Wiley-VCH, copyright 2025. (d) EPSC signals read from a P1:$PC_{71}BM$-based phototransistor array after the 1st pulse, 10th pulse, and at 0.28 s, 5.00 s, 30.00 s following light cessation, with SWIR light patterned as the letter "H". Reproduced from ref. 205 with permission from Wiley-VCH, copyright 2023.

under practical mechanical strain requires coordinated efforts in both material structural design and device architecture innovation. The instability of OPDs primarily stems from the susceptibility of the photoactive layer to moisture and oxygen, as well as the hygroscopicity and intrinsic instability of anode or cathode interlayers. Effective strategies to significantly reduce environmental sensitivity include introducing high-stability molecular frameworks such as all-fused-ring or semi-fused-ring structures,[211] developing electrode interlayers that efficiently block environmental moisture,[50] and employing flexible substrates with high mechanical flexibility and strong interfacial adhesion.[178] Zhang *et al.*[211] reported an all-fused-ring small-molecule acceptor, FM2, which effectively mitigates photoisomerization and photo-oxidation of the material under illumination. This approach was further combined with a hydrophobic cross-linked polymer cathode interlayer (c-NDI), substantially improving the OPD stability under high-humidity conditions. Xu *et al.*[13] utilized a hydrophobic and well-phase-separated PTB7-Th:BTP-4F:COTIC-4F ternary blend as the photoactive layer, together with a mechanically robust polyethylene naphthalate (PEN) flexible substrate, successfully realizing an unencapsulated OPD that withstands 1000 hours of water immersion and 10 000 bending cycles. In another study, Wijaya *et al.*[214] introduced a novel electron transport layer with low defects, good adhesion, and hydrophobicity, and adopted highly flexible parylene as the substrate to construct a flexible OPD. Owing to excellent interfacial stability and interlayer adhesion, the device maintained stable detection performance after 5000 surface bending cycles.

Artificial visual recognition systems are promising candidates for mimicking biological vision's capabilities in sensing, processing, and memorizing visual information. These systems can simulate synaptic behaviors such as paired-pulse facilitation (PPF), short-term plasticity (STP), long-term plasticity (LTP), STP-LTP transitions, excitatory postsynaptic currents (EPSC), and inhibitory postsynaptic currents (IPSC).[215] Active layer materials exhibit synaptic memory effects by inducing delayed photocurrent decay during charge trapping, enabling their application in optical neuromorphic artificial vision systems. Currently, most reported systems adopt phototransistor architectures, as their gate voltage tunability facilitates delayed photocurrent decay and enhanced synaptic performance.[215–218] Liu *et al.*[219] constructed a synaptic phototransistor using a PDPP-DTT:C6Si/PbS CQDs photoactive layer, which demonstrated a high responsivity of 6.02×10^2 A W^{-1} at 1064 nm. Leveraging its slow photocurrent decay characteristics, the device achieved "short-term memory" functionality: after "forgetting" previously "learned" information from 50 light pulses at 1100 nm, it required only 30 pulses to regain the same learning level. Huang's research group designed a novel narrow-bandgap (0.69 eV) conjugated polymer (P1).

P1:$PC_{71}BM$-based phototransistor simulated PPF, EPSC, STP, and LTP behaviors under ultralow power consumption (2.85 fJ).[205] As shown in Fig. 11(d), a 3 × 3 phototransistor array

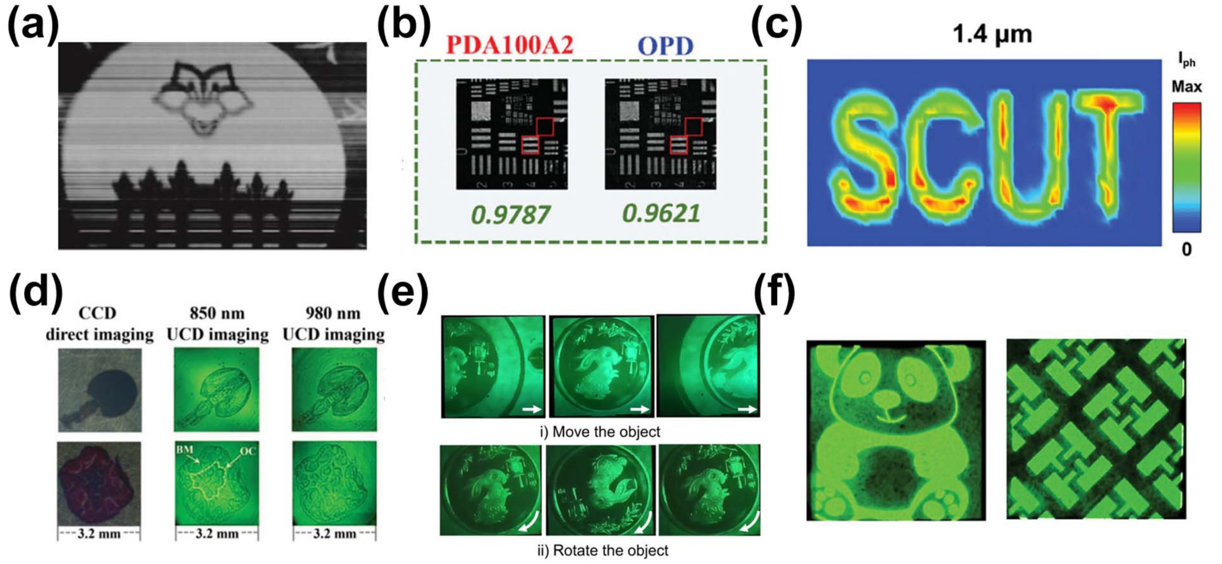

Fig. 12 (a) High-pixel density imaging of an OPD array based on PTB7-Th:COTIC-4F:Y6. Reproduced from ref. 121 with permission from Wiley-VCH, copyright 2022. (b) High-resolution imaging based on an OPD of PBDB-T:PZF-V:PY-IT and a commercial silicon diode PDA100A2. Reproduced from ref. 126 with permission from Wiley-VCH, copyright 2024. (c) Single-pixel imaging results of an OPD based on PTB7-Th:Y-QC4F under the illumination of a SWIR light source ($\lambda = 1.4$ μm). Reproduced from ref. 28 with permission from Wiley-VCH, copyright 2024. (d) Bioimaging of PTB7-Th:IEICO-4F:$PC_{71}BM$-based UCDs under 850 and 980 nm illumination. Reproduced from ref. 212 with permission from Wiley-VCH, copyright 2021. (e) Dynamic up-conversion imaging of PTB7-Th:ATT-X-F_{in}-based OUDs under 1064 nm illumination. Reproduced from ref. 3 with permission from AAAS, copyright 2024. (f) PTB7-Th:COTIC-4F:BTP-eC9-based UCD observed using a mask under 980 nm illumination. Reproduced from ref. 213 with permission from Wiley-VCH, copyright 2025.

gradually resolved the letter "H" under 1550 nm SWIR illumination as pulse frequency increased. It retained the memory of the pattern for 30 seconds post-illumination, which demonstrates perception-memory integration critical for neuromorphic computing. Xie *et al.*[204] mimicked the fruit fly visual system by fabricating a 20 × 20 PbS/C_{60}/pentacene organic ambipolar transistor array with bidirectional photoresponse across visible and NIR wavelengths. Using dual OFET arrays to decompose optical signals into EPSC and IPSC components, they trained a motion detection system integrated with a convolutional neural network (CNN). As illustrated in Fig. 11(c), the OPD array achieved 98.1% accuracy in gesture recognition.

5.1.2 Optical imaging. Optical imaging has broad applications in medical imaging, military reconnaissance, and industrial non-destructive testing. Organic infrared photodetectors enable optical imaging by converting light signals into electrical signals, which are then processed by computers to generate digital images. Huang *et al.*[121] fabricated an organic photodiode with PTB7-Th:COTIC-4F:Y6 as the infrared-active layer, achieving a specific detectivity exceeding 10^{13} Jones across a broad spectrum of 780–1070 nm. They further constructed a 1 × 256 linear organic photodiode image array (OPDIA) with a pixel pitch of 25 μm × 25 μm. As shown in Fig. 12(a), the OPDIA integrated with a readout integrated circuit (ROIC) successfully achieved high-pixel-density imaging of the emblem of South China University of Technology. The same group[220] also developed a photoconductor based on PBTT:PBTB, which exhibited outstanding detection performance at 1122 nm (responsivity up to 0.96 A W^{-1}). They fabricated a 16 × 16 flexible OPD image sensor capable of clearly resolving the spatial intensity distribution of 1342 nm infrared light. Chandran *et al.*[126] reported a fully polymer-based ternary photodiode using PBDB-T:PZF-V:PY-IT and fabricated it into a single-pixel detector. Fig. 12(b) demonstrates that the detector exhibits a contrast-to-noise ratio (CNR) comparable to commercial silicon diodes (PDA100A2) in scattering environments, enabling high-resolution computational imaging. Liu's team[28] designed and synthesized a novel non-fullerene acceptor, Y-QC4F, with an ultralow bandgap of 0.83 eV. As demonstrated in Fig. 12(c), PTB7-Th:Y-QC4F-based OPD showcased high-quality short-wave infrared (SWIR) imaging capabilities under 1.4 μm NIR illumination using a "SCUT"-patterned mask.

Up-conversion imaging devices eliminate the need for complex epitaxial readout integrated circuits, offering simple structures and relatively low manufacturing costs. Du *et al.*[212] fabricated an organic upconversion device (UCD) using PTB7-Th:IEICO-4F:$PC_{71}BM$ (80 nm) as the infrared absorption layer and CBP:Ir$(ppy)_2$ as the visible light emission layer. This UCD successfully converted 1064 nm infrared light into 524 nm visible light with an upconversion efficiency of 12.9%. As shown in Fig. 12(d), the device clearly resolved fine anatomical features such as the mouthparts of houseflies and the membranous cuticle of locusts. Zhu's research group[3] synthesized a small-molecule material, ATT-X-F_{in}, with a spectral response spanning 300–1300 nm. They integrated a PTB7-Th:ATT-X-F_{in}-based SWIR photodetector with a phosphorescent organic light-emitting diode (OLED) to create an all-organic upconversion device (OUD) achieving 8% upconversion efficiency. As

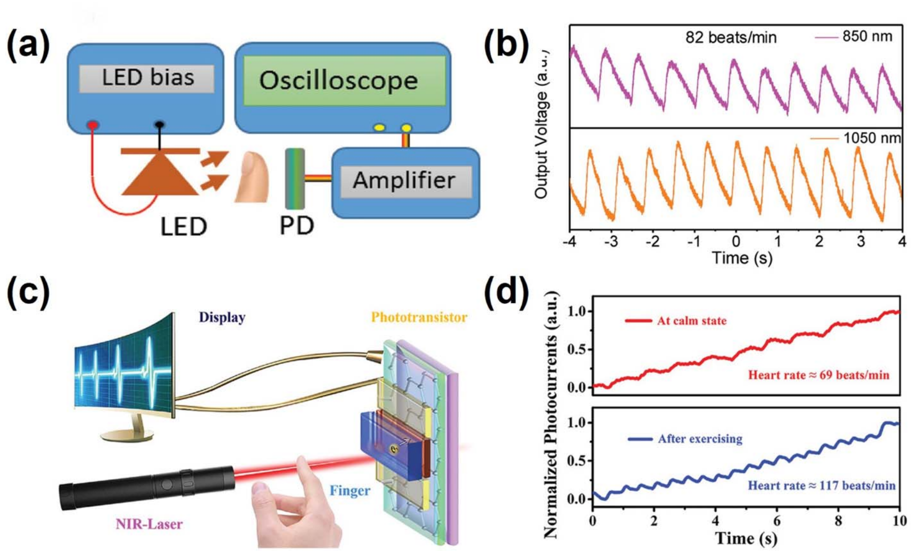

Fig. 13 (a) PPG measurement setup, (b) heartbeat waveforms measured under 850 nm and 1050 nm illumination of DPP-DTT:SWIR dye-based OPD PPG sensor. Reproduced from ref. 80 with permission from Wiley-VCH, copyright 2020. (c) NIR contactless real-time pulse monitoring setup, (d) heart rate of a subject at rest and post-exercise of PTB7-Th:IEICO-4F:$PC_{71}BM$-based OPD PPG sensor. Reproduced from ref. 81 with permission from Wiley-VCH, copyright 2021.

illustrated in Fig. 12(e), the OUD demonstrated dynamic SWIR upconversion imaging of moving or rotating objects, highlighting its potential for night vision applications. Dong *et al.*[213] combined a NIR OPD based on PTB7-Th:COTIC-4F:BTP-eC9 with a phosphorescent OLED for upconversion imaging, efficiently converting 980 nm NIR light into visible green light with an upconversion efficiency of 16.68%. This UCD captured NIR signals modulated by patterned masks and converted them into high-resolution green patterns. Fig. 12(f) shows a high-resolution green pattern taken with a camera.

5.2 Healthcare monitoring

Photoplethysmography (PPG) is a non-invasive medical sensing technique that utilizes photodetectors to measure changes in infrared light absorption/reflection by blood vessels in living tissues, enabling real-time monitoring of heart rate, cardiac cycle, blood oxygen saturation, blood pressure, and other parameters, thereby providing information about cardiovascular and respiratory systems.[221] As shown in Fig. 13(a and b), Li *et al.*[80] developed a large-area, room-temperature organic photodetector based on a DPP-DTT:SWIR dye BHJ layer, sensitive to light in the 1000–1600 nm wavelength range. These detectors were integrated into PPG sensors for pulse oximeters and demonstrated exceptional performance in real-time heart rate monitoring. He *et al.* reported a graphene/ZnO/PTB7-Th:IEICO-4F:$PC_{71}BM$ phototransistor with strong near-infrared absorption across 760–1100 nm, achieving a high responsivity of 6×10^6 A W^{-1} and a specific detectivity exceeding 2.4×10^{13} Jones at 850 nm.[81] As illustrated in Fig. 13(c and d), he successfully applied this device to a signal amplification-free, contactless heart rate monitor. Zhang *et al.*[27] developed an n-type fully fused ring molecule, FM2, which exhibits a narrow optical band gap of 1.22 eV and strong near-infrared absorption. A self-powered OPD device based on PBDB-T:FM2 was used to construct a simple PPG sensor. The sensor can detect the cardiac cycle using an 808 nm laser and successfully detect a human heart rate of 72 beats min^{-1}. Wang *et al.*[222] selected highly transparent indium tin oxide (ITO) and thin silver (Ag) layers as electrodes to construct a flexible translucent NIR OPD based on BDP-OMe:C_{60}. This OPD translates the different absorption properties of oxygenated and deoxygenated haemoglobin under 730 nm illumination into detected systolic peaks and troughs, which in turn calculates oxygen saturation levels and pulse values.

5.3 Optical communication

Infrared (IR) optical communication is a wireless technology that transmits data *via* IR light, eliminating the need for cables and significantly reducing costs for short-range communication. The operational principle of IR OPDs in communication involves converting input text into ASCII codes *via* a computer. A serial communication module modulates an LED to emit corresponding IR signals based on the ASCII codes. The OPD receives these signals and outputs electrical currents, which are then converted back to ASCII codes by the serial module, ultimately displaying the text on a screen.[90] Compared to the intrinsic rigidity and brittleness of inorganic photodetectors based on materials like Si and GaAs, IR OPDs leverage flexible organic materials, making them ideally suited for applications such as skin-mounted health monitoring devices, foldable displays, and flexible automotive systems.[118] Furthermore, their compatibility with solution-processable fabrication techniques (including spin-coating, blade-coating, and roll-to-roll printing), enables large-area manufacturing at a fraction of the cost, with a per-pixel expense estimated to be merely 5% of that of silicon-based photodetectors.[128] Additionally, while

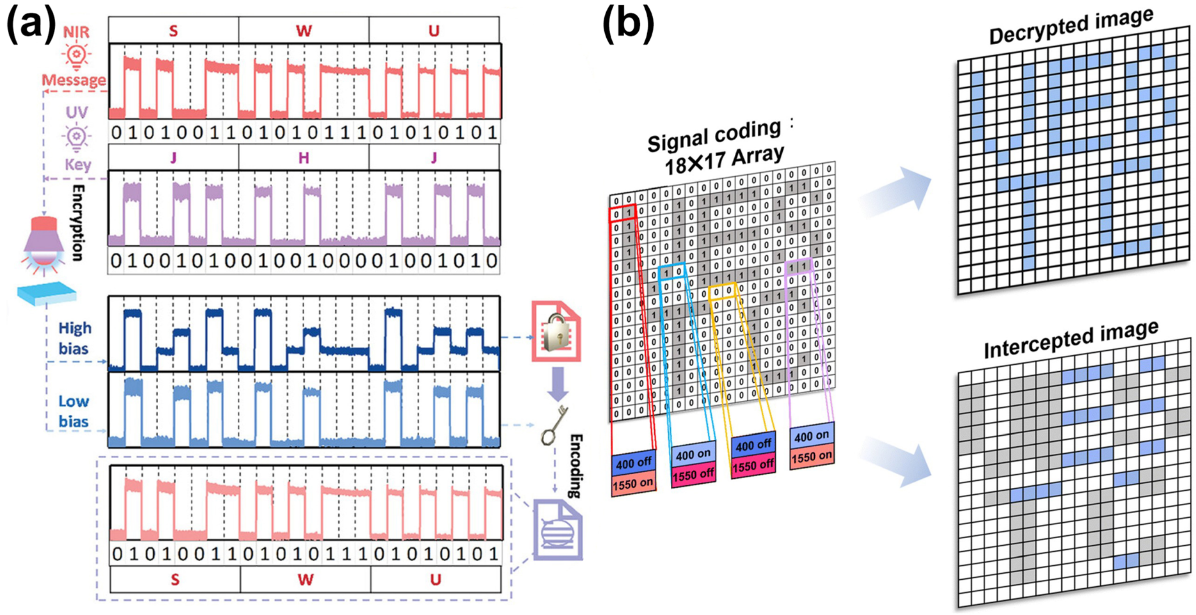

Fig. 14 (a) Flowchart of PolyTPD:Y6-based bipolar OPD encrypting and decrypting at high and low bias conditions. Reproduced from ref. 223 with permission from Wiley-VCH, copyright 2025. (b) Demonstration of dual-channel encrypted optical communication using HgTe QDs/PBDB-T:Y6 bipolar OPD. Reproduced from ref. 224 with permission from Wiley-VCH, copyright 2025.

inorganic detectors often require external optical filters for spectral selection (*e.g.*, a Si photodiode coupled with an 850 nm bandpass filter), which increases system complexity and cost, IR OPDs can achieve filter-free, multi-spectral response and even encryption functions through tailored material design or bias-voltage tuning.[223] Maxime *et al.*[225] developed a narrow-bandgap SMA, O4TFIC, absorbing light up to 1020 nm by incorporating carbon-oxygen bridges, linear side chains, and fluorinated terminal units. The PM6:O4TFIC-based OPD exhibited ultrafast IR response (t_r and t_d both <4 μs), enabling accurate transcription of ∼910 nm signals emitted from commercial remote controls. With accelerating digitalization, information security demands higher confidentiality and integrity in optical communication. Jiang *et al.*[223] developed a switchable dual-mode OPD by optimizing the blend of Poly-TPD and Y6. This device responded solely to ultraviolet (UV) light under low bias but became sensitive to both UV and NIR light at high voltage, achieving encrypted optical communication. As shown in Fig. 14(a), the OPD generated mixed signals under high bias, while extracting the "JHJ" decryption key from UV-only responses under low bias. Through positional mapping and signal subtraction, chaotic data were decrypted to reveal the target message "SWU". Zeng *et al.*[224] reported a self-powered photodetector based on stacked HgTe quantum dots and PBDB-T:Y6. The device showed positive responsivity across 300–1000 nm and negative responsivity from 1000–1800 nm (at 0 V bias). As illustrated in Fig. 14(b), conventional unipolar photodetectors failed to distinguish wavelength-specific signals, leading to partial pixel loss, while the bipolar detector accurately reconstructed the "UESTC" image, enabling secure dual-channel encrypted optical communication.

6 Challenges and opportunities

In recent years, the active layer materials and device fabrication processes for NIR–SWIR OPDs have been greatly developed and optimized. In terms of active material development, the HOMO and LOMO energy levels of the donor receptor are fine-tuned through molecular core modification and side-chain engineering to achieve a narrow band gap, which in turn widens the spectral response range; in terms of device structure design, the active layer morphology is optimized, the electrodes with suitable figure of merit are selected, and the interfacial engineering of the electrodes and the active layer is optimized, which reduces the dark current density and in turn improves the specific detection rate and response. Currently, the spectral response range of NIR–SWIR OPDs based on low bandgap polymers has been successfully extended to 1500 nm, with a specific detectivity of 10^{13} orders of magnitude (Jones) and a dark current density reduced to 10^{-10} orders of magnitude (A cm^{-2}), which is comparable to that of silicon-based inorganic detectors. In addition, NIR–SWIR OPDs have been successfully applied to artificial vision systems, imaging, PPG sensors and optical communications, and have demonstrated a wide range of application potentials in a variety of fields, such as wearable electronics, health monitoring, military surveys, and automated driving, *etc.* Despite the great progress in the development of NIR–SWIR OPDs, they still face some formidable challenges before commercial application. The difficulties mainly focus on two aspects: low detection performance and insufficient functional integration. Solving these problems will open up new opportunities for the widespread application of OPDs. This section highlights the main problems and potential solutions for OPDs, and the Fig. 15 summarizes the key points.

(i) Performance enhancement: first, the detection performance of most NIR–SWIR OPDs is still somewhat inadequate compared to inorganic detectors. Few organic materials have detection wavelengths above 1 μm, and the design and synthesis of low bandgap (<1 eV) organic materials is still quite challenging. Currently, the design of organic materials mainly relies on traditional molecular body engineering (*e.g.*, modulation of D–A or quinone structures) and side-chain engineering (*e.g.*, substituent resizing). However, this approach is characterized by long design cycles and complex synthesis. High-throughput screening strategies combined with big data computing can enable efficient design of small bandgap molecules. For example, DFT, molecular dynamics simulations, *etc.* can predict the distribution of HOMO and LUMO orbitals of molecules. However, limited by the non-radiative leaps induced by the energy gap law, the smaller the molecular bandgap, the more susceptible it is to high dark currents caused by lattice heating, as well as to reduced detection sensitivity for low-energy photons. Several studies have been carried out to extend the detection range of detectors by introducing quantum dots or quantum wells and designing optical resonant microcavities.[18,226,227] Recently, multi-effect synergistic strategies have gradually become a hot research topic to extend the spectral absorption range.[228,229] Coupling polarization effects such as piezoelectric, pyroelectric, and ferroelectric effects can break the bottleneck that organic detectors are almost unresponsive in the mid- and long-wave infrared wavelengths. For instance, Liu *et al.*[230] demonstrated a device with a high photovoltage of up to 1386 mV at 915 nm by com-bining P(VDF-TrFE) with a photothermal Schiff base compound. This performance is attributed to a synergistic effect where the compound's photothermal conversion induces a temperature gradient sensed by the polymer's pyroelectric effect, paving the way for fast, broadband infrared detection. In another approach, Wang *et al.*[231] achieved NIR detection (0.85–1.55 μm) using a composite of P(VDF-TrFE) and MoS_2. However, the response time of conventional thermal detectors is limited by the phonon-dominated lattice thermal transport (typically on the order of milliseconds), and thus the simultaneous realization of fast optical response and broad spectral detection under multi-effect synergy has become the focus of research on such detectors.[232] It has been found that low-dimensional materials (*e.g.*, graphene) can improve the response speed to the picosecond level by hot carrier-assisted transport.[233,234] Second, there is still no general and effective solution to the problems associated with the high dark current density, low D^* and low

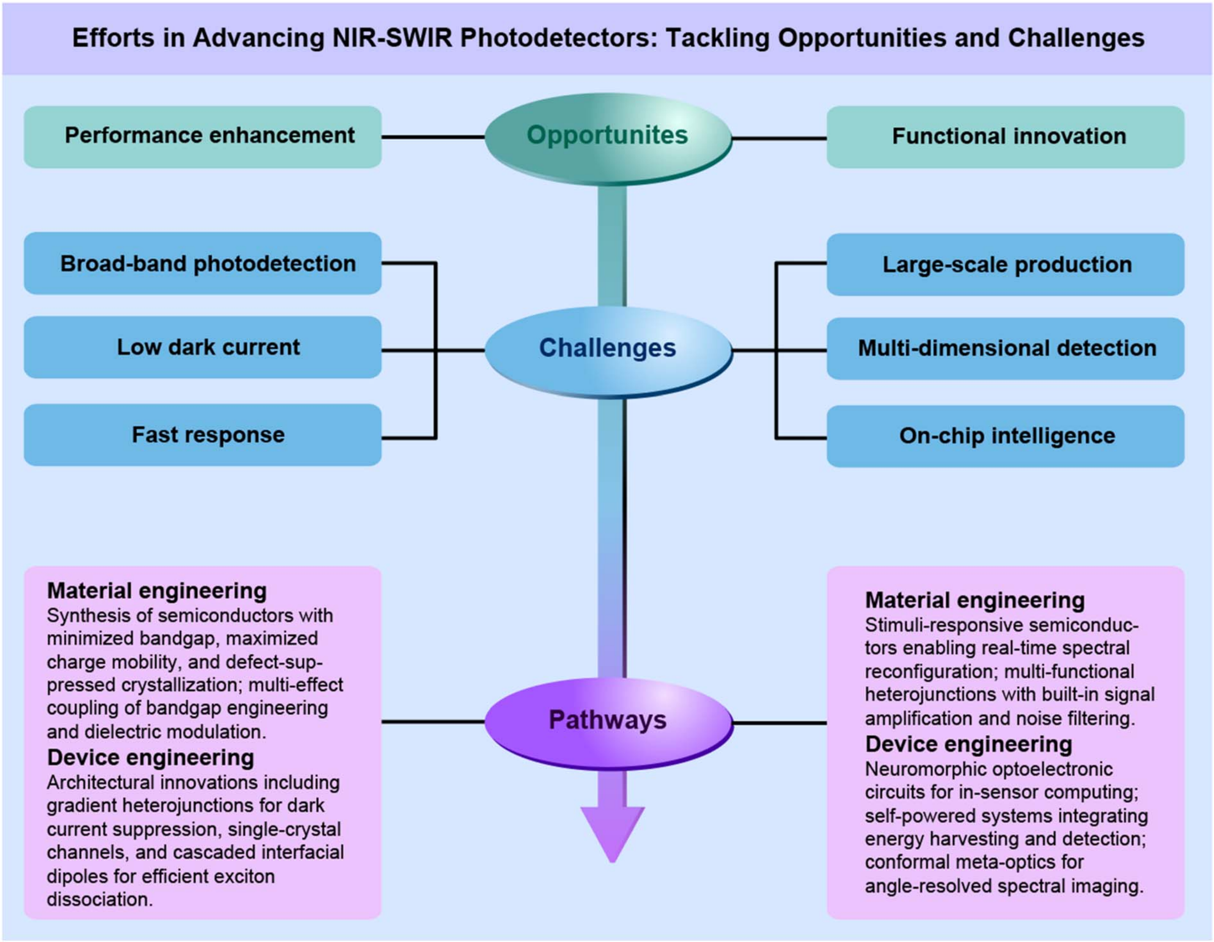

Material engineering
Synthesis of semiconductors with minimized bandgap, maximized charge mobility, and defect-suppressed crystallization; multi-effect coupling of bandgap engineering and dielectric modulation.
Device engineering
Architectural innovations including gradient heterojunctions for dark current suppression, single-crystal channels, and cascaded interfacial dipoles for efficient exciton dissociation.

Material engineering
Stimuli-responsive semiconductors enabling real-time spectral reconfiguration; multi-functional heterojunctions with built-in signal amplification and noise filtering.
Device engineering
Neuromorphic optoelectronic circuits for in-sensor computing; self-powered systems integrating energy harvesting and detection; conformal meta-optics for angle-resolved spectral imaging.

Fig. 15 Opportunities, challenges and pathways for future NIR–SWIR OPDs.

EQE of NIR–SWIR OPDs. The understanding of the complex electron and phonon transport mechanisms of bulk heterojunctions and the dark current generation mechanisms on the effect of light detection is still limited. Jonas *et al.*[235] found that the trap states caused by the disordered nature, structural defects and impurities of the organic materials and devices are the main sources of dark currents. Crystal engineering of organic materials into long-range ordered single crystals or eutectics with few defects could be a good option to reduce the dark current density. In addition, dark current can be reduced by optimizing molecular stacking (*e.g.*, inducing J-aggregation) and designing novel active layer structures such as gradient heterojunctions. Finally, the optical response speed of NIR–SWIR OPDs is limited, typically on the order of microseconds (μs), making it difficult to meet the demands of real-time applications such as optical communications, autonomous driving, and artificial vision systems. The molecules are modulated to be in π–π stacking mode to reduce structural defects such as grain boundaries, vacancies, and dislocations in semiconductors, and interfacial defects between different materials of the device. These strategies can effectively enhance the carrier mobility and thus accelerate the optical response.

(ii) Functional innovation: functional integration of NIR-SWIR OPDs serves as a critical foundation for their deployment in practical applications—such as military surveillance, autonomous driving, and wearable healthcare systems, while three fundamental challenges impede the progress. Firstly, although the integration of OPD with complementary technologies such as quantum dots and 2D materials has opened up new avenues for high-performance infrared detection, the move from laboratory single-component devices to large-scale, high-resolution imaging arrays still faces severe system-level bottlenecks. One of the most pressing challenges stems from the homogeneity of large-scale arrays and the compatibility of multi-material heterogeneous integration processes. The homogeneity of device performance is critical in large-area arrays, and any inhomogeneity will generate fixed pattern noise (FPN) in the final image, severely degrading the imaging quality. Organic semiconductor films prepared using solution methods suffer from crystallinity and thickness fluctuations due to the coffee-ring effect,[236,237] and 2D materials and quantum dot films[238,239] have uneven response due to uneven thickness and insufficient ligand stability, respectively, which can significantly degrade the imaging resolution and signal-to-noise ratio. To address these issues, the solution shearing method, when combined with templates or auxiliary tools, can produce large-area, centimeter-scale organic single-crystal arrays with controllable thickness.[240,241] On the other hand, the heterogeneous integration of OPDs, quantum dots and 2D materials with silicon-based readout circuits (ROICs) faces problems such as high contact resistance and process temperature mismatch. Meanwhile, the reduced pixel pitch at high resolution further aggravates the carrier interferences between neighbouring pixels, resulting in reduced dynamic response.[242] The development of non-destructive integration processes such as low-temperature transfer and van der Waals integration provides an important solution to improve pixel coherence and response performance.[243,244] Currently, the main methods to solve the electrical crosstalk problem include precise patterning of the functional layer to limit the lateral diffusion of carriers, such as the use of directional growth and patterning techniques of organic semiconductor single crystal arrays on customised templates, which reduces leakage currents and fringe current disturbances between neighbouring devices;[245] and patterning the hole transport layer by photolithography and reactive ion etching techniques, which significantly reduce inter-pixel parasitic currents.[246] In addition, the long-term stability of devices and packaging technology are also major challenges for practical applications. Organic semiconductors, quantum dots, and 2D materials are environmentally sensitive and prone to oxidation or degradation.[247] Therefore, the development of high barrier optical packaging structures as well as organic semiconductor molecules that are resistant to hydroxylation is essential for achieving reliable long-wave infrared imaging systems. In summary, future research needs to be dedicated to heterogeneous integration process optimisation, array uniformity control and high-performance packaging technologies to drive organic hybrid infrared photodetectors towards large-scale commercial imaging applications. Additionally, the transmission time of light can be used to obtain optical range information, which can then be applied to autonomous driving ranging. However, there is a paucity of literature addressing multidimensional infrared detection by OPDs. In the future, acquiring multidimensional information while developing novel applications may become one of the mainstream development directions of organic infrared light detection. Finally, smart-on-chip applications such as machine vision, artificial retina, and wearable devices, among others, impose heightened demands on OPDs with regard to flexibility, transparency, miniaturization, and low power consumption. Consequently, emerging research directions include the development of flexible, highly transparent, and highly conductive electrodes, as well as the construction of self-powered detectors. To further advance on-chip intelligent applications, it is imperative to enhance the integration density of organic semiconductors, develop large-area flexible detector arrays, and leverage the memory characteristics of transistors integrated with deep learning or neural network architectures. Xie *et al.*[204] constructed a 20 × 20 PbS/C_{60}/pentacene organic bipolar transistor array, which combined with a convolutional neural network (CNN) to improve the accuracy of motion target recognition of the OPD array by more than 10%.

In conclusion, further investigation of high-performance NIR–SWIR OPDs is necessary. These photodetectors are expected to become a new generation of mainstream photodetectors due to their rapid development, low cost, and bright application prospects.

Author contributions

Hongyu Tan and Xianshuo Wu contributed equally to this work. All the authors contributed to the discussion and manuscript preparation.

Conflicts of interest

The authors declare no competing financial interest.

Data availability

No primary research results, software, or code have been included, and no new data were generated or analyzed as part of this review.

Acknowledgements

This work was supported by the National Key Research and Development Program of China (Grant No. 2024YFB3614500), the National Natural Science Foundation (Grant No. 52373194, 52403301, and U24A20293), the Scientific Research Initial Funding of Civil Aviation University of China (Project No. 2020KYQD95), and the Haihe Laboratory of Sustainable Chemical Transformations.

References

1 F. P. García de Arquer, A. Armin, P. Meredith and E. H. Sargent, Solution-processed semiconductors for next-generation photodetectors, *Nat. Rev. Mater.*, 2017, **2**, 16100.
2 H. Hou, W. Wang, T. Li, Z. Zhang, X. Miao, G. Cai, X. Lu, Y. Yi and Y. Lin, Efficient infrared-detecting organic semiconductors featuring a tetraheterocyclic core with reduced ionization potential, *Angew. Chem., Int. Ed.*, 2025, **64**, e202425420.
3 Y. Chen, Y. Zheng, J. Wang, X. Zhao, G. Liu, Y. Lin, Y. Yang, L. Wang, Z. Tang, Y. Wang, Y. Fang, W. Zhang and X. Zhu, Ultranarrow-bandgap small-molecule acceptor enables sensitive SWIR detection and dynamic upconversion imaging, *Sci. Adv.*, 2024, **10**, eadm9631.
4 W. E. Meador, M. A. Saucier, M. R. Tucker, N. A. Kruse, A. J. Mobley, C. R. Brower, S. R. Parkin, K. M. Clark, N. I. Hammer, G. S. Tschumper and J. H. Delcamp, Extended shortwave infrared absorbing antiaromatic fluorenium-indolizine chromophores, *Chem. Sci.*, 2024, **15**, 12349–12360.
5 I. Burgués-Ceballos, L. Lucera, P. Tiwana, K. Ocytko, L. W. Tan, S. Kowalski, J. Snow, A. Pron, H. Bürckstümmer, N. Blouin and G. Morse, Transparent organic photovoltaics: A strategic niche to advance commercialization, *Joule*, 2021, **5**, 2261–2272.
6 X. Chen, R. Huang, Y. Han, W. Zha, J. Fang, J. Lin, Q. Luo, Z. Chen and C. Ma, Balancing the molecular aggregation and vertical phase Separation in the Polymer: Nonfullerene blend films enables 13.09% efficiency of organic solar cells with inkjet-printed active layer, *Adv. Energy Mater.*, 2022, **12**, 2200044.
7 F. Cao, L. Liu and L. Li, Short-wave infrared photodetector, *Mater. Today*, 2023, **62**, 327–349.
8 J. V. Dcosta, D. Ochoa and S. Sanaur, Recent progress in flexible and wearable all organic photoplethysmography sensors for SpO2 monitoring, *Adv. Sci.*, 2023, **10**, 2302752.
9 Y. Xia, J. Zhang, T. Guo, H. Wang, C. Geng, Y. Zhu, R. Han, Y. Yang, G. Song, X. Wan, G. Li and Y. Chen, High-speed flexible near-infrared organic photodetectors for self-powered optical integrated sensing and communications, *Adv. Funct. Mater.*, 2025, **35**, 2412813.
10 C. Xu, M. Li, N. Sui, K. Kang, S. Shao, M. Deng, Q. Zhang, L. Jiao, C. Qiu and J. Zhao, Ultralow-power highly-selective near-infrared (≈850 nm) carbon nanotube flexible optoelectronic synaptic transistors for real-time trajectory tracking, *Small*, 2025, **21**, 2412324.
11 H. Yu, X. Zhao, M. Tan, B. Wang, M. Zhang, X. Wang, S. Guo, Y. Tong, Q. Tang and Y. Liu, Ultraflexible and ultrasensitive near-infrared organic phototransistors for hemispherical biomimetic eyes, *Adv. Funct. Mater.*, 2022, **32**, 2206765.
12 H. Jiang, Y. Hu, X. Gao, T. Wei, N. Li, Q. Zhang, W. Jia, L. Chen, X. Guo and Y. Lei, Crosstalk-free dual-band detection of visible and near-infrared light enabled by the combination of optical design and one-step transfer printing, *Adv. Funct. Mater.*, 2025, 2500628.
13 Z. Xu, Y. Li, Z. Ye, X. Liang, K. Qian, H. Huang, K. Ke, C. Shu, L. Song, H. Fu, J. Li, F. Kang and G. Wei, Flexible and stable ternary organic photodetector for broadband visible–NIR applications in high-fidelity imaging and optical communication, *Small Methods*, 2025, 2500296.
14 M. Liu, W. Li, Z. Peng, X. Shao, J. Liu and L. Wang, Electron acceptors based on resonant N—B ← N unit with improved exciton dissociation for high-performance short-wavelength infrared organic photodetectors, *Angew. Chem., Int. Ed.*, 2025, e202506116.
15 C. Wang, X. Ren, C. Xu, B. Fu, R. Wang, X. Zhang, R. Li, H. Li, H. Dong, Y. Zhen, S. Lei, L. Jiang and W. Hu, N-Type 2D organic single crystals for high-performance organic field-effect transistors and near-infrared phototransistors, *Adv. Mater.*, 2018, **30**, 1706260.
16 J. Qiao, F. Cui, W. Zhang, R. Gui, Z. Fu, M. Sun, P. Lu, H. Yin, X. Du and X. Hao, Enhanced exciton delocalization in organic near-infrared photodetectors via solid additive-mediated J-aggregation, *Adv. Mater.*, 2025, **37**, 2418844.
17 H. Luong, S. Chae, A. Yi, J. Chatsirisupachai, B. Kim, Y. Wan, V. Promarak, H. Kim and T. Nguyen, Ultralow dark current in near-infrared organic photodetector *via* crosslinked conjugated polyelectrolyte hole-transporting layer, *Matter*, 2024, **7**, 2473–2489.
18 T. Rauch, M. Böberl, S. F. Tedde, J. Fürst, M. V. Kovalenko, G. Hesser, U. Lemmer, W. Heiss and O. Hayden, Near-infrared imaging with quantum-dot-sensitized organic photodiodes, *Nat. Photonics*, 2009, **3**, 332–336.
19 X. Wang, L. Lv, L. Li, Y. Chen, K. Zhang, H. Chen, H. Dong, J. Huang, G. Shen, Z. Yang and H. Huang, High-performance all-polymer photoresponse devices based on acceptor–acceptor conjugated polymers, *Adv. Funct. Mater.*, 2016, **26**, 6306–6315.
20 W. Li, Y. Xu, X. Meng, Z. Xiao, R. Li, L. Jiang, L. Cui, M. Zheng, C. Liu, L. Ding and Q. Lin, Visible to near-infrared photodetection based on ternary organic heterojunctions, *Adv. Funct. Mater.*, 2019, **29**, 1808948.
21 M. A. Iqbal, A. Liaqat, S. Hussain, X. Wang, M. Tahir, Z. Urooj and L. Xie, Ultralow-transition-energy organic

complex on graphene for high-performance shortwave infrared photodetection, *Adv. Mater.*, 2020, **32**, 2002628.

22 Y. Yao, Q. Ou, K. Wang, H. Peng, F. Fang, Y. Shi, Y. Wang, D. I. Asperilla, Z. Shuai and P. Samorì, Supramolecular engineering of charge transfer in wide bandgap organic semiconductors with enhanced visible-to-NIR photoresponse, *Nat. Commun.*, 2021, **12**, 3667.

23 B. Yang, Y. Wang, L. Li, J. Zhang, J. Wang, H. Jiao, D. Hao, P. Guo, S. Zeng, Z. Hua and J. Huang, High Performance Ternary Organic Phototransistors with Photoresponse up to 2600 nm at Room Temperature, *Adv. Funct. Mater.*, 2021, **31**, 2103787.

24 Y. Guan, J. Qiao, Y. Liang, H. K. Bisoyi, C. Wang, W. Xu, D. Zhu and Q. Li, A high mobility air-stable n-type organic small molecule semiconductor with high UV–visible-to-NIR photoresponse, *Light: Sci. Appl.*, 2022, **11**, 236.

25 T. Yan, Z. Li, F. Cao, J. Chen, L. Wu and X. Fang, An all-organic self-powered photodetector with ultraflexible dual-polarity output for biosignal detection, *Adv. Mater.*, 2022, **34**, 2201303.

26 T. Kamijo, A. van Breemen, X. Ma, S. Shanmugam, T. Bel, G. de Haas, B. Peeters, R. Petre, D. Tordera, R. Verbeek, H. Akkerman, L. Hagelsieb, F. de Roose, I. Lieberman, F. Yamaguchi, R. Janssen, E. Meulenkamp, A. Kronemeijer and G. Gelinck, A touchless user interface based on a near-infrared-sensitive transparent optical imager, *Nat. Electron.*, 2023, **6**, 451–461.

27 Y. Zhang, Y. Yu, X. Liu, J. Miao, Y. Han, J. Liu and L. Wang, An n-type all-fused-ring molecule with photoresponse to 1000 nm for highly sensitive near-infrared photodetector, *Adv. Mater.*, 2023, **35**, 2211714.

28 Y. Zhang, J. Chen, J. Yang, M. Fu, Y. Cao, M. Dong, J. Yu, S. Dong, X. Yang, L. Shao, Z. Hu, H. Cai, C. Liu and F. Huang, Sensitive SWIR organic photodetectors with spectral response reaching 1.5 μm, *Adv. Mater.*, 2024, **36**, 2406950.

29 W. Jang, H. Luong, M. Kim, T. Nguyen and D. Wang, Enhancing detection frequency and reducing noise through continuous structures via release-controlled transfer toward light-based wireless communication, *Adv. Mater.*, 2024, **36**, 2406316.

30 Y. Huang, L. Shao, Y. Wang, L. Hao, X. Luo, J. Zheng, Y. Cao, S. Li, Z. Tan, S. Li, W. Zhong, S. Dong, X. Yang, J. Benduhn, C. Liu, K. Leo and F. Huang, Bias-switchable photomultiplication and photovoltaic dual-mode near-infrared organic photodetector, *Adv. Mater.*, 2025, **37**, 2500491.

31 D. Meng, R. Zheng, Y. Zhao, E. Zhang, L. Dou and Y. Yang, Near-infrared materials: The turning point of organic photovoltaics, *Adv. Mater.*, 2022, **34**, 2107330.

32 J. Cong, Z. Huang, S. Liu, Z. Luo, F. Liu, Z. Chen, K. Lee, Y. Huang and C. Yang, Efficient SWIR organic photodetectors with spectral detection extending to 1.4 μm using a benzobisthiadiazole-based acceptor, *Small*, 2025, **21**, 2410418.

33 M. He, J. Han, C. Li, C. Han, X. Han, X. Du, H. Luo, H. Yu, J. Gou, Z. Wu and J. Wang, Addressing responsivity-noise trade-off by van der waals multilayer two-phase heterojunction for large LDR organic photodetectors, *Laser Photonics Rev.*, 2025, **19**, 2400554.

34 J. Cui, J. Li, C. Sun, Z. Gu, G. Dai, Y. Tian, J. Li, J. Feng, L. Ye, Y. Yi and W. Zhu, Efficient shortwave infrared photodetection through polymer:cocrystal blend film-based field-effect transistors, *Adv. Opt. Mater.*, 2025, **13**, 2403275.

35 H. Luong, C. Kaiyasuan, A. Yi, S. Chae, B. Kim, P. Panoy, H. Kim, V. Promarak, Y. Miyata, H. Nakayama and T. Nguyen, Highly sensitive resonance-enhanced organic photodetectors for shortwave infrared sensing, *ACS Energy Lett.*, 2024, **9**, 1446–1454.

36 Y. Wei, H. Chen, T. Liu, S. Wang, Y. Jiang, Y. Song, J. Zhang, X. Zhang, G. Lu, F. Huang, Z. Wei and H. Huang, Self-powered organic photodetectors with high detectivity for near infrared light detection enabled by dark current reduction, *Adv. Funct. Mater.*, 2021, **31**, 2106326.

37 V. Pejović, E. Georgitzikis, I. Lieberman, P. Malinowski, P. Heremans and D. Cheyns, Photodetectors based on lead sulfide quantum dot and organic absorbers for multispectral sensing in the visible to short-wave infrared range, *Adv. Funct. Mater.*, 2022, **32**, 2201424.

38 M. Jeong, S. Han, W. Sung, S. Kim, J. Min, M. Kim, W. Choi, H. Lee, D. Lee, M. Kim and K. Cho, Photomultiplication-type organic photodetectors with high EQE-bandwidth product by introducing a perovskite quantum dot interlayer, *Adv. Funct. Mater.*, 2023, **33**, 2300695.

39 Z. Xu, M. He, Q. Wu, C. Wu, X. Li, B. Liu, M. Tang, J. Yao and G. Wei, Ultrafast charge transfer 2D MoS2/organic heterojunction for sensitive photodetector, *Adv. Sci.*, 2023, **10**, 2207743.

40 J. Han, F. Wang, S. Han, W. Deng, X. Du, H. Yu, J. Gou, Q. J. Wang and J. Wang, Recent progress in 2D inorganic/organic charge transfer heterojunction photodetectors, *Adv. Funct. Mater.*, 2022, **32**, 2205150.

41 J. La, S. Lee, A. R. Hong, J. Byun, J. Kang, I. Han, Y. Cho, G. Kang, H. Jang and H. Ko, A super-boosted hybrid plasmonic upconversion process for photodetection at 1550 nm wavelength, *Adv. Mater.*, 2022, **34**, 2106225.

42 Y. Lu, L. Liu, R. Gao, Y. Xiong, P. Sun, Z. Wu, K. Wu, T. Yu, K. Zhang, C. Zhang, T. Bourouina, X. Li and X. Liu, Ultrafast near-infrared pyroelectric detector based on inhomogeneous plasmonic metasurface, *Light: Sci. Appl.*, 2024, **13**, 241.

43 F. P. García de Arquer, D. V. Talapin, V. I. Klimov, Y. Arakawa, M. Bayer and E. H. Sargent, Semiconductor quantum dots: Technological progress and future challenges, *Science*, 2021, **373**, eaaz8541.

44 D. He, M. Zeng, Z. Zhang, Y. Bai, G. Xing, H.-M. Cheng and Y. Lin, Exciton diffusion and dissociation in organic and quantum-dot solar cells, *SmartMat*, 2023, **4**, e1176.

45 O. P. Dimitriev, Dynamics of excitons in conjugated molecules and organic semiconductor systems, *Chem. Rev.*, 2022, **122**, 8487–8593.

46 O. Mikhnenko, P. Blom and T. Nguyen, Exciton diffusion in organic semiconductors, *Energy Environ. Sci.*, 2015, **8**, 1867–1888.

47 H. Najafov, B. Lee, Q. Zhou, L. C. Feldman and V. Podzorov, Observation of long-range exciton diffusion in highly ordered organic semiconductors, *Nat. Mater.*, 2010, **9**, 938–943.

48 F. Sun, X. Zheng, T. Hu, J. Wu, M. Wan, Y. Xiao, T. Cong, Y. Li, B. Xiao, J. Shan, E. Wang, X. Wang and R. Yang, 1,5-Diiodocycloctane: a cyclane solvent additive that can extend the exciton diffusion length in thick film organic solar cells, *Energy Environ. Sci.*, 2024, **17**, 1916–1930.

49 L. Yang, D. Guo, J. Li, G. He, D. Yang, A. Vadim and D. Ma, Low-cost copper electrode for high-performance panchromatic multiplication-type organic photodetectors with optical microcavity effect, *Adv. Funct. Mater.*, 2022, **32**, 2108839.

50 A. Joseph, A. Pillai, M. Sundaram, B. Nanda and M. Namboothiry, Mitigation of illumination sensitive dark current in broadband organic photodiode enabled by robust interface engineering, *Adv. Energy Mater.*, 2025, 2500748.

51 H. Gu, T. Zhang, Y. Wang, T. Zhou and H. Chen, 2D compounds with heterolayered architecture for infrared photodetectors, *Chem. Sci.*, 2024, **15**, 15983–16005.

52 M. Kim, S. Ryu, S. Park, Y. Pu and T. Park, Designs and understanding of small molecule-based non-fullerene acceptors for realizing commercially viable organic photovoltaics, *Chem. Sci.*, 2021, **12**, 14004–14023.

53 G. J. Hedley, A. Ruseckas and I. D. W. Samuel, Light harvesting for organic photovoltaics, *Chem. Rev.*, 2017, **117**, 796–837.

54 H. Ren, J. Chen, Y. Li and J. Tang, Recent progress in organic photodetectors and their applications, *Adv. Sci.*, 2021, **8**, 2002418.

55 N. S. Sariciftci, L. Smilowitz, A. J. Heeger and F. Wudl, Photoinduced electron transfer from a conducting polymer to buckminsterfullerene, *Science*, 1992, **258**, 1474–1476.

56 G. Yu, J. Gao, J. C. Hummelen, F. Wudl and A. J. Heeger, Polymer photovoltaic cells: Enhanced efficiencies via a network of internal donor-acceptor heterojunctions, *Science*, 1995, **270**, 1789–1791.

57 M. Liu, J. Wei, L. Qi, J. An, X. Liu, Y. Li, Z. Shi, D. Li, K. S. Novoselov, C.-W. Qiu and S. Li, Photogating-assisted tunneling boosts the responsivity and speed of heterogeneous WSe2/Ta2NiSe5 photodetectors, *Nat. Commun.*, 2024, **15**, 141.

58 J. Wu, Z. Wen, B. Guo, Y. Wu, B. Li, C. Wang, L. Wu, T. Zhang and R. Che, Dielectric-free MoS2/VO2 junction field-effect transistor with sensitive and ultrafast photoresponse for light encrypted communication, *Adv. Mater.*, 2025, **37**, 2503294.

59 M. Yu, Z.-C. Wan, S.-W. Song, Z.-Y. Yang, M. Suzuki and H. Yamada, Dual-benefit strategy for developing an efficient photodetector with prompt response to UV-near IR radiations: in situ synthesis and crystallization through a simple one-step annealing, *J. Mater. Chem. A*, 2024, **12**, 19288–19297.

60 J. Li, W. Zhu, Y. Han, Y. Geng and W. Hu, Polymer: Non-fullerene acceptor heterojunction-based phototransistor for short-wave infrared photodetection, *Nano Res.*, 2024, **17**, 3087–3095.

61 Z. Sa, F. Liu, X. Zhuang, Y. Yin, Z. Lv, M. Wang, J. Zhang, K. Song, F. Chen and Z.-x. Yang, Toward high bias-stress stability p-type GaSb nanowire field-effect-transistor for gate-controlled near-infrared photodetection and photocommunication, *Adv. Funct. Mater.*, 2023, **33**, 2304064.

62 S. Ghosh, A. Varghese, K. Thakar, S. Dhara and S. Lodha, Enhanced responsivity and detectivity of fast WSe2 phototransistor using electrostatically tunable in-plane lateral p–n homojunction, *Nat. Commun.*, 2021, **12**, 3336.

63 W. Yang, S. Fan, H. Yang, S. Li, S. Chen, F. Hu, X. Wang, J. Zhang and X. Liu, Photo-induced electrical gating with the inserting of an interfacial carrier blocking layer for organic/graphene phototransistors, *Adv. Opt. Mater.*, 2024, **12**, 2302937.

64 Y. Tang, F. Wu, F. Chen, Y. Zhou, P. Wang, M. Long, W. Zhou, Z. Ning, J. He, F. Gong, Z. Zhu, S. Qin and W. Hu, A colloidal-quantum-dot infrared photodiode with high photoconductive gain, *Small*, 2018, **14**, 1803158.

65 S. Bai, R. Li, H. Huang, Y. Qi, Y. Xu, J. Song, F. Yao, O. J. Sandberg, P. Meredith, A. Armin and Q. Lin, Transient analysis of photomultiplication-type organic photodiodes, *Appl. Phys. Rev.*, 2022, **9**, 021405.

66 G. H. Lee, J.-H. Kim, H. Kang, J. Jeong, J. W. Chung, D. Kim, J. Park, Y. Yun and S. Park, Light-mediated photomultiplication via cascade energy transfer in organic photodiode, *Adv. Funct. Mater.*, 2025, **35**, 2423993.

67 M. Shou, Q. Zhang, S. Xiong, T. Han, J. Zhou, N. Zheng, Z. Xie and L. Liu, Simultaneous photomultiplication improvement and response acceleration for high-performance lateral polymer photodetectors based on bulk heterojunction, *ACS Appl. Mater. Interfaces*, 2021, **13**, 5293–5301.

68 J. Tian, An overview of pyroelectric photodetector: Photoresponse mechanisms and applications, *AIP Adv.*, 2023, **13**, 050701.

69 Y. Zhao, L. Liu, F. Zhang, C.-A. Di and D. Zhu, Advances in organic thermoelectric materials and devices for smart applications, *SmartMat*, 2021, **2**, 426–445.

70 T. Li, J.-C. Liu, E.-P. Liu, B.-T. Liu, J.-Y. Wang, P.-Y. Liao, J.-H. Jia, Y. Feng and M.-L. Tong, NIR-II photothermal conversion and imaging based on a cocrystal containing twisted components, *Chem. Sci.*, 2024, **15**, 1692–1699.

71 X. Guo, X. Lu, P. Jiang and X. Bao, Touchless thermosensation enabled by flexible infrared photothermoelectric detector for temperature prewarning function of electronic skin, *Adv. Mater.*, 2024, **36**, 2313911.

72 C. Costa, V. Cardoso, P. Martins, D. Correia, R. Gonçalves, P. Costa, V. Correia, C. Ribeiro, M. Fernandes, P. Martins and S. Lanceros-Méndez, Smart and multifunctional materials based on electroactive poly(vinylidene fluoride):

Recent advances and opportunities in sensors, actuators, energy, environmental, and biomedical applications, *Chem. Rev.*, 2023, **123**, 11392–11487.

73 M. Fattori, S. Cardarelli, J. Fijn, P. Harpe, M. Charbonneau, D. Locatelli, S. Lombard, C. Laugier, L. Tournon, S. Jacob, K. Romanjek, R. Coppard, H. Gold, M. Adler, M. Zirkl, J. Groten, A. Tschepp, B. Lamprecht, M. Postl, B. Stadlober, J. Socratous and E. Cantatore, A printed proximity-sensing surface based on organic pyroelectric sensors and organic thin-film transistor electronics, *Nat. Electron.*, 2022, **5**, 289–299.

74 K. Xie, J. Housseini, P. M. Resende, F. Le Goupil, J.-D. Isasa, S. Tencé-Girault, G. Fleury, H. Kellay and G. Hadziioannou, Enhanced pyroelectricity over extended thermal range in flexible polymer thin films, *Adv. Funct. Mater.*, 2024, **34**, 2411397.

75 F. P. García de Arquer, A. Armin, P. Meredith and E. Sargent, Solution-processed semiconductors for next-generation photodetectors, *Nat. Rev. Mater.*, 2017, **2**, 16100.

76 H. Shirakawa, E. Louis, A. MacDiarmid, C. Chiang and A. Heeger, Synthesis of electrically conducting organic polymers: halogen derivatives of polyacetylene, (CH), *J. Chem. Soc., Chem. Commun.*, 1977, 578–580.

77 A. Heeger, Semiconducting polymers: the third generation, *Chem. Soc. Rev.*, 2010, **39**, 2354–2371.

78 J. Huang, J. Lee, J. Vollbrecht, V. Brus, A. Dixon, D. Cao, Z. Zhu, Z. Du, H. Wang, K. Cho, G. Bazan and T. Nguyen, A high-performance solution-processed organic photodetector for near-infrared sensing, *Adv. Mater.*, 2020, **32**, 1906027.

79 Y. Wu, K. Fukuda, T. Yokota and T. Someya, A Highly responsive organic image sensor based on a two-terminal organic photodetector with photomultiplication, *Adv. Mater.*, 2019, **31**, 1903687.

80 N. Li, Z. Lan, Y. S. Lau, J. Xie, D. Zhao and F. Zhu, SWIR photodetection and visualization realized by incorporating an organic SWIR sensitive bulk heterojunction, *Adv. Sci.*, 2020, **7**, 2000444.

81 Z. He, J. Han, X. Du, L. Cao, J. Wang, C. Zheng, H. Lin and S. Tao, Photomemory and pulse monitoring featured solution-processed near-infrared graphene/organic phototransistor with detectivity of 2.4×10^{13} jones, *Adv. Funct. Mater.*, 2021, **31**, 2103988.

82 Z. Zhao, B. Liu, C. Xie, Y. Ma, J. Wang, M. Liu, K. Yang, Y. Xu, J. Zhang, W. Li, L. Shen and F. Zhang, Highly sensitive, sub-microsecond polymer photodetectors for blood oxygen saturation testing, *Sci. China Chem.*, 2021, **64**, 1302–1309.

83 B. Park, J. Jung, D. Lim, H. Lee, S. Park, M. Kyeong, S. Ko, S. Eom, S. Lee, C. Lee and S. Yoon, Significant dark current suppression in organic photodetectors using side chain fluorination of conjugated polymer, *Adv. Funct. Mater.*, 2022, **32**, 2108026.

84 P. Jacoutot, A. D. Scaccabarozzi, T. Zhang, Z. Qiao, F. Aniés, M. Neophytou, H. Bristow, R. Kumar, M. Moser, A. D. Nega, A. Schiza, A. Dimitrakopoulou-Strauss, V. G. Gregoriou, T. D. Anthopoulos, M. Heeney, I. McCulloch, A. A. Bakulin, C. L. Chochos and N. Gasparini, Infrared organic photodetectors employing ultralow bandgap polymer and non-fullerene acceptors for biometric monitoring, *Small*, 2022, **18**, 2200580.

85 Z. Du, H. M. Luong, S. Sabury, A. L. Jones, Z. Zhu, P. Panoy, S. Chae, A. Yi, H. J. Kim, S. Xiao, V. V. Brus, G. N. Manjunatha Reddy, J. R. Reynolds and T. Nguyen, High-performance wearable organic photodetectors by molecular design and green solvent processing for pulse oximetry and photoplethysmography, *Adv. Mater.*, 2024, **36**, 2310478.

86 C. Zhang, A. Song, Q. Huang, Y. Cao, Z. Zhong, Y. Liang, K. Zhang, C. Liu, F. Huang and Y. Cao, All-polymer solar cells and photodetectors with improved stability enabled by terpolymers containing antioxidant side chains, *Nano-Micro Lett.*, 2023, **15**, 140.

87 S. Lee, J. Lee, H. R. Sim, C. So and D. S. Chung, Shortwave infrared organic photodiodes realized by polaron engineering, *Adv. Mater.*, 2024, **36**, 2310250.

88 B. Du, S. Xiong, L. Sun, Y. Tagawa, D. Inoue, D. Hashizume, W. Wang, R. Guo, T. Yokota, S. Wang, Y. Ishida, S. Lee, K. Fukuda and T. Someya, A water-resistant, ultrathin, conformable organic photodetector for vital sign monitoring, *Sci. Adv.*, 2024, **10**, eadp2679.

89 M. Hun Jee, B. Park, A. Young Lee, S. Rhee, M. Lim, J. Min Ha, N. Kim, F. Zhang, J. Ha, H. Ahn, J. Kim, M. Han, S. Cheol Yoon, S. Ko and H. Woo, Photo-crosslinking and layer-by-layer processed organic photodetectors with remarkably suppressed dark current, *Chem. Eng. J.*, 2024, **490**, 151624.

90 X. Chen, Y. Zhu, Y. Xu, M. Rao, P. Pang, B. Zhang, C. Xu, W. Ni, G. Li, J. Wu, M. Li, Y. Chen and Y. Geng, Design of ultra-narrow bandgap polymer acceptors for high-sensitivity flexible all-polymer short-wavelength infrared photodetectors, *Angew. Chem., Int. Ed.*, 2024, **18**, e202413965.

91 X. Wang, Z. Wang, J. Han, H. Zhu, J. Liu and W. Qiao, Manipulating electron linking units and side chains for high-performance all-polymer photodetectors with stability over 5000 h, *Chem. Eng. J.*, 2024, **484**, 149653.

92 C. Liu, L. Shao, S. Chen, Z. Hu, H. Cai and F. Huang, Recent progress in π-conjugated polymers for organic photovoltaics: Solar cells and photodetectors, *Prog. Polym. Sci.*, 2023, **143**, 101711.

93 T. Mikie, T. Morioku, S. Suruga, M. Hada, Y. Sato, H. Ohkita and I. Osaka, Dithienonaphthobisthiadiazole synthesized by thienannulation of electron-deficient rings: an acceptor building unit for high-performance π-conjugated polymers, *Chem. Sci.*, 2024, **15**, 19991–20001.

94 X. Gong, M. Tong, Y. Xia, W. Cai, J. S. Moon, Y. Cao, G. Yu, C.-L. Shieh, B. Nilsson and A. J. Heeger, High-detectivity polymer photodetectors with spectral response from 300 nm to 1450 nm, *Science*, 2009, **325**, 1665–1667.

95 J. Qi, J. Han, X. Zhou, D. Yang, J. Zhang, W. Qiao, D. Ma and Z. Y. Wang, Optimization of broad-response and high-detectivity polymer photodetectors by bandgap

engineering of weak donor–strong acceptor polymers, *Macromolecules*, 2015, **48**, 3941–3948.

96 L. Zheng, T. Zhu, W. Xu, L. Liu, J. Zheng, X. Gong and F. Wudl, Solution-processed broadband polymer photodetectors with a spectral response of up to 2.5 μm by a low bandgap donor–acceptor conjugated copolymer, *J. Mater. Chem. C*, 2018, **6**, 3634–3641.

97 X. Liu, C. Anderson and Y. Liu, p-Azaquinodimethane: A versatile quinoidal moiety for functional materials discovery, *Acc. Chem. Res.*, 2023, **56**, 1669–1682.

98 X. Liu, B. He, C. Anderson, J. Kang, T. Chen, J. Chen, S. Feng, L. Zhang, M. Kolaczkowski, S. Teat, M. Brady, C. Zhu, L. Wang, J. Chen and Y. Liu, Para-azaquinodimethane: A compact quinodimethane variant as an ambient stable building block for high-performance low band gap polymers, *J. Am. Chem. Soc.*, 2017, **139**, 8355–8363.

99 C. Liu, X. Liu, G. Zheng, X. Gong, C. Yang, H. Liu, L. Zhang, C. L. Anderson, B. He, L. Xie, R. Zheng, H. Liang, Q. Zhou, Z. Zhang, J. Chen and Y. Liu, An unprecedented quinoid–donor–acceptor strategy to boost the carrier mobilities of semiconducting polymers for organic field-effect transistors, *J. Mater. Chem. A*, 2021, **9**, 23497–23505.

100 L. Zhang, T. Yang, L. Shen, Y. Fang, L. Dang, N. Zhou, X. Guo, Z. Hong, Y. Yang, H. Wu, J. Huang and Y. Liang, Toward highly sensitive polymer photodetectors by molecular engineering, *Adv. Mater.*, 2015, **27**, 6496–6503.

101 X. Chen, Y. Zhu, Y. Xu, M. Rao, P. Pang, B. Zhang, C. Xu, W. Ni, G. Li, J. Wu, M. Li, Y. Chen and Y. Geng, Design of ultra-narrow bandgap polymer acceptors for high-sensitivity flexible all-polymer short-wavelength infrared photodetectors, *Angew. Chem., Int. Ed.*, 2025, **64**, e202413965.

102 C. Zhang, R. Yu, Q. Lv, S. Li, H. Yuan, B. Huang and Z. Tan, Progress in non-fullerene acceptors: Evolution from small to giant molecules, *ChemSusChem*, 2024, **18**, e202401138.

103 Q. Yue, W. Liu and X. Zhu, N-type molecular photovoltaic materials: design strategies and device applications, *J. Am. Chem. Soc.*, 2020, **142**, 11613–11628.

104 J. Yi, G. Zhang, H. Yu and H. Yan, Advantages, challenges and molecular design of different material types used in organic solar cells, *Nat. Rev. Mater.*, 2024, **9**, 46–62.

105 B. Xie, Z. Chen, L. Ying, F. Huang and Y. Cao, Near-infrared organic photoelectric materials for light-harvesting systems: Organic photovoltaics and organic photodiodes, *InfoMat*, 2020, **2**, 57–91.

106 M. Xie, Z. Wei and K. Lu, Quinoxaline-based Y-type acceptors for organic solar cells, *Chem. Sci.*, 2024, **15**, 8265–8279.

107 Y. Wang, M. Yang, B. Yin, B. Wu, G. Liu, S. Jeong, Y. Zhang, C. Yang, Z. He, F. Huang, Y. Cao and C. Duan, An A–D–A′–D–A-type narrow bandgap electron acceptor based on selenophene-flanked diketopyrrolopyrrole for sensitive near-infrared photodetection, *ACS Appl. Mater. Interfaces*, 2024, **16**, 66846–66856.

108 M. Yang, B. Yin, G. Hu, Y. Cao, S. Lu, Y. Chen, Y. He, X. Yang, B. Huang, J. Li, B. Wu, S. Pang, L. Shen, Y. Liang, H. Wu, L. Lan, G. Yu, F. Huang, Y. Cao and C. Duan, Sensitive short-wavelength infrared photodetection with a quinoidal ultralow band-gap n-type organic semiconductor, *Chem*, 2024, **10**, 1425–1444.

109 M. Liu, X. Han, H. Chen, Q. Peng and H. Huang, A molecular descriptor of intramolecular noncovalent interaction for regulating optoelectronic properties of organic semiconductors, *Nat. Commun.*, 2023, **14**, 2500.

110 H. Huang, L. Yang, A. Facchetti and T. Marks, Organic and polymeric semiconductors enhanced by noncovalent conformational locks, *Chem. Rev.*, 2017, **117**, 10291–10318.

111 X. Zhang, X. Gu and H. Huang, Low-cost nonfused-ring electron acceptors enabled by noncovalent conformational locks, *Acc. Chem. Res.*, 2024, **57**, 981–991.

112 B. Yin, X. Zhou, Y. Li, G. Hu, W. Wei, M. Yang, S. Jeong, W. Deng, B. Wu, Y. Cao, B. Huang, L. Pan, X. Yang, Z. Fu, Y. Fang, L. Shen, C. Yang, H. Wu, L. Lan, F. Huang, Y. Cao and C. Duan, Sensitive organic photodetectors with spectral response up to 1.3 μm using a quinoidal molecular semiconductor, *Adv. Mater.*, 2024, **36**, 2310811.

113 L. Shao, L. Hong, Y. Cao, H. Tang, Y. Huang, X. Xia, Y. Bai, M. Dong, X. Zhang, X. Lu, X. Yang, C. Liu, F. Huang and Y. Cao, Spiro-conjugation in narrow-bandgap nonfullerene acceptors enables broader spectral response and higher detectivity for near-infrared organic photodetectors, *Adv. Opt. Mater.*, 2023, **11**, 2202823.

114 Y. Zhang, Q. Wei, Z. He, Y. Wang, T. Shan, Y. Fu, X. Guo and H. Zhong, Efficient optoelectronic devices enabled by near-infrared organic semiconductors with a photoresponse beyond 1050 nm, *ACS Appl. Mater. Interfaces*, 2022, **14**, 31066–31074.

115 L. Shao, Y. Huang, L. Hong, Z. Xu, X. Yang, C. Liu, F. Huang and Y. Cao, Optimizing the π-Bridge of Non-fullerene Acceptors to Suppress Dark Current in NIR Organic Photodetectors, *Chem. Res. Chin. Univ.*, 2024, **40**, 712–721.

116 W. Peng, G. Zhang, M. Zhu, H. Xia, Y. Zhang, H. Tan, Y. Liu, W. Chi, Q. Peng and W. Zhu, Simple-structured NIR-absorbing small-molecule acceptors with a thiazolothiazole core: Multiple noncovalent conformational locks and d–a effect for efficient OSCs, *ACS Appl. Mater. Interfaces*, 2019, **11**, 48128–48133.

117 Z. Han, C. Zhang, T. He, J. Gao, Y. Hou, X. Gu, J. Lv, N. Yu, J. Qiao, S. Wang, C. Li, J. Zhang, Z. Wei, Q. Peng, Z. Tang, X. Hao, G. Long, Y. Cai, X. Zhang and H. Huang, Precisely manipulating molecular packing via tuning alkyl side-chain topology enabling high-performance nonfused-ring electron acceptors, *Angew. Chem., Int. Ed.*, 2024, **63**, e202318143.

118 J. Liu, J. Jiang, S. Wang, T. Li, X. Jing, Y. Liu, Y. Wang, H. Wen, M. Yao, X. Zhan and L. Shen, Fast response organic tandem photodetector for visible and near-infrared digital optical communications, *Small*, 2021, **17**, 2101316.

119 X. Liao, W. Xie, Z. Han, Y. Cui, X. Xia, X. Shi, Z. Yao, X. Xu, X. Lu and Y. Chen, NIR photodetectors with highly efficient detectivity enabled by 2D fluorinated

dithienopicenocarbazole-based ultra-narrow bandgap acceptors, *Adv. Funct. Mater.*, 2022, **32**, 2204255.

120 W. Wang, X. Miao, G. Cai, L. Ding, Y. Li, T. Li, Y. Zhu, L. Tao, Y. Jia, Y. Liang, X. Lu, Y. Fang, Y. Yi and Y. Lin, Enhancing transition dipole moments of heterocyclic semiconductors via rational nitrogen-substitution for sensitive near infrared detection, *Adv. Mater.*, 2022, **34**, 2201600.

121 Y. Song, Z. Zhong, P. He, G. Yu, Q. Xue, L. Lan and F. Huang, Doping compensation enables high-detectivity infrared organic photodiodes for image sensing, *Adv. Mater.*, 2022, **34**, 2201827.

122 S. Park, C. Labanti, R. Pacalaj, T. Lee, Y. Dong, Y. Chin, J. Luke, G. Ryu, D. Minami, S. Yun, J. Park, F. Fang, K. Park, J. Durrant and J. Kim, The state-of-the-art solution-processed single component organic photodetectors achieved by strong quenching of intermolecular emissive state and high quadrupole moment in non-fullerene acceptors, *Adv. Mater.*, 2023, **35**, 2306655.

123 S. Zhang, Z. Li, J. Li, B. Wang, F. Chen, X. Li, S. Liu, J. W. Y. Lam, G. Xing, J. Li, Z. Zhao, F. Kang, G. Wei and B. Z. Tang, Organic near-infrared photodetectors with photoconductivity-enhanced performance, *Aggregate*, 2023, **4**, e345.

124 G. Suthar, Y.-T. Hsiao, K.-W. Tsai, C.-Y. Liao, C.-W. Chu, Y.-M. Chang and F.-C. Chen, Morphological effects on the performance of broadband organic photomultiplication photodetectors containing selenium substituted non-fullerene acceptors, *Adv. Funct. Mater.*, 2023, **33**, 2301538.

125 Y. Huang, Z. Huang, T. Wang, P. Chaudhary, J. Hsu and K. Lee, A promising non-fullerene acceptor for near-infrared organic photodetectors operating with low dark current and high response speed, *Chem. Eng. J.*, 2023, **464**, 142633.

126 H. Chandran, R. Ma, Z. Xu, J. Veetil, Y. Luo, T. Dela Peña, I. Gunasekaran, S. Mahadevan, K. Liu, Y. Xiao, H. Xia, J. Wu, M. Li, S. Tsang, X. Yu, W. Chen and G. Li, High-detectivity all-polymer photodiode empowers smart vitality surveillance and computational imaging rivaling silicon diodes, *Adv. Mater.*, 2024, **36**, 2407271.

127 X. Zhu, Y. Zhang, H. Li, Y. Zhang, J. Miao, J. Liu and L. Wang, A fully-fluorinated all-fused-ring acceptor for highly sensitive near-infrared organic photodetectors, *Sci. Bull.*, 2024, **69**, 2679–2682.

128 Y. Zhu, H. Chen, R. Han, H. Qin, Z. Yao, H. Liu, Y. Ma, X. Wan, G. Li and Y. Chen, High-speed flexible near-infrared organic photodiode for optical communication, *Natl. Sci. Rev.*, 2024, **11**, nwad311.

129 K. Huang, B. Jiang, H. Lu, Y. Xue, C. Lu, Y. Chang, C. Huang, S. Chien, C. Chen and Y. Cheng, Electron-rich heptacyclic S,N heteroacene enabling C-shaped A-D-A-type electron acceptors with photoelectric response beyond 1000 nm for highly sensitive near-infrared photodetectors, *Adv. Sci.*, 2025, **12**, 2413045.

130 B. Xie, R. Xie, K. Zhang, Q. Yin, Z. Hu, G. Yu, F. Huang and Y. Cao, Self-filtering narrowband high performance organic photodetectors enabled by manipulating localized Frenkel exciton dissociation, *Nat. Commun.*, 2020, **11**, 2871.

131 J. H. Kim, A. Liess, M. Stolte, A.-M. Krause, V. Stepanenko, C. Zhong, D. Bialas, F. Spano and F. Würthner, An Efficient Narrowband Near-Infrared at 1040 nm Organic Photodetector Realized by Intermolecular Charge Transfer Mediated Coupling Based on a Squaraine Dye, *Adv. Mater.*, 2021, **33**, 2100582.

132 J. Kublitski, A. Fischer, S. Xing, L. Baisinger, E. Bittrich, D. Spoltore, J. Benduhn, K. Vandewal and K. Leo, Enhancing sub-bandgap external quantum efficiency by photomultiplication for narrowband organic near-infrared photodetectors, *Nat. Commun.*, 2021, **12**, 4259.

133 Z. Zhao, M. Liu, K. Yang, C. Xu, Y. Guan, X. Ma, J. Wang and F. Zhang, Highly sensitive narrowband photomultiplication-type organic photodetectors prepared by transfer-printed technology, *Adv. Funct. Mater.*, 2021, **31**, 2106009.

134 J. Vanderspikken, Q. Liu, Z. Liu, T. Vandermeeren, T. Cardeynaels, S. Gielen, B. Van Mele, N. Van den Brande, B. Champagne, K. Vandewal and W. Maes, Tuning electronic and morphological properties for high-performance wavelength-selective organic near-infrared cavity photodetectors, *Adv. Funct. Mater.*, 2022, **32**, 2108146.

135 Q. Liu, S. Zeiske, X. Jiang, D. Desta, S. Mertens, S. Gielen, R. Shanivarasanthe, H.-G. Boyen, A. Armin and K. Vandewal, Electron-donating amine-interlayer induced n-type doping of polymer:nonfullerene blends for efficient narrowband near-infrared photo-detection, *Nat. Commun.*, 2022, **13**, 5194.

136 R. Ollearo, X. Ma, H. Akkerman, M. Fattori, M. Dyson, A. van Breemen, S. Meskers, W. Dijkstra, R. Janssen and G. Gelinck, Vitality surveillance at distance using thin-film tandem-like narrowband near-infrared photodiodes with light-enhanced responsivity, *Sci. Adv.*, 2023, **9**, eadf9861.

137 J. Jiang, Y. Deng, J. Li, M. Guo, J. Sun, X. Li, Z. Lou, Y. Hou, Y. Hu and F. Teng, Multifunctional photodetector with tunable response bandwidth and polarization sensitivity, *Adv. Funct. Mater.*, 2024, **34**, 2400175.

138 Z. Ye, X. Li, H. Li, Z. Xu, K. Ke, Y. Gao, X. Tang, F. S. Yang, X. Xu, X. Li, F. Kang and G. Wei, Optical resonant cavities carving pathways in tunable wavelength sensitive visible-NIR organic photodetectors, *Nano Mater. Sci.*, 2024, DOI: **10.1016/j.nanoms.2024.10.001**.

139 M. Brunetta, Z. Qiao, A. Zamhuri, F. Furlan, M. Rimmele, P. A. Gilhooly-Finn, L. M. Cowen, F. Aniés, P. Sukpoonprom, S. Cazaly, J. Panidi, F. Eisner, M. Heeney, B. C. Schroeder and N. Gasparini, Narrowband detection via charge collection narrowing organic photodetector enabled by low bandgap random terpolymer for biometric sensing, *Adv. Funct. Mater.*, 2025, 2422637.

140 Y. Jiang, S. Sun, R. Xu, F. Liu, X. Miao, G. Ran, K. Liu, Y. Yi, W. Zhang and X. Zhu, Non-fullerene acceptor with asymmetric structure and phenyl-substituted alkyl side

chain for 20.2% efficiency organic solar cells, *Nat. Energy*, 2024, **9**, 975–986.

141 J. He, Y. J. Jo, X. Sun, W. Qiao, J. Ok, T.-i. Kim and Z. a. Li, Squaraine dyes for photovoltaic and biomedical applications, *Adv. Funct. Mater.*, 2021, **31**, 2008201.

142 J. Csucker, E. Didier, J. Pedro Ferreira Assunção, D. Rentsch, R. Kothandaraman, D. Bachmann, I. Shorubalko, F. Nüesch, R. Hany and M. Bauer, Squaraine dyes for organic photomultiplication photodetectors with 220% external quantum efficiency at 1240 nm, *Adv. Sci.*, 2025, **12**, 2502320.

143 J. He, Z. Wang, Y. Gao, B. Xiong, M. Shao and Z. a. Li, Ladder-type π-conjugated polysquaraines for near-infrared organic photodetectors, *Macromolecules*, 2024, **57**, 6123–6132.

144 J. He, Z. Wang, Y. Gao, X. Yu, W. Qiao, M. Shao and Z. a. Li, Near-infrared organic photodetectors with ultralow dark currents based on carbazole-bridged pyrrolic polysquaraines, *Adv. Opt. Mater.*, 2024, **12**, 2301361.

145 J. Kim, A. Liess, M. Stolte, A. Krause, V. Stepanenko, C. Zhong, D. Bialas, F. Spano and F. Würthner, An efficient narrowband near-infrared at 1040 nm organic photodetector realized by intermolecular charge transfer mediated coupling based on a squaraine dye, *Adv. Mater.*, 2021, **33**, 2100582.

146 J. Zeng, Z. Ren, D. Lin, W. Gong, G. Song, L. Wu, S. Liu, J. Wu, T. Jia, R. Xie and Z. He, Molecular-device co-engineering of ultra-low dark current SWIR organic photodetectors for high-quality blood-pressure monitoring and optical communication, *Adv. Mater.*, 2025, e09923.

147 J.-W. Ha, H. J. Eun, B. Park, H. Ahn, D. R. Hwang, Y. S. Shim, J. Heo, C. Lee, S. C. Yoon, J. H. Kim and S.-J. Ko, Effect of cyano substitution on non-fullerene acceptor for near-infrared organic photodetectors above 1000 nm, *Adv. Funct. Mater.*, 2023, **33**, 2211486.

148 W. Zhong, X. Wang, W. Wang, Z. Song, Y. Tang, B. Chen, T. Yang and Y. Liang, Fast near-infrared organic photodetectors with enhanced detectivity by molecular engineering of acceptor materials, *Adv. Sci.*, 2025, **12**, 2410332.

149 K. Cho, J.-W. Ha, M. Nam, C. Lee, S. J. You, A. Y. Lee, S. C. Yoon, M. Han, J. H. Kim, S.-J. Ko and D.-H. Ko, Crystallization-driven optimization of morphology and performance in near-infrared organic photodetectors via alkyl side chain tuning of narrow bandgap non-fullerene acceptors, *Adv. Funct. Mater.*, 2024, **34**, 2400676.

150 J. Vanderspikken, W. Maes and K. Vandewal, Wavelength-selective organic photodetectors, *Adv. Funct. Mater.*, 2021, **31**, 2104060.

151 Y. Wang, J. Kublitski, S. Xing, F. Dollinger, D. Spoltore, J. Benduhn and K. Leo, Narrowband organic photodetectors – towards miniaturized, spectroscopic sensing, *Mater. Horiz.*, 2022, **9**, 220–251.

152 J. Kim, T. Schembri, D. Bialas, M. Stolte and F. Würthner, Slip-stacked J-aggregate materials for organic solar cells and photodetectors, *Adv. Mater.*, 2022, **34**, 2104678.

153 B. Siegmund, A. Mischok, J. Benduhn, O. Zeika, S. Ullbrich, F. Nehm, M. Böhm, D. Spoltore, H. Fröb, C. Körner, K. Leo and K. Vandewal, Organic narrowband near-infrared photodetectors based on intermolecular charge-transfer absorption, *Nat. Commun.*, 2017, **8**, 15421.

154 J. Khan, R. T. M. Ahmad, J. Tan, R. Zhang, U. Khan and B. Liu, Recent advances in 2D organic−inorganic heterostructures for electronics and optoelectronics, *SmartMat*, 2023, **4**, e1156.

155 F. Cao, W. Tian, K. Deng, M. Wang and L. Li, Self-powered UV–Vis–NIR photodetector based on conjugated-polymer/CsPbBr3 nanowire array, *Adv. Funct. Mater.*, 2019, **29**, 1906756.

156 C. Li, H. Wang, F. Wang, T. Li, M. Xu, H. Wang, Z. Wang, X. Zhan, W. Hu and L. Shen, Ultrafast and broadband photodetectors based on a perovskite/organic bulk heterojunction for large-dynamic-range imaging, *Light: Sci. Appl.*, 2020, **9**, 31.

157 N. Ding, Y. Wu, W. Xu, J. Lyu, Y. Wang, L. Zi, L. Shao, R. Sun, N. Wang, S. Liu, D. Zhou, X. Bai, J. Zhou and H. Song, A novel approach for designing efficient broadband photodetectors expanding from deep ultraviolet to near infrared, *Light: Sci. Appl.*, 2022, **11**, 91.

158 M. Sulaman, S. Yang, H. Guo, C. Li, A. Imran, A. Bukhtiar, M. Qasim, Z. Ge, Y. Song, Y. Jiang and B. Zou, Synergetic enhancement of CsPbI3 nanorod-based high-performance photodetectors via PbSe quantum dot interface engineering, *Chem. Sci.*, 2024, **15**, 8514–8529.

159 J. Qiao, Q. Wang, J. Wang, J. Liu, W. Zhang, X. Liao, L. Ye, H. Yin and X. Hao, High-performance broad-spectrum photodetector by suppressing stray electrons by adopting a hybrid CQD/organic architecture, *Aggregate*, 2025, **6**, e722.

160 X. Hou, K. Zhang, J. Li, J. Liang, W. Li, D. Yan, L. Liu and J. Zhang, Improved performance of ZnO based inverted organic photodetectors with morphological and interfacial modification, *J. Mater. Chem. C*, 2023, **11**, 9229–9237.

161 X. Wang, W. Song, B. Liu, G. Chen, D. Chen, C. Zhou and G. Shen, High-performance organic-inorganic hybrid photodetectors based on P3HT:CdSe nanowire heterojunctions on rigid and flexible substrates, *Adv. Funct. Mater.*, 2013, **23**, 1202–1209.

162 F. Eisner, G. Foot, J. Yan, M. Azzouzi, D. G. Georgiadou, W. Y. Sit, Y. Firdaus, G. Zhang, Y. Lin, H. Yip, T. D. Anthopoulos and J. Nelson, Emissive charge-transfer states at hybrid inorganic/organic heterojunctions enable low non-radiative recombination and high-performance photodetectors, *Adv. Mater.*, 2022, **34**, 2104654.

163 L. Sun, Y. Wang, F. Yang, X. Zhang and W. Hu, Cocrystal engineering: A collaborative strategy toward functional materials, *Adv. Mater.*, 2019, **31**, 1902328.

164 C. Shan, D. Luo, J. Zeng, T. Dai, X. Gu, X. Xu, Z. Li, E. Zhou, B. Xu and A. Kyaw, High-detectivity photomultiplication-type organic photodetectors with non-fused ring electron acceptor enabled by solid additive-induced efficient hole tunneling injection, *Chem. Eng. J.*, 2025, **505**, 159658.

165 Z. He, X. Du, X. Yu, L. Cao, M. He, J. Han, H. Lin, J. Wang, C. Zheng and S. Tao, Reverse-distribution phase featured gradient heterojunction: A universal strategy to realize high-performance near-infrared organic photodetectors for real-time arterial monitoring, *Nano Energy*, 2023, **114**, 108673.

166 Y. Zhang, W. Chen, J. Miao, J. Liu and L. Wang, Flexible near-infrared organic photodetectors with ultralow dark current by layer-by-layer blade coating, *Adv. Opt. Mater.*, 2024, **12**, 2401891.

167 S. Weng, M. Zhao, D. Jiang and Q. Liang, Broadband organic ternary bulk heterojunctions photodetector based on non-fullerene acceptor with enhanced flat-spectrum response range from 200 to 1100 nm, *J. Phys. Chem. Lett.*, 2022, **13**, 10577–10588.

168 P. Bi, J. Wang, Z. Chen, Z. Li, C. Tan, J. Qiao, J. Dai, T. Zhang, J. Gao, W. Goh, C. Lyu, C. Jiang, X. Hao, J. Hou and L. Yang, Weak near-infrared light visualization enabled by smart multifunctional optoelectronics, *Adv. Mater.*, 2025, **37**, 2416785.

169 T. Liu, Z. Jia, Y. Song, N. Yu, Q. Lin, C. Li, Y. Jia, H. Chen, S. Wang, Y. Wei, Y. Lin, F. Huang, Z. Tang, Y. Li, L. Meng and H. Huang, Near infrared self-powered organic photodetectors with a record responsivity enabled by low trap density, *Adv. Funct. Mater.*, 2023, **33**, 2301167.

170 Y. Wang, Q. Du, X. Zheng, Y. Zhang, Q. Liu, F. Wang and S. Qin, A polarized near-infrared organic phototransistor based on a narrow-band SnPc single crystal, *J. Mater. Chem. C*, 2024, **12**, 15739–15746.

171 Y. Yao, Y. Chen, H. Wang and P. Samorì, Organic photodetectors based on supramolecular nanostructures, *SmartMat*, 2020, **1**, e1009.

172 T. Cui, N. Luo, Z. Zhang, J. Liu, Y. Sun, D. Liu, Y. Zhang, X. Shao, H. Zhang, L. Jiang and Z. Liu, A fused diketopyrrolopyrrole derivative for single-crystal visible-NIR organic phototransistor, *Small Methods*, 2025, 2402250.

173 Y. Yu, X. Xia, C. Xu, Z. Lv, X. Wang and L. Liao, Customizable organic charge-transfer cocrystals for the dual-mode optoelectronics in the NIR (II) window, *J. Am. Chem. Soc.*, 2024, **146**, 11845–11854.

174 Y. Wang, H. Wu, W. Zhu, X. Zhang, Z. Liu, Y. Wu, C. Feng, Y. Dang, H. Dong, H. Fu and W. Hu, Cocrystal engineering: Toward solution-processed near-infrared 2D organic cocrystals for broadband photodetection, *Angew. Chem., Int. Ed.*, 2021, **60**, 6344–6350.

175 M. Más-Montoya and R. Janssen, The effect of H- and J-aggregation on the photophysical and photovoltaic properties of small thiophene–pyridine–DPP molecules for bulk-heterojunction solar cells, *Adv. Funct. Mater.*, 2017, **27**, 1605779.

176 Y. Liu, Y. Song, Z. Zhu, C. Ji, J. Li, H. Jia, Y. Shi, F. Hu, Z. Zhao, D. Ding, B. Z. Tang and G. Feng, Twisted-planar molecular engineering with sonication-induced j-aggregation to design near-infrared j-aggregates for enhanced phototherapy, *Angew. Chem., Int. Ed.*, 2025, **64**, e202419428.

177 W. Liu, W. Guo, L. Fu, Y. Duan, G. Han, J. Gao, H. Liu, Y. Wang, Z. Ma and Y. Liu, Terminal fluorination modulates crystallinity and aggregation of fully non-fused ring electron acceptors for high-performance and durable near-infrared organic photodetectors, *Angew. Chem., Int. Ed.*, 2025, **64**, e202416751.

178 Z. Lou, J. Tao, B. Wei, X. Jiang, S. Cheng, Z. Wang, C. Qin, R. Liang, H. Guo, L. Zhu, P. Müller-Buschbaum, H. Cheng and X. Xu, Near-infrared organic photodetectors toward skin-integrated photoplethysmography-electrocardiography multimodal sensing system, *Adv. Sci.*, 2023, **10**, 2304174.

179 S. Gao, X. Wang, Y. Zhao, Y. Xu, W. Qiao and Z. Y. Wang, Broadband all-polymer photodetectors with ultrahigh detectivity above 1014 Jones enabled by fine-tuned molecular stacking via facile random terpolymerization, *Chem. Eng. J.*, 2024, **489**, 151377.

180 X. Yu, H. Lin, Z. He, X. Yao, X. Du, Z. Chen, G. Yang, C. Zheng and S. Tao, High-performance near-infrared organic photodetectors enabled by fabricating an interdigital heterojunction, *Adv. Opt. Mater.*, 2024, **12**, 2302170.

181 M. Lim, X. Ma, Y. Kang, M. Jee, S. Lee, S. Jeong, T. Kim, J. Shim, F. Zhang and H. Woo, Symmetric and asymmetric non-fullerene acceptors cooperate synergistically for ternary optoelectronic devices, *Chem. Eng. J.*, 2025, **504**, 158769.

182 S. Park, K. Fukuda, M. Wang, C. Lee, T. Yokota, H. Jin, H. Jinno, H. Kimura, P. Zalar, N. Matsuhisa, S. Umezu, G. Bazan and T. Someya, Ultraflexible near-infrared organic photodetectors for conformal photoplethysmogram sensors, *Adv. Mater.*, 2018, **30**, 1802359.

183 Z. Zhong, K. Li, J. Zhang, L. Ying, R. Xie, G. Yu, F. Huang and Y. Cao, High-performance all-polymer photodetectors via a thick photoactive layer strategy, *ACS Appl. Mater. Interfaces*, 2019, **11**, 14208–14214.

184 W. Köntges, P. Perkhun, J. Kammerer, R. Alkarsifi, U. Würfel, O. Margeat, C. Videlot-Ackermann, J.-J. Simon, R. R. Schröder, J. Ackermann and M. Pfannmöller, Visualizing morphological principles for efficient photocurrent generation in organic non-fullerene acceptor blends, *Energy Environ. Sci.*, 2020, **13**, 1259–1268.

185 S. Bao, H. Yang, H. Fan, J. Zhang, Z. Wei, C. Cui and Y. Li, Volatilizable solid additive-assisted treatment enables organic solar cells with efficiency over 18.8% and fill factor exceeding 80%, *Adv. Mater.*, 2021, **33**, 2105301.

186 H. Tanaka, Y. Abe, Y. Matsuo, J. Kawai, I. Soga, Y. Sato and E. Nakamura, An amorphous mesophase generated by thermal annealing for high-performance organic photovoltaic devices, *Adv. Mater.*, 2012, **24**, 3521–3525.

187 J. Guo, B. Qiu, X. Xia, J. Zhang, S. Qin, X. Li, X. Lu, L. Meng, Z. Zhang and Y. Li, Miscibility regulation and thermal annealing induced hierarchical morphology enables high-efficiency all-small-molecule organic solar cells over 17%, *Adv. Energy Mater.*, 2023, **13**, 2300481.

188 Z. Wang, Z. Peng, Z. Xiao, D. Seyitliyev, K. Gundogdu, L. Ding and H. Ade, Thermodynamic properties and molecular packing explain performance and processing procedures of three D18:NFA organic solar cells, *Adv. Mater.*, 2020, **32**, 2005386.

189 Y. Lau, Z. Lan, L. Cai and F. Zhu, High-performance solution-processed large-area transparent self-powered organic near-infrared photodetectors, *Mater. Today Energy*, 2021, **21**, 100708.

190 J. Ma, J. Wang, J. Hu and Y. Liu, Flexible near-infrared organic photodetectors based on a high work function anode, *J. Mater. Chem. C*, 2024, **12**, 14139–14147.

191 W. Jang, B. Kim, S. Seo, A. Shawky, M. Kim, K. Kim, B. Mikladal, E. Kauppinen, S. Maruyama, I. Jeon and D. Wang, Strong dark current suppression in flexible organic photodetectors by carbon nanotube transparent electrodes, *Nano Today*, 2021, **37**, 101081.

192 J. Xiao, Y. Wang, J. Wu, L. Yuan, H. Tai and Y. Jiang, Suppressing the dark current under forward bias for dual-mode organic photodiodes, *Laser Photonics Rev.*, 2025, **19**, 2400920.

193 T. Kim, J. Lee, M. Jang, G. Lee, E. Shim, S. Oh, M. Saeed, M. Lee, B. Yu, D. Hwang, C. Park, S. Lee, J. Jo and J. Shim, Atto-scale noise near-infrared organic photodetectors enabled by controlling interfacial energetic offset through enhanced anchoring ability, *Adv. Mater.*, 2024, **36**, 2403647.

194 S. Han, H. Lee, W. Choi, D. Lee, S. Kim, Y. Sung, S. Kim and K. Cho, Photomultiplication-type organic photodetectors with fast response enabled by the controlled charge trapping dynamics of quantum dot interlayer, *Adv. Funct. Mater.*, 2021, **31**, 2102087.

195 J. Wang, S. Deng, J. Hu, J. Miao, J. Li, J. Liu and Y. Liu, Alcohol-soluble n-type polythiophenes as cathode interlayer in organic photodetectors for hole blocking, *Adv. Funct. Mater.*, 2024, **34**, 2312502.

196 T. Zhu, Y. Yang, L. Zheng, L. Liu, M. Becker and X. Gong, Solution-processed flexible broadband photodetectors with solution-processed transparent polymeric electrode, *Adv. Funct. Mater.*, 2020, **30**, 1909487.

197 J. Ouyang, Application of intrinsically conducting polymers in flexible electronics, *SmartMat*, 2021, **2**, 263–285.

198 L. Cui, Q. Li, Y. Zhang, J. Zhang, Z. Wang, J. Chen and B. Zheng, Machine learning-assisted high-throughput screening of transparent organic light-emitting diode anode materials, *Chem. Sci.*, 2024, **15**, 19375–19389.

199 Z. Ju, Y. Chen, P. Li, J. Ma, H. Xu, Y. Liu and P. Samorì, Dressing AgNWs with MXenes nanosheets: Transparent printed electrodes combining high-conductivity and tunable work function for high-performance opto-electronics, *Adv. Mater.*, 2024, **36**, 2412512.

200 H. Zhou, T. Li, M. Xie, Y. Zhou, Q. Sun, S.-T. Zhang, Y. Zhang, W. Yang and S. Xue, Improving electron transportation and operational lifetime of full color organic light emitting diodes through a "weak hydrogen bonding cage" structure, *Chem. Sci.*, 2024, **15**, 8106–8111.

201 W. Yang, W. Qiu, E. Georgitzikis, E. Simoen, J. Serron, J. Lee, I. Lieberman, D. Cheyns, P. Malinowski, J. Genoe, H. Chen and P. Heremans, Mitigating dark current for high-performance near-infrared organic photodiodes via charge blocking and defect passivation, *ACS Appl. Mater. Interfaces*, 2021, **13**, 16766–16774.

202 X. Zhou, D. Yang and D. Ma, Extremely low dark current, high responsivity, all-polymer photodetectors with spectral response from 300 nm to 1000 nm, *Adv. Opt. Mater.*, 2015, **3**, 1570–1576.

203 Y. Xia, C. Geng, X. Bi, M. Li, Y. Zhu, Z. Yao, X. Wan, G. Li and Y. Chen, Biomimetic flexible high-sensitivity near-infrared II organic photodetector for photon detection and imaging, *Adv. Opt. Mater.*, 2024, **12**, 2301518.

204 T. Xie, Y. Leng, T. Sun, S. Zhu, H. Cai, P. Han, Y. Zhang, J. Qin, R. Xu, Z. Yi, Y. Zhou and S. Han, Drosophila visual system inspired ambipolar OFET for motion detection, *Adv. Funct. Mater.*, 2025, **35**, 2415457.

205 S. Wang, H. Chen, T. Liu, Y. Wei, G. Yao, Q. Lin, X. Han, C. Zhang and H. Huang, Retina-inspired organic photonic synapses for selective detection of SWIR light, *Angew. Chem., Int. Ed.*, 2023, **62**, e202213733.

206 L. Min, H. Sun, L. Guo, Y. Zhou, M. Wang, F. Cao and L. Li, Pyroelectric-accelerated perovskite photodetector for picosecond light detection and ranging, *Adv. Mater.*, 2024, **36**, 2400279.

207 A. Morteza Najarian, M. Vafaie, A. Johnston, T. Zhu, M. Wei, M. Saidaminov, Y. Hou, S. Hoogland, F. P. García de Arquer and E. Sargent, Sub-millimetre light detection and ranging using perovskites, *Nat. Electron.*, 2022, **5**, 511–518.

208 H. Wang, H. Liu, Q. Zhao, Z. Ni, Y. Zou, J. Yang, L. Wang, Y. Sun, Y. Guo, W. Hu and Y. Liu, A retina-like dual band organic photosensor array for filter-free near-infrared-to-memory operations, *Adv. Mater.*, 2017, **29**, 1701772.

209 Q. Lin, C. Li, H. Xiong, M. Zhang, J. Qiao, J. Wu, L. Yang, S. Wang, H. Chen, Y. Wei, D. Zheng, G. Lu, X. Hao, D. Yu, Y. Cai, A. Facchetti and H. Huang, Event-driven retinomorphic photodiode with bio-plausible temporal dynamics, *Nat. Nanotechnol.*, 2025, **20**, 1213–1220.

210 S. J. Hong, Y. R. Lee, A. Bag, H. S. Kim, T. Q. Trung, M. J. Sultan, D.-B. Moon and N.-E. Lee, Bio-inspired artificial mechanoreceptors with built-in synaptic functions for intelligent tactile skin, *Nat. Mater.*, 2025, **24**, 1100–1108.

211 Y. Zhang, X. Zhu, D. Yu, J. Miao and J. Liu, Stable unencapsulated near-infrared organic photodetectors, *Adv. Opt. Mater.*, 2025, **13**, 2500539.

212 X. Du, J. Han, Z. He, C. Han, X. Wang, J. Wang, Y. Jiang and S. Tao, Efficient organic upconversion devices for low energy consumption and high-quality noninvasive Imaging, *Adv. Mater.*, 2021, **33**, 2102812.

213 S. Dong, J. Li, T. Ma, M. Zhang, L. Zhu, X. Gao, M. Ma, W. Yuan, Z. Wang, F. Liu and X. Jiang, Ternary compensation enables high-sensitive efficient upconversion device for NIR visualization, *Adv. Mater.*, 2025, **37**, 2412678.

214 T. J. Wijaya, S. Xiong, K. Sasaki, Y. Kato, K. Mori, M. Koizumi, S. Lee, M. Kobayashi, Y. Zhou, K. Fukuda, T. Yokota and T. Someya, A highly stable organic–inorganic hybrid electron transport layer for ultraflexible organic photodiodes, *Adv. Mater.*, 2025, **37**, 2501951.

215 J. Zhang, Z. Guo, T. Sun, P. Guo, X. Liu, H. Gao, S. Dai, L. Xiong and J. Huang, Energy-efficient organic photoelectric synaptic transistors with environment-friendly CuInSe2 quantum dots for broadband neuromorphic computing, *SmartMat*, 2024, **5**, e1246.

216 D. Zhu and D. Ji, A stretchable and reconfigurable synaptic transistor, *SmartMat*, 2023, **4**, e1179.

217 Y. Xu, G. Zhang, W. Liu, C. Jin, Y. Nie, J. Sun and J. Yang, Flexible multiterminal photoelectronic neurotransistors based on self-assembled rubber semiconductors for spatiotemporal information processing, *SmartMat*, 2023, **4**, e1162.

218 Y. Ni, L. Yang, J. Feng, J. Liu, L. Sun and W. Xu, Flexible optoelectronic neural transistors with broadband spectrum sensing and instant electrical processing for multimodal neuromorphic computing, *SmartMat*, 2023, **4**, e1154.

219 X. Huang, Y. Liu, G. Liu, K. Liu, X. Wei, M. Zhu, W. Wen, Z. Zhao, Y. Guo and Y. Liu, Short-wave infrared synaptic phototransistor with ambient light adaptability for flexible artificial night visual system, *Adv. Funct. Mater.*, 2023, **33**, 2208836.

220 L. Lv, W. Dang, X. Wu, H. Chen, T. Wang, L. Qin, Z. Wei, K. Zhang, G. Shen and H. Huang, Flexible short-wave infrared image sensors enabled by high-performance polymeric photodetectors, *Macromolecules*, 2020, **53**, 10636–10643.

221 M. Xin, T. Yu, Y. Jiang, R. Tao, J. Li, F. Ran, T. Zhu, J. Huang, J. Zhang, J.-H. Zhang, N. Hu, W. Wang, Q. Zhang, Z. Liu, X. Wang, Y. Shi and L. Pan, Multi-vital on-skin optoelectronic biosensor for assessing regional tissue hemodynamics, *SmartMat*, 2023, **4**, e1157.

222 Y. Wang, T. Zhang, D. Samigullina, L. Winkler, F. Dollinger, J. Kublitski, X. Jia, R. Ji, S. Reineke, D. Spoltore, K. Leo and J. Benduhn, Semitransparent near-infrared organic photodetectors: Flexible, large-area, and physical-vapor-deposited for versatile advanced optical applications, *Adv. Funct. Mater.*, 2024, **34**, 2313689.

223 H. Jiang, Y. Hu, H. Jiang, T. Wei, K. Wang, L. Chen, Q. Zhang and Y. Lei, Unidirectional bias-switchable dual-mode organic photodetectors enables secure communication and gesture simulation, *Adv. Funct. Mater.*, 2025, **35**, 2419686.

224 W. Zeng, Z. Duan, Y. Bu, H. Yu, C. Wang, X. Tang, J. Yang, Z. Yuan, Y. Jiang and H. Tai, A self-powered HgTe quantum dots/PBDB-T:Y6 bipolar broadband photodetector for logic gates, *Mater. Horiz.*, 2025, **12**, 2179–2186.

225 M. Babics, H. Bristow, W. Zhang, A. Wadsworth, M. Neophytou, N. Gasparini and I. McCulloch, Non-fullerene-based organic photodetectors for infrared communication, *J. Mater. Chem. C*, 2021, **9**, 2375–2380.

226 E. Hong, Z. Li, X. Zhang, X. Fan and X. Fang, Deterministic fabrication and quantum-well modulation of phase-pure 2D perovskite heterostructures for encrypted light communication, *Adv. Mater.*, 2024, **36**, 2400365.

227 F. Cao, J. Chen, D. Yu, S. Wang, X. Xu, J. Liu, Z. Han, B. Huang, Y. Gu, K. L. Choy and H. Zeng, Bionic detectors based on low-bandgap inorganic perovskite for selective NIR-I photon detection and imaging, *Adv. Mater.*, 2020, **32**, 1905362.

228 S. Tian, B. Li, Y. Dai and Z. L. Wang, Piezo-phototronic and pyro-phototronic effects enhanced broadband photosensing, *Mater. Today*, 2023, **68**, 254–274.

229 R. Xing, X. Zhang, X. Fan, R. Xie, L. Wu and X. Fang, Coupling strategies of multi-physical fields in 2D materials-based photodetectors, *Adv. Mater.*, 2025, **37**, 2501833.

230 J. Liu, K. Yi, Z. Wang, Z. Zhang, Y. Qi, P. Chen, Q. Shen and B. Chu, All-organic composites with strong photoelectric response over a wide spectral range, *Sci. China Mater.*, 2021, **64**, 1197–1205.

231 X. Wang, P. Wang, J. Wang, W. Hu, X. Zhou, N. Guo, H. Huang, S. Sun, H. Shen, T. Lin, M. Tang, L. Liao, A. Jiang, J. Sun, X. Meng, X. Chen, W. Lu and J. Chu, Ultrasensitive and broadband MoS2 photodetector driven by ferroelectrics, *Adv. Mater.*, 2015, **27**, 6575–6581.

232 X. Lu, L. Sun, P. Jiang and X. Bao, Progress of photodetectors based on the photothermoelectric effect, *Adv. Mater.*, 2019, **31**, 1902044.

233 K. Tielrooij, N. Hesp, A. Principi, M. Lundeberg, E. Pogna, L. Banszerus, Z. Mics, M. Massicotte, P. Schmidt, D. Davydovskaya, D. Purdie, I. Goykhman, G. Soavi, A. Lombardo, K. Watanabe, T. Taniguchi, M. Bonn, D. Turchinovich, C. Stampfer, A. Ferrari, G. Cerullo, M. Polini and F. Koppens, Out-of-plane heat transfer in van der Waals stacks through electron–hyperbolic phonon coupling, *Nat. Nanotechnol.*, 2018, **13**, 41–46.

234 D. Sun, G. Aivazian, A. Jones, J. Ross, W. Yao, D. Cobden and X. Xu, Ultrafast hot-carrier-dominated photocurrent in graphene, *Nat. Nanotechnol.*, 2012, **7**, 114–118.

235 J. Kublitski, A. Hofacker, B. Boroujeni, J. Benduhn, V. Nikolis, C. Kaiser, D. Spoltore, H. Kleemann, A. Fischer, F. Ellinger, K. Vandewal and K. Leo, Reverse dark current in organic photodetectors and the major role of traps as source of noise, *Nat. Commun.*, 2021, **12**, 551.

236 D. Lv, X. Liu, J. Li, S. Hou, Y. Li, Z. Wang, Q. Zhang, S. Wang, X. Yu and Y. Han, Improving the uniformity and stretchability of inkjet-printed films by adding the surfactant Triton X, *ACS Appl. Mater. Interfaces*, 2024, **16**, 66301–66315.

237 H. Mao, J. Zhang, L. Wen, L. Tan, Y. Liu, J. Yang, Z. Qin, L. Zhang, Y. Zhai and Y. Chen, Controlled solution flow via patterned meniscus assist for elongated exciton diffusion length to approaching 20% efficiency in pseudo-planar heterojunction organic solar cells, *Adv. Mater.*, 2025, **37**, 2505266.

238 D. Wu, C. Guo, L. Zeng, X. Ren, Z. Shi, L. Wen, Q. Chen, M. Zhang, X. J. Li, C.-X. Shan and J. Jie, Phase-controlled van der Waals growth of wafer-scale 2D MoTe2 layers for integrated high-sensitivity broadband infrared photodetection, *Light: Sci. Appl.*, 2023, **12**, 5.

239 S. Hinds, L. Levina, E. J. D. Klem, G. Konstantatos, V. Sukhovatkin and E. H. Sargent, Smooth-morphology ultrasensitive solution-processed photodetectors, *Adv. Mater.*, 2008, **20**, 4398–4402.

240 Z. Chen, S. Duan, X. Zhang, B. Geng, Y. Xiao, J. Jie, H. Dong, L. Li and W. Hu, Organic semiconductor crystal engineering for high-resolution layer-controlled 2D crystal arrays, *Adv. Mater.*, 2022, **34**, 2104166.

241 S. Duan, T. Wang, B. Geng, X. Gao, C. Li, J. Zhang, Y. Xi, X. Zhang, X. Ren and W. Hu, Solution-processed centimeter-scale highly aligned organic crystalline arrays for high-performance organic field-effect transistors, *Adv. Mater.*, 2020, **32**, 1908388.

242 K. Ba and J. Wang, Advances in solution-processed quantum dots based hybrid structures for infrared photodetector, *Mater. Today*, 2022, **58**, 119–134.

243 Y. Zhang, Y. Wang, C. Gao, Z. Ni, X. Zhang, W. Hu and H. Dong, Recent advances in n-type and ambipolar organic semiconductors and their multi-functional applications, *Chem. Soc. Rev.*, 2023, **52**, 1331–1381.

244 L. Han, S. Ogier, J. Li, D. Sharkey, X. Yin, A. Baker, A. Carreras, F. Chang, K. Cheng and X. Guo, Wafer-scale organic-on-III-V monolithic heterogeneous integration for active-matrix micro-LED displays, *Nat. Commun.*, 2023, **14**, 6985.

245 X. Zhao, H. Zhang, J. Zhang, J. Liu, M. Lei and L. Jiang, Organic semiconductor single crystal arrays: Preparation and applications, *Adv. Sci.*, 2023, **10**, 2300483.

246 H. Kweon, S. Kim, B. Ha, S. Lee, S. Lee, S. Roh, H. Oh, J. Ha, M. Kang, M. S. Kang, J. H. Cho and D. H. Kim, Microlithography of hole transport layers for high-resolution organic light-emitting diodes with reduced electrical crosstalk, *Nat. Electron.*, 2025, **8**, 66–74.

247 X. Wu, X. Zhu, L. Sun, S. Zhang, Y. Ren, Z. Wang, X. Zhang, F. Yang, H.-L. Zhang and W. Hu, Navigating the transitional window for organic semiconductor single crystals towards practical integration: from materials, crystallization, and technologies to real-world applications, *Chem. Soc. Rev.*, 2025, **54**, 1699–1732.